博士論文

Development of Multi-Filter Soft X-ray Imaging Diagnostic for High-Energy Electron Study of Magnetic Reconnection
(磁気リコネクションの高エネルギー電子の検証のためのマルチフィルターの軟X線イメージング計測の開発**)**

Student ID: 37-187185

Author: Junguang Xiang
向 俊光

Supervisor: Prof. Yasushi Ono
小野 靖 教授

Department of Electrical Engineering and Information Systems
Graduate School of Engineering
The University of Tokyo

Submitted in partial fulfillment of the requirements for the degree of
Doctor of Philosophy

December 2021

Acknowledgements

It is my great honor to be a member in the Ono laboratory, where I have opportunity to carry out my research on magnetic reconnection with advanced facilities and intelligent researchers.

First of all, I would like to sincerely thank my supervisor, Professor Yasushi Ono, a very knowledgeable and rigorous scientist with rich experience in the field of magnetic reconnection and high-temperature plasma. Prof. Ono is approachable and always patiently teaches me a lot about magnetic reconnection and plasma diagnostic techniques. His careful guidance and valuable suggestions give me great help and inspiration to finish the experiments and this thesis. Prof. Ono's integrity, enthusiasm for research and rigor for experiments have influenced my studies and life over the years. Here, I would like to express my sincere gratitude to Prof. Ono again.

I am sincerely grateful to professor Inomoto for his kind advice about soft X-ray measurement, especially about the high-voltage circuit which is used to control the MCPs. I also learned a lot from Prof. Inomoto's research in the UTST merging experiments.

I am sincerely grateful to associate professor Tanabe for giving me important and valuable advice and suggestions on my experiments and also for helping me to solve many problems encountered in my research. Prof. Tanabe shared his experience with me and taught me a lot of knowledge about optical systems including lenses and cameras.

It is my great pleasure to work with Mr. Takeda and Mr. Okunishi for the soft X-ray measurement. Thank you very much. You are talented and industrious. There is no doubt that the soft X-ray diagnostic would be much better developed by you in the future.

Many thanks to Dr. Tanaka, Dr. Cao, Dr. Cai, Dr. Tara, and Dr. Akimitsu. As my tutor, Dr. Tanaka picked up me from the Ueno station when I arrived in Tokyo for the first time and gave me a lot of help in school life and research. Dr. Cao taught me the start-up of experiments when I knew little about the experimental facilities. Valuable communications with Dr. Cai had expanded my horizon about research of magnetic reconnection all over the world. Dr. Cai also shared his knowledge and experience with me, including the school life as an international student. Dr. Tara is in the same grade with me, so we always meet the same problem and help each other. Dr. Akimitsu makes great efforts for the operation of TS-6 device. Thank you all very much.

I would like to thank all the members of the Ono laboratory. We work together, share the pleasure of research and deal with unpredictable trouble of experiments. Besides the research, I also learned a lot of knowledge about Japanese culture and customs from you all. I will never forget the time we spend together.

I sincerely wish you all the best in your research and life.

Abstract

Magnetic reconnection is an important and basic physical process, which has been widely found both in space plasma, such as solar flares, coronal mass ejection and interaction of solar wind with Earth's magnetosphere, and in laboratory plasmas[1]. During the evolution of the magnetic reconnection, the magnetic topology is rearranged, resulting in breaking and reconnecting magnetic field lines. There are several approaches to study the magnetic reconnection, such as observing space plasma, simulation, and laboratory plasma. Compared with space plasma observation, laboratory plasmas can be actively controlled and diagnostic systems are relatively easier to develop. Merging two torus plasmas together is an effective method for investigating magnetic reconnection, which is carried out since 1980s on TS-3[2, 3] (Tokyo University Spherical Torus Device No. 3). On the other hand, it is also a potential technique for fusion plasma heating. As a major upgrade of TS-3, TS-6/TS-3U device was successfully assembled, and the first plasma was produced in 2018 spring[4, 5].

Magnetic energy would be converted into thermal or kinetic energy by heating or accelerating charged particles, when the magnetic reconnection happens. It indicates that charged particle (electron and ion) heating and acceleration are key physical processes to study energy conversion mechanism. The ion heating characteristic during magnetic reconnection has been sufficiently investigated on TS-4[3], MAST[6], and TS-6[7], while electron heating and acceleration mechanism is still not well understood. UTST has found that electron acceleration could be measured not only around the X-point but also in the downstream region during the magnetic reconnection by soft X-ray (SXR) diagnostic[8, 9].

We developed a multi-filter high-resolution tangential-view SXR tomographic imaging measurement on TS-6 spherical tokamak (ST) merging device, as a key diagnostic for investigating high-energy electron characteristics[10]. Multiple micro-channel plates (MCPs) are respectively installed in individual vacuum chambers. In the front of each chamber, there is a pinhole covered by a special filter, which constitutes a pinhole camera system. By installing different filters, we can measure SXR with different energy ranges. Especially designed lenses and fiber bundles serve as optical system to transfer images from phosphor plates of MCPs to a high speed imaging system. This design also enables us to simultaneously measure two images appearing on phosphor plates of MCPs by just one high speed imaging system. We had prepared more fiber bundles in advance for upgrades, and up to 16 images can be measured synchronously in the future. On the other hand, it also makes it possible to install the camera system far from the TS-6 in order to protect the camera system. As the measured images by camera system are line-integrated, we developed tomographic method based on the Phillips-Tikhonov regularization[11, 12] to reconstruct the local emissivity of SXR, which reflects the spatial distribution of high-energy electrons.

Relying on this diagnostic, we successfully measured SXR emitted from the TS-6 plasma merging experiments for the first time in 2021 spring. The energy range of SXR was distinguished to be higher than 100 eV but lower than 400 eV by the multi-filter arrangement of this SXR diagnostic. According to the reconstructed results of local SXR emissivity, which reflects the spatial distribution of high-energy electrons, electron acceleration in the X-point and downstream region was successfully measured.

In the downstream regions, the majority of energetic electrons are found distributing in the direction perpendicular to the magnetic field. With the evolution of magnetic reconnection, electrons with higher energy are measured in further part of downstream region. During the magnetic reconnection, electrons leave from X-point region along with the outflow and most of them would be trapped by the electric potential. These electrons can be accelerated by the induced electric field in the magnetic pileup areas, and obtain much more energy along with the movement to further parts of the downstream region. On the other hand, downstream acceleration can be enhanced with the increase of poloidal magnetic field (PF)/B_t.

It means that betatron acceleration plays an important role for the electron acceleration in the downstream region.

We also found that X-point acceleration can be enhanced with the increase of toroidal magnetic field (TF)/guide field. On the other hand, the increasing of guide field can also make the X-ray burst occur earlier. When the electrons enter into the area near the X-point, they would rotate around the guide field. The guide field confines electrons in the vicinity of X-point and further accelerate them. With a higher guide field, electrons would be accelerated and obtain higher kinetic energy, leading to the higher local emissivity of SXR. On the other hand, the kinetic energy of electrons would reach the peak value earlier and then fall.

Table of contents

Chapter 1

Introduction

The magnetic reconnection, as a basic physical process[13], has been widely observed both in space and laboratory plasmas[1, 14]. When the magnetic reconnection happens, the topology of magnetic field would be changed due to the breaking and reconnection of the magnetic field lines. On the other hand, the stored energy in the magnetic field would be converted into thermal and kinetic energy of charged particles. Therefore, the electrons and ions are to be heated or accelerated, and these physical phenomenons have been reported by astronomical observations[15, 16], simulations[17, 18] and laboratory plasmas[8, 6, 19–21].

Laboratory plasmas can provide a relatively more active and comprehensive method to study the magnetic reconnection. With the development of plasma diagnostics, more plasma parameters can be measured. Since 1980s, merging of two torus plasmas has been developed as an effective experimental method to investigate the magnetic reconnection in the TS-3 device[2]. As the huge burst of thermal and kinetic energy of particles happens, this merging start-up has become a potential heating method for high-temperature plasma devices, especially for spherical tokamak[6, 4]. On the other hand, there are also phenomenons related to magnetic reconnection which have been observed in fusion plasmas[22, 23]. Therefore, research about magnetic reconnection is also necessary for nuclear fusion.

In this chapter, some concepts about nuclear fusion, spherical tokamak and plasma diagnostics are introduced, which would be used for following chapters.

1.1 Nuclear Fusion

Energy, which is closely related to various aspects of human life, is the basis for maintenance and development of human civilization. With the rapid development of science and technology, the demand for energy in modern society is also increasing rapidly. One important and urgent issue, how to meet the increasing demand for energy while the available amount of fossil fuels such as petroleum, coal, and natural gas is exhaustible, gradually arises to be focused by the whole society. On the other hand, the accumulating use of fossil fuels has bringing about environment pollution, due to exhaust of CO_2 and other harmful gases. Thus, clean energy sources are necessary for the sustainable existence and development of human beings. Wind-power, hydro-power, solar-power, geothermal-power and bio-energy, as mainstream technologies of renewable energy, have been developed and become important energy sources for human society. However, limited by the low capacity factors, renewable energy is not able to become main energy sources at present.

In addition to fossil fuels and renewable energy, nuclear power, which can be obtained from fission, decay and fusion, is another important source of energy, which has already become the second-largest low-carbon energy source after hydro-power and equivalently supplied about 10% of global electricity generation in 2019[24]. Without the commercialization of nuclear fission since the 1970s, there would be about more 1.84 million deaths related to air pollution and the emission of about 64 billion tonnes of carbon dioxide if this part of energy was obtained from fossil fuels. In contrast to the common perception, nuclear power releases less radiation into the environment than any other major energy source. On the other hand, nuclear power has much higher capacity factors than normal fossil fuels and various renewable energy sources. Nuclear power has become an indispensable part of the energy solution. Even though the nuclear power obtained from fission is a safe, clean and sustainable energy source, it also caused some threats to human beings and the environment, such as Chernobyl accident in 1986.

So, how to solve the energy crisis? Is there one kind of energy source that is safe, clean, abundant, and environment-friendly? Owing to the less radioactive emission and higher

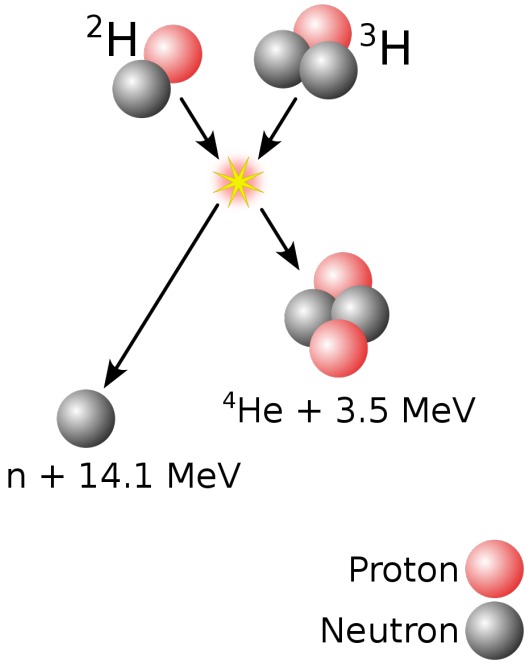

Fig. 1.1 Schematic diagram of D-T fusion reaction.[25]

effectiveness than fission, controlled nuclear fusion has been regarded as a potential candidate to solve the problems mentioned above. Deuterium-Tritium (D-T) nuclear fusion[25], as shown in the Fig. 1.1, is regarded as the most possible reaction type to realize the controlled fusion energy, owing to relatively small Coulomb repulsion and large reaction cross-section.

In a high-temperature plasma, particles have high kinetic energy which results to severe inflation of the plasma. In order to maintain required particle density for nuclear fusion reaction, the particles have to be confined. Investigation about controlled nuclear fusion has been theoretically and experimentally carried out since the 1950s, even though there are still many non-negligible difficulties at present. There are two main technical routes to realize the controlled utilization of nuclear fusion power, magnetic confinement fusion and inertial confinement fusion. Compared to inertial confinement fusion, magnetic confinement fusion is regarded as a more promising technical strategy to reach the commercialization of fusion power, as it is able to operate under much more easily achievable conditions and in steady state for a much longer time.

1.2 Magnetic Confinement Fusion

Magnetic confinement fusion (MCF), just as its name implies, is to employ magnetic field to confine the high-temperature plasma and maintain the nuclear fusion reaction. Based on the topology of magnetic filed configuration, MCF can be classified to be open type or closed type. Magnetic mirror is a typical example of open-type MCF devices, with magnetic field lines open in both sides, as shown in the Fig. 1.2. As part of particles would escape from this kind of confinement device along the magnetic field line, there is significant loss. The closed type MCF devices were proposed to reduce the above disadvantages. Even so, not all charged particles move along the magnetic field lines, and particle loss would still happen due to drift movement. Tokamak and stellarator have become two most promising kinds of MCF devices to solve the drift losses after several decades' development.

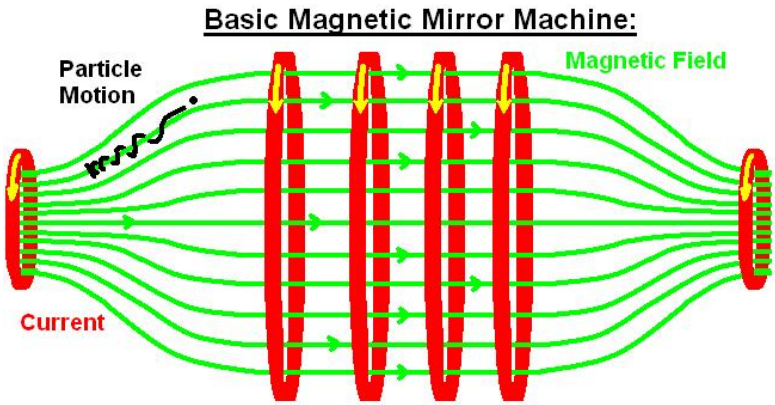

Fig. 1.2 Schematic diagram of a magnetic mirror device[26].

Toroidal field coil is one of the main components of tokamak devices, as shown in the Fig. 1.3[27], which can generate high magnetic field in the toroidal direction to confine and stabilize the plasma. Plasma current could be induced in a tokamak plasma and the current is able to not only further heat the plasma (Ohm heating) but also generate poloidal magnetic field, which would form the helical field together with the toroidal field. The helical field, like a net, is able to reduce the losses of particles due to charge separation. Even though tokamak devices have some certain advantages due to symmetric structure in the toroidal

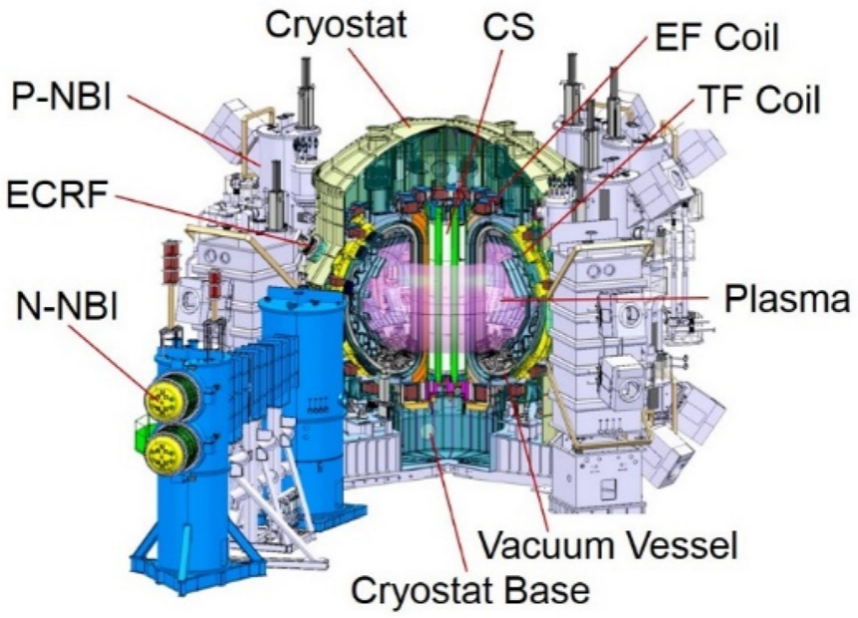

Fig. 1.3 Schematic diagram of the JT-60SA tokamak device[27].

direction, there are still some disadvantages. Due to the existence of plasma current in a tokamak plasma, plasma disruption caused by macro MHD instability could happen, which would destroy the confinement, end the discharge of plasma and even damage the device.

On the macro level, the research related to tokamak plasmas focuses on various MHD instabilities, which would determine the operation limitation of a device. The research purpose is to better control plasmas and break through the operation limitation, in order to improve the plasma parameter and avoid huge disruption of plasma. Deep understanding of macroscopic plasma physics is necessary for the research mentioned above, which relies on the improvement of plasma diagnostics and simulation. Macro instability problems are relatively easier to be observed, and some successful progress has been achieved. With the improvement of plasma parameters and proposal of new operation models, there are more challenges.

Micro instabilities are mainly related to plasma transport. Experimental results reveal that the plasma transport is much higher than the theoretical value calculated by classical transportation model and neoclassical transport model, which has considered the dynamic of particles in cylindrical devices. Therefor, it is called anomalous transport. Recent

experiments and simulations have confirmed that the anomalous transport could be caused by micro instabilities, such as drift wave. Research related to the above mentioned problems, such as neoclassical magnetic island, zonal flow, and non-local effect, has widely drawn attention. Benefiting from this, new physical images have been proposed, and problems about plasma turbulence and relationship between macro and micro processes have been better understood.

Edge plasma is also non-negligible for plasma confinement. The interaction between edge plasma and wall of the device can cause some negative influence on tokamak operation.

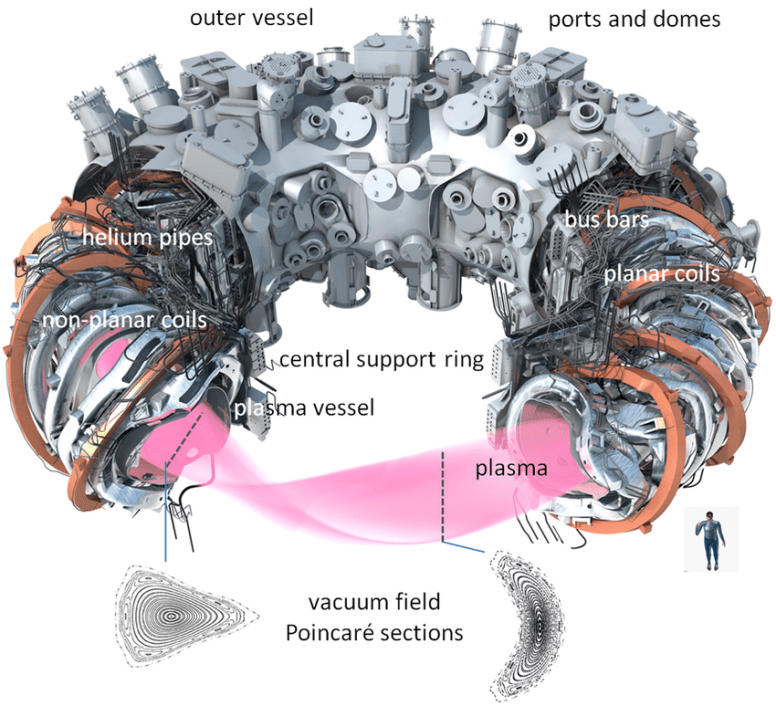

Fig. 1.4 Schematic diagram of the Wendelstein 7-X stellarator device[28].

Different from tokamak devices whose poloidal magnetic fields are generated by plasma current, some certain external coils in a stellarator device can induce magnetic fields in the poloidal direction, as shown in the Fig. 1.4[28]. Stellarator devices do not rely on plasma current to generate poloidal fields, and there is no pure toroidal current in a stellarator plasma. Thus, a lot of MHD instabilities related to plasma current in tokamak devices would not happen in stellarator devices, which means that it could be easier to achieve higher plasma

density and β in a stellarator. For stellarator devices, the precision of manufacture and installation is highly required due to complicated structure of magnet.

The Fig. 1.5 shows the sketch of tokamak geometry. The magnetic flux surface that intersects with the X-point is called the separatrix. As all flux surfaces external to this surface are unconfined, the separatrix defines the last closed flux surface (LCFS).

There are some items listed as follows: R_{max} and R_{min} are respectively the maximum and minimum value of R along the LCFS or separatrix; Z_{max} and Z_{min} are respectively the maximum and minimum value of Z along the LCFS or separatrix; R_{upper} and R_{lower} are respectively the major radius of the highest and lowest vertical point of the LCFS or separatrix.

Then, some parameters can be derived from the above items, as shown in the Table. 1.1. The triangularity and ellipticity (also referred to as elongation) refer to the shape of the poloidal cross-section of the LCFS or separatrix of a tokamak device.

Table 1.1 Some parameters of tokamak geometry

Parameter	Expression
Geometric Major Radius R_{geo}	$(R_{max}+R_{min})/2$
Minor Radius a	$(R_{max}-R_{min})/2$
Upper Triangularity δ_{upper}	$(R_{geo}-R_{upper})/a$
Lower Triangularity δ_{lower}	$(R_{geo}-R_{lower})/a$
Ellipticity κ	$(Z_{max}-Z_{min})/2a$

The field line pitch or rotational transform is defined as the number of poloidal transits per single toroidal transit of a field line on a toroidal flux surface, expressed as $\iota/2\pi$. For a toroidally helical magnetic flux surfaces, the field line pitch on such a surface can be defined as:

$$\frac{\iota}{2\pi} = \frac{\mathrm{d}\psi}{\mathrm{d}\Phi}, \tag{1.1}$$

where ψ is the poloidal magnetic flux, and Φ is the toroidal magnetic flux.

The safety factor can be defined as $q = 2\pi/\iota$. Assuming that ϕ, θ, and B_θ represent the toroidal angle, poloidal angle, and poloidal magnetic field respectively. In a tokamak, there

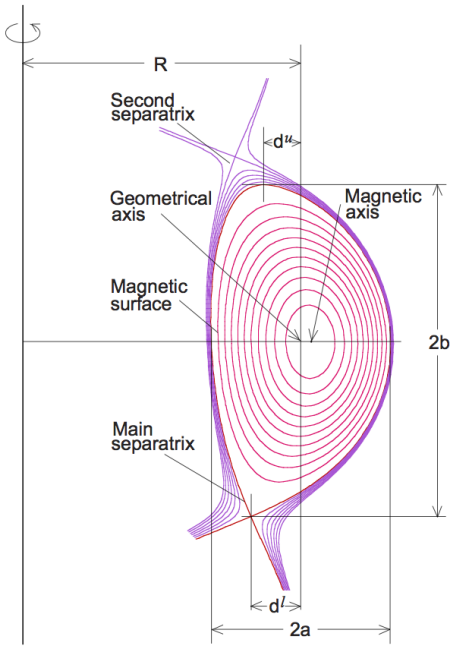

Fig. 1.5 Sketch of tokamak geometry, including separatrix[29].

is an approximation for a field line on the flux surface, expressed as follows:

$$\frac{r\mathrm{d}\theta}{B_\theta} = \frac{R\mathrm{d}\phi}{B_\phi}. \tag{1.2}$$

Thus, the safety factor can be expressed as:

$$q = \frac{m}{n} = \left\langle \frac{\mathrm{d}\phi}{\mathrm{d}\theta} \right\rangle \simeq \frac{rB_\phi}{RB_\theta}. \tag{1.3}$$

As mentioned above, the poloidal magnetic field is mostly produced by the toroidal plasma current in a tokamak device. If the safety factor $q \leq 2$ at the LCFS, the plasma is magnetohydrodynamically unstable.

1.3 Spherical Tokamak

Spherical tokamak is a new type of tokamak with low aspect ratio, which develops from 1980s. The aspect ratio A is defined as the ratio of major radius R and minor radius a, expressed as $A = R/a$. For normal tokamak devices, the aspect ratio is larger than 3. If the aspect ratio is smaller than 1.5, then this device can be called as spherical tokamak. The Fig. 1.6 shows the comparison of conventional tokamak and spherical one. With the decrease of aspect ratio, the shape of plasma tends to be spherical, and the cross-section of plasma is elongated in the vertical direction. In a spherical tokamak device, magnetic field lines much more concentrate on the inner side of the torus where the magnetic field is much higher, which is beneficial for MHD stability. Even though the spherical tokamak have the same topology to conventional tokamak, it is able to generate higher plasma current by using lower magnetic field due to much better utilization of magnetic field, which would reduce the cost of magnets. Furthermore, because of the great utilization of magnetic field, superconducting magnets may not be required, which would reduce the engineering difficulty.

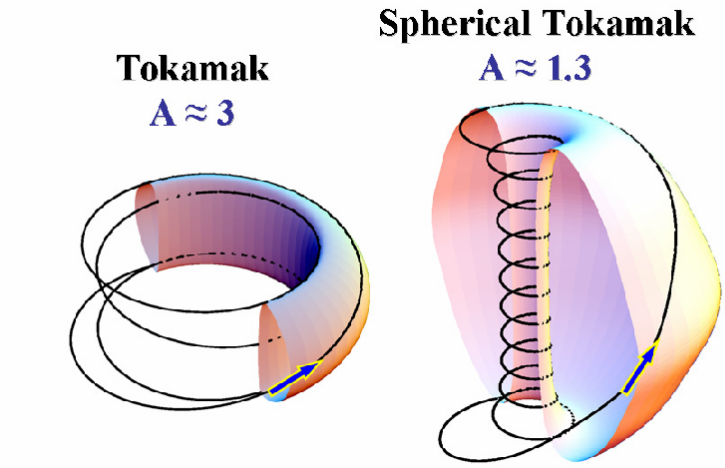

Fig. 1.6 Schematic diagram of a spherical tokamak and a conventional tokamak[30].

Beta β, the ratio of plasma pressure to magnetic pressure, is an important plasma parameter for MCF devices, which can be expressed as[31]:

$$\beta = \frac{p}{B^2/2\mu_0}. \tag{1.4}$$

The ratio β is able to show the confinement performance of MCF devices, and also plays a decisive role on determining macro balance and magneto-hydrodynamics (MHD) instability of plasma.With higher β , relatively less energy would be used to generate the magnetic fields for given plasma pressure or density. In practice, most tokamaks operate at β of order 0.01, while spherical tokamaks typically operate at β values an order of magnitude higher. Even though, it is possible to build a conventional tokamak that operates at higher β by use of more powerful magnets, such as superconducting ones, the current in the plasma must be increased in order to generate the toroidal magnetic field of the suitable magnitude, which would cause much more instability for the plasma. Due to special characteristic in design of spherical tokamak, much better safety factor q can be achieved, and thus it allows for much more magnetic power before the instabilities appear.

1.4 Plasma Diagnostics

High temperature plasmas are complex systems, which can not be simply described by some physical parameters, and the measurement for these parameters is also complicate. There are many kinds of physical processes, which can occur in a high temperature plasma, including elastic collisions between charged particles (Coulomb collisions), elastic collisions of electrons or ions with neutral particles, charge exchange between an ion and a neutral particle, inelastic collisions between electrons and neutral particles or ions, and interaction of photons and charged particles. The energy magnitude of particles during the physical processes mentioned above ranges from eV to 10 KeV, and the density magnitude ranges from 10^{17} m^{-3} to 10^{21} m^{-3}. In order to understand such plasmas, which sometimes can not be measured directly, plasma diagnostics has been developed to quantitatively reveal detailed characteristics. On the other hand, plasma diagnostics can also provide necessary data to ensure the normal operation of plasma devices.

Passively measuring various electromagnetic fields (including frequency regions range from microwaves to X-rays) emitted from plasmas, as well as magnetic fields generated by plasmas. The main passive diagnostic methods and their measured parameters are shown in the Tab. 1.2, including Includes: Mirnov, pickup coils for measuring magnetic fields, flux loops, electron cyclotron diagnostics for measuring electron temperature and its fluctuation, soft X-ray diagnostics for measuring electron temperature, density and effective charge number Z_{eff}, H_α/D_α diagnostics, spectral diagnostics for measuring various impurity radiations.

Active probes are inserted into the plasma, including: physical probes such as electrostatic and magnetic probes, microwave probes, laser probes, particle probes. These probes enter the plasma and interact with the plasma and diagnose the plasma based on the properties of the interaction. The main active diagnostic methods and the parameters they measure are shown in Tab. 1.3, including: Thomson laser scattering diagnostics for measuring electron temperature and density, charge exchange compound spectroscopy diagnostics for measuring ion temperature, plasma rotation velocity and impurity density, kinematic Stark effect for

Table 1.2 Passive plasma diagnostics and its measured parameters.

Name	Measurement Parameters
Mirnov Coils, Pickup Coils	Magnetic field components and fluctuations (outside plasma)
Flux Loops	Magnetic field (outside plasma)
Electron Cyclotron Emission	Electron temperature T_e, electron temperature fluctuations (turbulence) $\widehat{T_e}$ (local)
Soft X-Ray Emission	A combination of electron temperature T_e, electron density n_e, and effective charge Z_{eff} (line integral)
Bolometry	Broad spectrum emission (line integral)
H_α Monitors	Emission of specific H_α radiation
Spectroscopy	Monitoring of impurities, etc. (line integral)

measuring magnetic pitch angle, heavy ion beam probes for measuring electron density and plasma potential, electron density interferometry, polarimetry for measuring magnetic pitch, reflectometry for measuring electron density, Langmuir probes for measuring ion saturation current, plasma potential and Mach number, beam emission spectroscopy diagnostics.

Table 1.3 Active plasma diagnostics and its measured parameters.

Name	Measurement Parameters
Thomson Scattering	Electron temperature T_e, electron density n_e (local)
Charge Exchange Recombination Spectroscopy	Ion temperature T_i, toroidal and poloidal plasma rotation velocity v_ϕ, v_θ, impurity density n_Z
Motional Stark Effect	Magnetic pitch angle $tan(\gamma) = B_\theta / B_\phi$
Heavy Ion Beam Probe	Electron density n_e, plasma potential ϕ (local)
Interferometry	Electron density n_e (line integral)
Polarimetry	Magnetic field pitch (line integral)
Reflectometry	Electron density n_e (local, fluctuations)
Langmuir probes	Ion saturation current, plasma potential, Mach number, etc. (local, fluctuations)
Diagnostic beams	Injection of Helium, Lithium, etc., and observation of emitted radiation (local, fluctuations)

At the same time, the high temperature environment also limits the design of diagnostic system. For example, diagnostic systems which would contact the plasma directly are

generally limited to boundary probes. On the other hand, diagnostic systems should avoid interfering the plasma as much as possible during the measurement of plasma parameters. The following factors should be considered for the choice and design of plasma diagnostic system.

Temporal and spacial resolution

High temporal resolution is necessary for micro problems and some rapid macro problems such as plasma disruption and magnetic reconnection. High spacial resolution is usually required for measuring some fine structure such as electron temperature gradient (ETG) mode. Besides, for some diagnostics whose measured results are line-integrated, tomographic reconstruction is necessary. The active spectroscopy diagnostic can usually achieve high spacial resolution.

Signal-to-noise ratio (SNR)

Shielding, isolation and filtering are the most commonly used methods for reducing the noise and improving the reliability of plasma diagnostic system.

Measurement precision

In general, the precision of plasma diagnostic system is not so high. It is necessary to improve the precision as much as possible.

Objective energy range and spacial coverage

The energy magnitude of particles is wide. Due to the limitation of plasma device and other systems, the position, observing direction, and spacial coverage should also be considered.

1.5 Outline

The multi-filter high-resolution soft X-ray imaging diagnostic developed on TS-6 plasma merging experiments in order to investigate the high-energy electrons accelerated during the evolution of magnetic reconnection is in detailed introduced in this thesis, as well as the tomographic method. The experimental results measured by this diagnostic are also discussed.

The structure of this thesis is as follows:

Chapter 1 introduces some basic concept about nuclear fusion, spherical tokamak which the TS-6 device belongs to, and plasma diagnostic.

Chapter 2 explains the principle and models of magnetic reconnection, which helps to understand its physical image.

Chapter 3 introduces the plasma merging experiment method, the arrangement of TS-6, and main diagnostics, which can provide well understanding of experimental facilities in this thesis.

Chapter 4 in detail shows the design and arrangement of soft X-ray diagnostic on TS-6 merging device. The principle and algorithm of tomographic method are also introduced.

Chapter 5 presents the experiment results obtained by this soft X-ray diagnostic. These experimental results are compared with some simulations which have already been reported.

Chapter 6 summarizes this thesis, and gives some discussions.

Chapter 2

Magnetic Reconnection

There are many burst phenomena, which can be observed in space and laboratory plasmas, such as solar flares and magnetosphere sub-storms, as well as saw-tooth crash[22] and rupture instabilities in tokamak devices, resulting in release of huge energy in short time and rapid change of plasma state[16, 1]. The source of energy leading to such phenomena comes from the magnetic field. Magnetic energy can be effectively and rapidly transformed to thermal and kinetic energy of particles during the magnetic reconnection in the plasma. At the same time, the topology of magnetic field is also changed.

The concept of magnetic reconnection was first introduced by Ronald Gordon Giovanelli[32], who suggested that discharges occur near the neutral point or neutral line where the magnetic field strength is zero, and may play an important role in the occurrence of solar flares. The term reconnection was first introduced by James Dungey in 1958[33] and was then applied to the Earth's magnetosphere, creating the first open magnetosphere model. The first magnetic reconnection model was proposed by Sweet and Parker[34, 13], in which the plasma carries the magnetic field from both sides to the centre of the current sheet, where the magnetic lines of force are cut and reconnected, and the magnetic field energy is converted into kinetic and thermal energy of the plasma before flowing out at both ends of the current sheet. However, the magnetic reconnection rate predicted by the Sweet-Parker model is too slow to explain the outbursts that occur in real space plasmas. Petschek improved on the Sweet-Parker model

by suggesting that magnetic reconnection occurs in a system consisting of two pairs of slow excitation and an X-shaped diffusion zone[35]. Although the speed of reconnection in the Petschek model is much improved over that of the Sweet-Parker model, it is still too slow to explain the observed outbursts in space plasmas. It is important to note that these early magneto-reconnection models were based on the magneto-hydrodynamic equations, where energy dissipation was achieved through electrical resistance.

2.1 Basic Process

The Fig. 2.1 schematically shows the magnetic reconnection process[36]. The shaded blue box in the Fig. 2.1 denotes the boundary layer between two magnetically disconnected regions. Above and below the box, called the diffusion region, the ambient plasma (sketched as blue circles) is threaded by a magnetic field (thin blue curves). The key aspect of magnetic reconnection is that the magnetic fields above and below have a component that reverses at the boundary layer. This implies there is an out-of plane current through the diffusion region, given as the background image in the Fig. 2.1. When magnetic reconnection occurs, the topology of the magnetic field changes. This process can be regarded as a magnetic field line from above converting into the diffusion region and effectively breaking and reconnecting with a similar magnetic field line converting up from below.

The diffusion region is where charged particles become decoupled from the magnetic field, either through complex orbits in geometries with steep spatial gradients, or through interactions with the electromagnetic fields in turbulent waves. Intense energy conversion from the magnetic energy occurs in the diffusion region, and the charged particles there would be heated or accelerated. Therefore, the plasma to the left and right is hotter than the ambient plasma. The boundary layer to the left and right of the diffusion region bifurcates into two layers bounding the magnetic field lines that have already undergone magnetic reconnection. This boundary layer is also a location of heating and acceleration of the ambient plasma. This whole set of physical phenomena are collectively referred to as magnetic reconnection.

One special characteristic of magnetic reconnection is that the process can be typically self-driven. The ejection of plasma jets to the sides brings in more plasmas from above and below. Therefore, it can bring in more magnetic fields where magnetic reconnection occurs. This process can self-sufficiently sustain until its energy source is exhausted. So, there is considerably large amount of energy would be released during the evolution of magnetic reconnection.

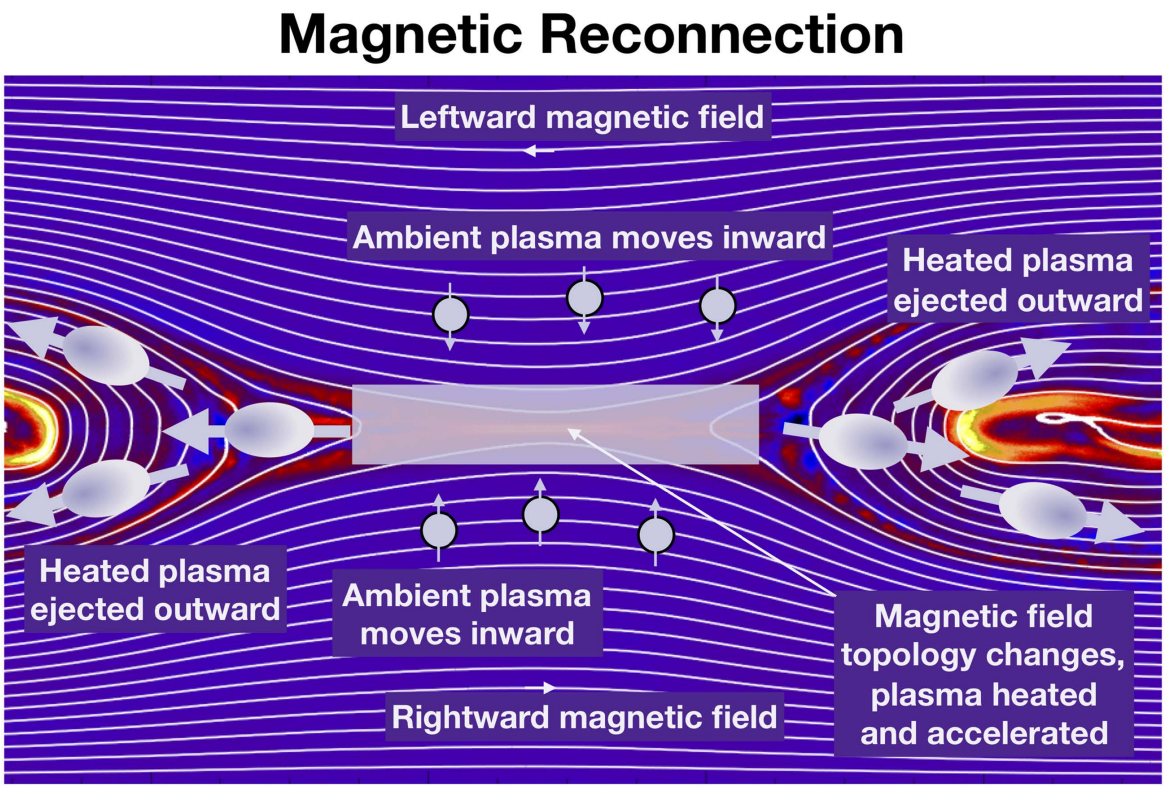

Fig. 2.1 Schematic diagram of magnetic reconnection processes[36].

2.2 Basic Models of Magnetic Reconnection

The description of magnetic reconnection is based on MHD theory, and began with relatively simple steady-state physical image. In 1950s, various models of magnetic reconnection had been proposed to describe it. Here, two important models are to be introduced.

2.2.1 Sweet-Parker Model

The Sweet-Parker model is the first one to quantitatively describe the magnetic reconnection based on MHD theory, and it was individually proposed by Parker in 1957 and Sweet in 1958. The schematic diagram of Sweet-Parker model is shown in the Fig. 2.2. The current sheet is assumed to locate in the diffusion region with a length of $2l$ and a width of 2δ. The inflow of plasma is in the z-direction, while the outflow is in the x-direction. The plasma enters into the diffusion region, and particles can be accelerated or heated by magnetic reconnection.

For the steady-state magnetic reconnection, the shape of current sheet and the distribution of plasma flow will not change during the evolution magnetic reconnection. According to conservation of mass, the mass of plasma entering into the diffusion region is equal to the one leaving from this region, which can be expressed as following:

$$\rho_{in} V_{in} l = \rho_{out} V_{out} \delta, \tag{2.1}$$

where ρ represents the mass densities of plasma, and V represents the velocity.

The pressure in the center of diffusion region can be obtained from Bernoulli equation:

$$p_z = p_{in} + \frac{B_{in}^2}{2\mu_0} + \frac{\rho_{in} V_{in}^2}{2} \tag{2.2}$$

$$p_x = p_{out} + \frac{B_{out}^2}{2\mu_0} + \frac{\rho_{out} V_{out}^2}{2}, \tag{2.3}$$

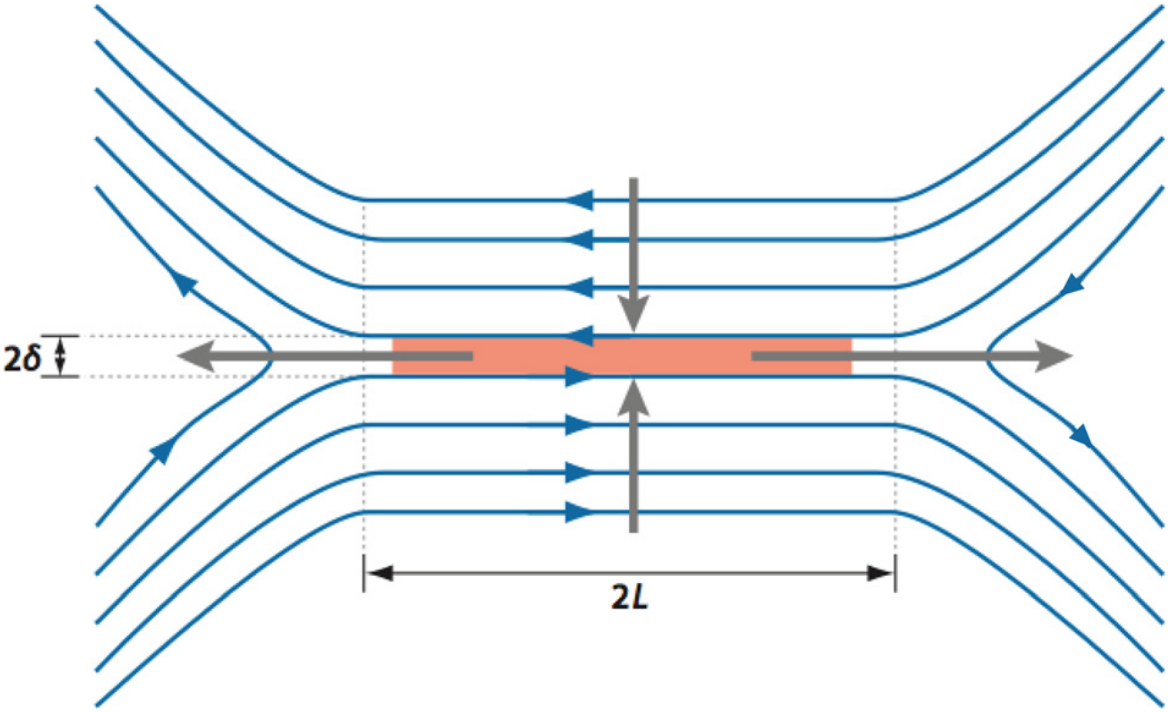

Fig. 2.2 Schematic diagram of Sweet-Parker model[1].

where p_z and p_x respectively represent pressures along the z-direction and x-direction in the center of diffusion region, p_{in} and p_{out} respectively represent pressures of inflow and outflow plasma.

In the Sweet-Parker model, the outflow velocity is much larger than the inflow velocity $V_{out} \gg V_{in}$ and the magnetic field in the inflow region is much larger than that in the outflow region $B_{in} \gg B_{out}$. For a steady-state magnetic reconnection, there is a relationship for pressure in the center of current sheet: $p_z = p_x$. According to Parker's further assumption: $\rho_{in} = \rho_{out}$, $p_{in} = p_{out}$, the derived outflow velocity is Alfven velocity:

$$V_{out} = V_A = \frac{B_{in}}{\sqrt{\mu_0 \rho_{out}}}. \tag{2.4}$$

In the diffusion region, the electric field can be obtained by Ohm law:

$$E = \eta J \tag{2.5}$$

where η is the electrical resistivity of diffusion region, and J is the current density of diffusion region. The relationship among the current density, inflow magnetic field, and width of current sheet can be derived:

$$J = \frac{B_{in}}{\mu_0 \delta}. \tag{2.6}$$

According to the above relationship, the inflow velocity then can be obtained as following:

$$V_{in} = \frac{\delta}{L} V_A = \frac{V_A}{\sqrt{S}}, \tag{2.7}$$

where $S = \mu_0 v_A L/\eta$ is the Lundquist number. The dimensionless Mach number is defined as reconnection ratio of magnetic reconnection,

$$M_A = \frac{V_{in}}{V_{out}} = \frac{1}{\sqrt{S}}. \tag{2.8}$$

For the solar corona, the Lundquist number is usually very large, with a magnitude of 10^{12}, which means that the reconnection ratio derived from the Sweet-Parker model is very small. So, this model is hard to explain the fast burst of solar flare.

2.2.2 Petschek Model

As mentioned above, the reconnection ratio of Sweet-Parker model is too small and it can only explain some slow processed of magnetic reconnection. In order to solve this problem, Petschek modified the Sweet-Parker model. The diffusion region is shortened ($L^* \ll L$) and the shock wave is introduced into the separatrix between the inflow and outflow regions. The reconnection ratio obtained by Petschek model is $\pi/8lnS$, much larger than the value obtained by Sweet-Parker model.

According to the above modification, magnetic reconnection can only occur in very small region, and a mass of particles in inflow region would be accelerated by not diffusion but shock wave and enter into outflow region. Thus, the magnetic energy can be converted into thermal and kinetic energy of particles by not only Jole heating but also shock wave.

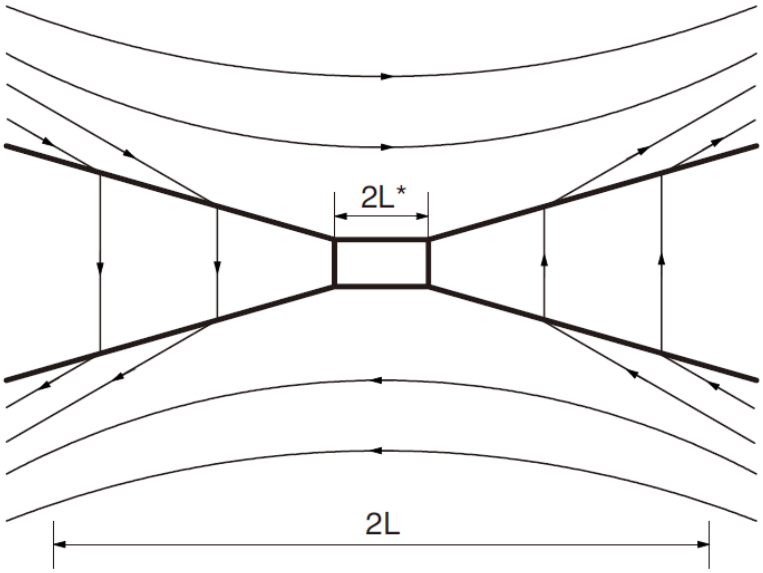

Fig. 2.3 Schematic diagram of Petschek model[1].

However, magnetic reconnection in Petschek model was found to be unstable according to numerical simulation, as the diffusion region would be rapidly elongated like the shape in Sweet-Parker model. Besides, there is some conflict between the generation of shock wave and assumption of small diffusion region, which is found by Biskamp in 1986. It means that there are still some imperfections in these magnetic reconnection models.

2.3 Collision-less Magnetic Reconnection Model

Inside the ion inertial region of collision-less magnetic reconnection, while ions are decoupled from the magnetic field lines, electrons are still frozen-in along these lines. The current in the reconnection plane is dominated by electron motion. In anti-parallel magnetic reconnection, electrons stream along the separatrix from the strong magnetic field region into the X-line region where electrons are accelerated by the reconnection electric field. The accelerated electrons flow out along the magnetic field lines on the inside of the separatrix. Thus, a current system is formed that streams out along the separatrix and flows into the X-line along these magnetic field lines inside the separatrix. The out-of-plane magnetic field created by the current system will be canceled, while a quadrupolar structure is formed inside the ion diffusion region.

The reconnection electric field, a quantity characterizing the reconnection rate, exists in the electron diffusion and magnetic pileup regions; the field center is situated at the X-point. According to the two-fluid model, the generalized Ohm's law can be deduced directly from the particle momentum equation,

$$E + V_i \times B = \frac{1}{ne} j \times B - \frac{m_e}{e}\frac{\mathrm{d}V_e}{\mathrm{d}t} - \frac{1}{ne}\nabla \cdot \mathscr{P}. \tag{2.9}$$

Different from the classical Ohm's law, the classical resistance term ηJ is replaced by the sum of three terms: the Hall term $\frac{1}{ne} j \times B$, the electron inertia term $-\frac{m_e}{e}\frac{\mathrm{d}V_e}{\mathrm{d}t}$, and the electron pressure tensor gradient term $-\frac{1}{ne}\nabla \cdot \mathscr{P}$.

In the collision-less model, two-liquid equation and generalized Ohm's law are employed, which means that the dynamic of ions and electrons should be taken into consideration. The Fig. 2.4 shows the schematic diagram of diffusion region after magnetic reconnection for the collision-less magnetic reconnection model. In the ion diffusion region, as shown in gray color, Hall effect term dominates among the generalized Ohm's law, and ions decoupling with the magnetic field can be treated as background with positive charge. The red dotted lines shows the electron flow. Electrons enter into the electron diffusion region along the

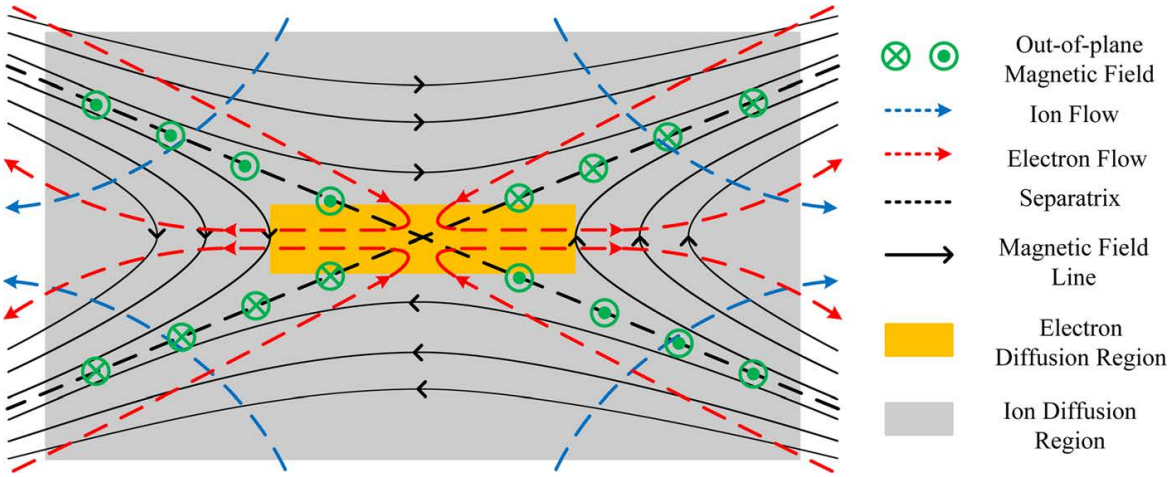

Fig. 2.4 Schematic diagram of collision-less magnetic reconnection model[1].

magnetic field, which is shown as the orange rectangular box in the Fig. 2.4, and then are accelerated by electrical field near the X-point. Finally, the accelerated electrons leave the diffusion region along the magnetic field. In the ion diffusion region, the dynamic movement of ions and electrons forms the Hall current, which would correspondingly generate Hall magnetic field perpendicular to the reconnection plate, as shown by the green marks. It is obvious that the Hall magnetic field has a quadrupolar structure according to the electron flow.

Hall effect is highly related to fast magnetic reconnection, as the reconnection ratio is obviously low when the Hall effect is not taken into consideration.

2.4 Means for Investigating Magnetic Reconnection

Numerical simulation can try different boundary conditions to investigate magnetic reconnection and it is relatively easier to perform. However, the results of simulation are limited by computational capability and algorithm, and it can not study the whole processes of magnetic reconnection, including macro and micro physics. There are some differences existing between simulation and real physics.

Magnetic reconnection occurs during solar flares, coronal mass ejections, and many other events in the solar atmosphere. The observational evidence for solar flares includes observations of inflow/outflow, down-flowing loops, and changes in the magnetic topology. In the past, observations of the solar atmosphere were done using remote imaging; consequently, the magnetic fields were inferred or extrapolated rather than observed directly. However, the first direct observations of solar magnetic reconnection were gathered in 2012 (and released in 2013) by the High-Resolution Coronal Imager.

Magnetic reconnection events that occur in the Earth's magnetosphere (in the day-side magneto-pause and in the magneto-tail) were observed by spacecrafts such as Cluster II and the Magnetosphere Multi-scale Mission. Cluster II is a four-spacecraft mission, with the four-spacecraft arranged in a tetrahedron to separate the spatial and temporal changes as the suite flies through space. It has observed numerous reconnection events in which the Earth's magnetic field reconnects with that of the Sun.

Magnetic reconnection has also been observed in numerous laboratory experiments. For example, studies on the LAPD at UCLA have observed and mapped quasi-separatrix layers near the magnetic reconnection region of a two flux rope system, while experiments on the Magnetic Reconnection Experiment (MRX) at the Princeton Plasma Physics Laboratory (PPPL) have confirmed many aspects of magnetic reconnection, including the Sweet–Parker model in regimes where the model is applicable.

The following Tab. 2.1 shows the advantages and disadvantages of different means for investigating magnetic reconnection. Even though the astronomical observation can provide data from the real magnetic reconnection in space plasmas, the information is not complete due to insufficiency of measurement points. The huge cost, passivity of measurement and uncontrolled experimental parameters make this method full of challenge.

For laboratory plasmas, the experimental devices can be especially designed, the plasma diagnostics are much easier installed, and the experimental conditions can also be relatively controlled. These advantages allow us to study the magnetic reconnection much more detailed.

Table 2.1 Advantages and disadvantages of different means for investigating magnetic reconnection

Means	Advantages	Disadvantages	Examples
Solar/Astrophysical plasmas	1.Observations of large-scale dynamics; 2.Parameter regimes inaccessible by experiment or simulation; 3.Detailed information on thermal properties of plasma.	1.No experimental control; 2.Limited to remote sensing; 3.Cannot directly observe small-scale physics; 4.Difficult to diagnose magnetic filed.	1.Solar/stellar flares and coronal mass ejections; 2.Interstellar medium and star formation regions; 3.Neutron star magnetosphere.
Space plasmas	1.Extremely detailed data at a few points; 2.Parameter regimes inaccessible to experiment; 3.Excellent for studying collision-less physics.	1.Difficult to connect observations to global dynamics; 2.Difficult to disentangle cause and effect; 3.No experimental control.	1.Cluster, THEMIS, Geotail, ACE, Wind, Ulysses, Voyagers 1/2; 2.Future: Magnetosphere Multi-scale Mission, Solar Probe Plus
Laboratory experiments	1.Probes inserted into plasmas directly (especially for $T \leq 20eV$); 2.Studying small-scale physics and global dynamics simultaneously; 3.Controlled experiments.	1.Relatively modest parameter regimes; 2.Modest separation of scales; 3.Results influenced by experimental method.	1.Tokamaks, spherical tokamaks, spheromaks, reversed field pinches, such as MRX, VTF, TS-3/4/6, UTST, SSX, RSX, CS-3D, and soon FLARE.

Chapter 3

Magnetic Reconnection Research in TS-6 Merging Experiments

3.1 Plasma Merging Experiments

For early research on magnetic reconnection before 1980, laboratory experiments were carried out in short-pulse plasmas or fast high-density pulsed plasma discharges of a few micro-seconds' duration. Even though the plasma diagnostics were not significantly developed, impressive and interesting results had been successively found. The reconnection rate was measured by Bratenahl and Yeates to be larger than the theoretical value calculated from classical model, resulting from micro-instabilities driven by electron drift against ions. Frank measured the current density profiles of the neutral sheet by magnetic probes.

Magnetic reconnection was also investigated in LCD, a linear plasma device in UCLA, and strong guide field was employed. The rapid formation of long thin current sheet was studied, and its thickness is inversely proportional to the magnitude of axial magnetic field. Further experiments also reveal that the current sheet is torn into multiple magnetic islands during magnetic reconnection with guided field. Electron heating is observed around the current sheet boundaries, and fluctuations in the plasma are found to have a significant effect

on the acceleration of ions. In addition, other issues such as resistivity, energy conversion, and current distribution in reconnection have also been investigated in detail.

With the development of plasma diagnostics and experimental methods, problem about magnetic reconnection, such as MHD instabilities, energy conversion, has been significantly studied. Merging of two torus plasmas was found to an effective experimental method to investigate magnetic reconnection. Two spherical tokamaks (STs) with opposing B_t are merged, forming X-point structures at their contacting points, as shown in the Fig. 3.1. Then, a new high-beta ST is formed by the use of high-power heating effect of magnetic reconnection (or two spheromaks are merged to form an FRC). The advantages of this method are as follows: (1) the merging/magnetic reconnection of two torus plasmas converts a part of the reconnecting magnetic energy into ion thermal energy, providing $MW \sim GW$ class ion heating power, (2) its heating time, almost equal to the Sweet–Parker time calculated from the anomalous resistivity at the reconnection X-point, is shorter than its energy confinement time, enabling us to form high T_i and high β torus plasmas, (3) its heating time is also shorter than the growth time of MHD instabilities, enabling us to test the stability of a variety of high β configurations formed by the reconnection heating.

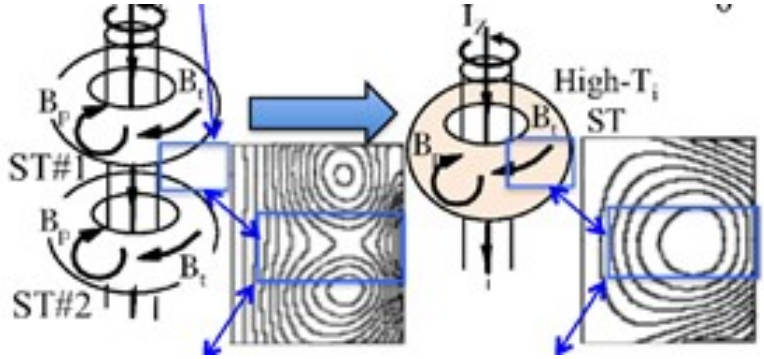

Fig. 3.1 Schematic diagram of tokamak plasma merging experiments.[3]

Merging of two torus plasmas is an effective method to investigate magnetic reconnection, which has been carried out on TS-3 (Tokyo University Spherical Torus Device No. 3) device[2] since 1986, and then this experimental method spreads to other devices all over the world, such as MRX[37], VTF[38], TS-4[39], MAST[40], and UTST[41]. The main devices for reconnection experiments are summarized in the Tab. 3.1.

Table 3.1 Main devices for reconnection experiments.

Device	Location	When	Geometry	Main features
3D-CS	Russia	1970	Linear	3D, heating
LPD, LAPD	UCLA	1980	Linear	Heating, waves
TS-3	U-Tokyo	1985	Merging	3D, Rate, heating
TS-4	U-Tokyo	1995	Merging	3D, Rate, heating
MRX	Princeton	1995	Merging	3D, heating, scaling
SSX	Swarthmore	1996	Merging	Heating
VTF	MIT	1998	Toroidal	Trigger
RSX	Los Alamos	2002	Linear	Boundary
RWX	Wisconsin	2002	Linear	Boundary
UTST	U-Tokyo	2008	Merging	Heating
TS-6	U-Tokyo	2017	Merging	3D, Rate, heating

3.2 Overview of TS-6 Merging Experiments

TS-3 had been upgraded to TS-6/TS-3U (Tokyo University Spherical Torus Device No. 6) in 2017[4, 5], with vacuum vessel of $\phi 0.75$ m $\times$ 1.44 m, as shown in the Fig. 3.2. Unlike general arrangements of other tokamak devices, TS-6 is transversely installed with the Z-axis parallel to the horizontal direction. The vacuum vessel is mainly made of stainless steel SUS-304, except for some glass windows, and there is no coating on the first wall. The TF coils can provide toroidal magnetic field up to 0.2 T. Plasma was first produced in 2018 spring, and various diagnostics have been or are being developed on TS-6. The main parameters of TS-6 are listed in the Tab. 3.2.

Table 3.2 Main parameters of TS-6 merging experiments.

Parameter	Value
Chamber diameter	0.75 m
Chamber height	1.44 m
Toroidal field (Guide field)	Up to 0.2 T
Ion temperature	$\sim 30-350$ eV
Electron temperature	$\sim 10-40$ eV
Electron density	$\sim 1\times 10^{20}$ m^{-3}

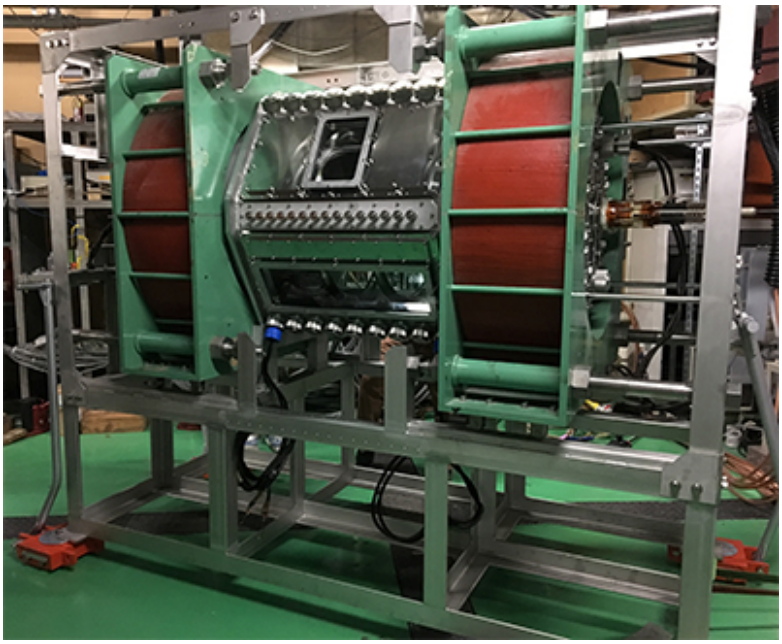

Fig. 3.2 Photograph of TS-6 merging device.

The cross-section of the TS-6 merging device is shown in the Fig. 3.3. Besides the main chamber, coil system is an important component for TS-6 merging device, whose detailed parameters and characteristics are listed in the Tab. 3.3.

Two ring-type poloidal field (PF) coils with a diameter of 0.44 m and a distance of 0.70 m are symmetrically installed on both sides of the middle plane inside the main chamber. The PF coils are designed to generate poloidal magnetic field, which would further generate parallel toroidal plasma currents of two spherical tokamak (ST) plasmas.

For experiments from 2019 to 2021, there is some malfunction with the PF coils, so the separation coils are employed to generate poloidal field instead. The separation coils with a diameter of 0.62 m and a distance of 0.60 m were designed to accelerate the merging of two ST plasmas. Since the malfunction of PF coils, the capacitance bank which should be used for PF coils is connected to the separation coils. For present experiments, the maximum charging voltage of PF is 39KV, and it would usually take about 160 seconds.

The toroidal field (TF) coils with 12 turns are installed outside and surrounding the main chamber of TS-6 device. In general, the maximum charging voltage of TF is 3.4 KV.

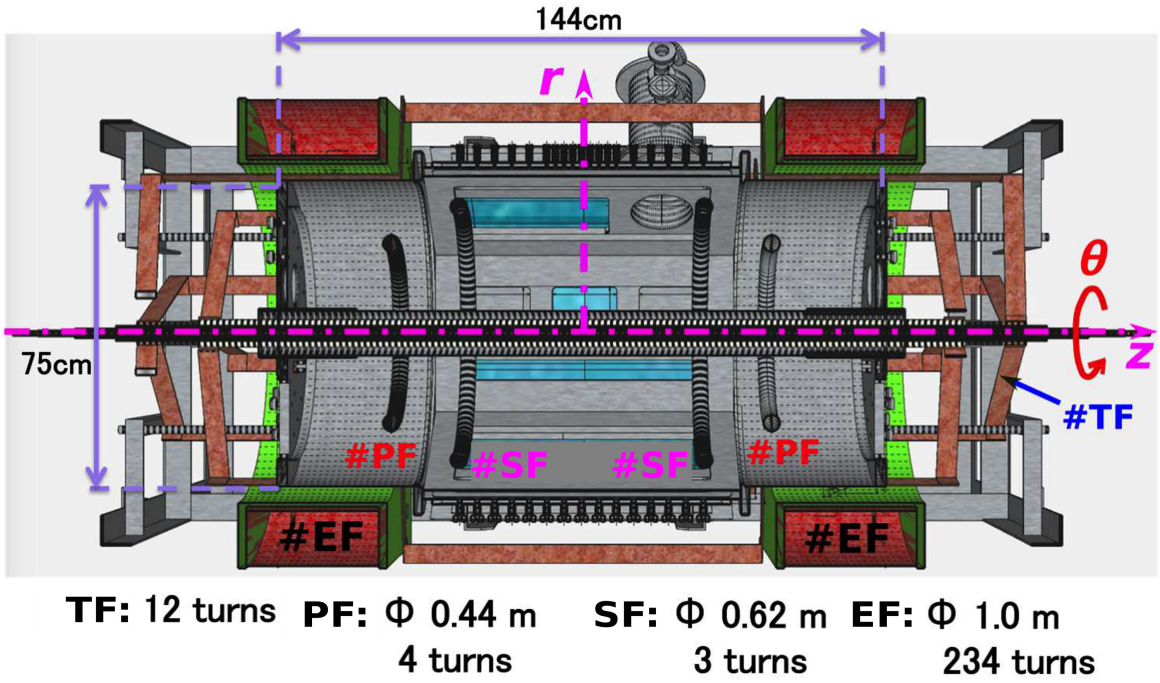

Fig. 3.3 Cross-section TS-6 merging device. The PF, TF, EF, CS, and separation coils are also shown in this figure.[42]

Recently, we had tried to charge the TF with a maximum voltage of 4 KV, and no accident happened.

The equilibrium field (EF) coils with a diameter of 1.00 m are employed to generate equilibrium field, which can better confine and maintain the plasmas inside the main chamber of TS-6. The EF coils are charged by a direct current (DC) power source with a maximum current of 150 A.

Even though the center solenoid (CS) coils have been installed in the center of the main chamber, they are only used for some special situation and CS-less merging experiments are the main operation mode in our laboratory.

Before the experiments, vacuum pressure and gas supply system should be checked to be in normal operation. The start time when the discharge button should be pushed is assumed to be $t = 0$ s.The Fig. 3.4 shows the current waveform of PF coils, TF coils, and plasma[43]. The discharge of TF coils starts from $t = 50$ μs and reach the peak at about $t = 500$ μs. As mentioned above, the TF coils would generate toroidal magnetic field for the two ST plasmas.

Table 3.3 Main parameters and characteristics of TS-6 coil system.

Coils	Diameter	Capacitance Bank	Rated Voltage	Maximum Charging Energy
Poloidal Field Coils	0.44 m	18.75 μF	40 KV	15 KJ
Separation Coils[1]	0.62 m	18.75 μF	40 KV	15 KJ
Toroidal field Coils	12 turns	8.3 mF	8 KV	266 KJ
Equilibrium field Coils	1.00 m	DC	-	-

[1] The capacitance bank which should be used for PF coils is connected to the separation coils

The discharge of PF coils starts from $t = 400$ μs and its change would induce a toroidal plasma current as shown in the Fig. 3.4.

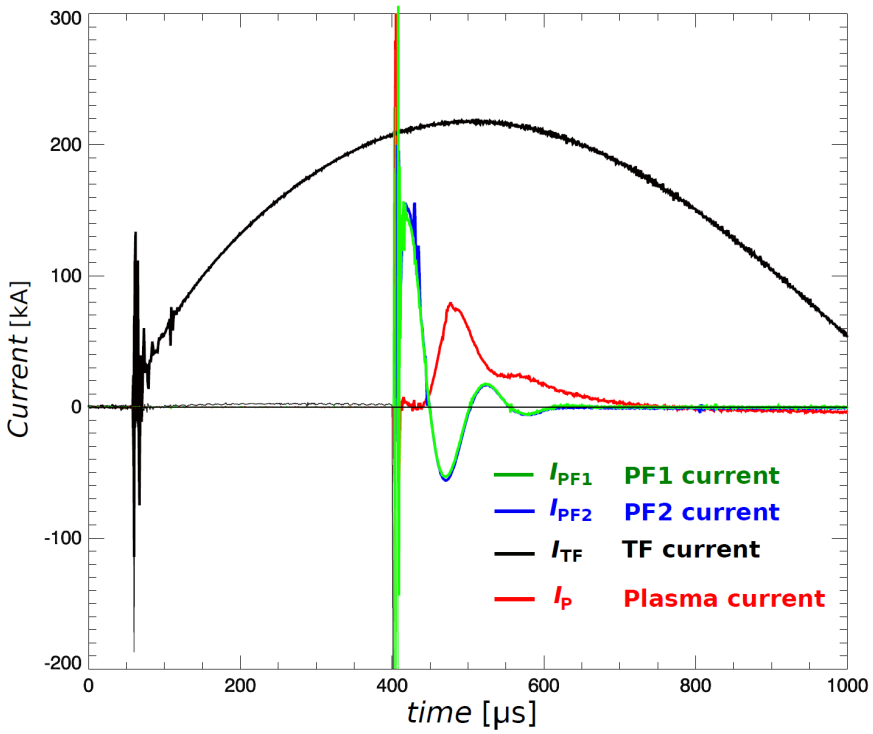

Fig. 3.4 The current waveform of PF coils, TF coils, and the plasma[43].

3.3 Plasma Diagnostics on TS-6 Merging Experiments

Some plasma diagnostic systems have already been developed on TS-6, such as Rogowski coil for measuring alternating current (AC), electrostatic probe for measuring electron temperature, density and electric potential. Here, the 2D magnetic probe system and ion Doppler spectroscopy are briefly introduced, as they are most frequently used on TS-6 merging experiments.

3.3.1 Magnetic Probe System

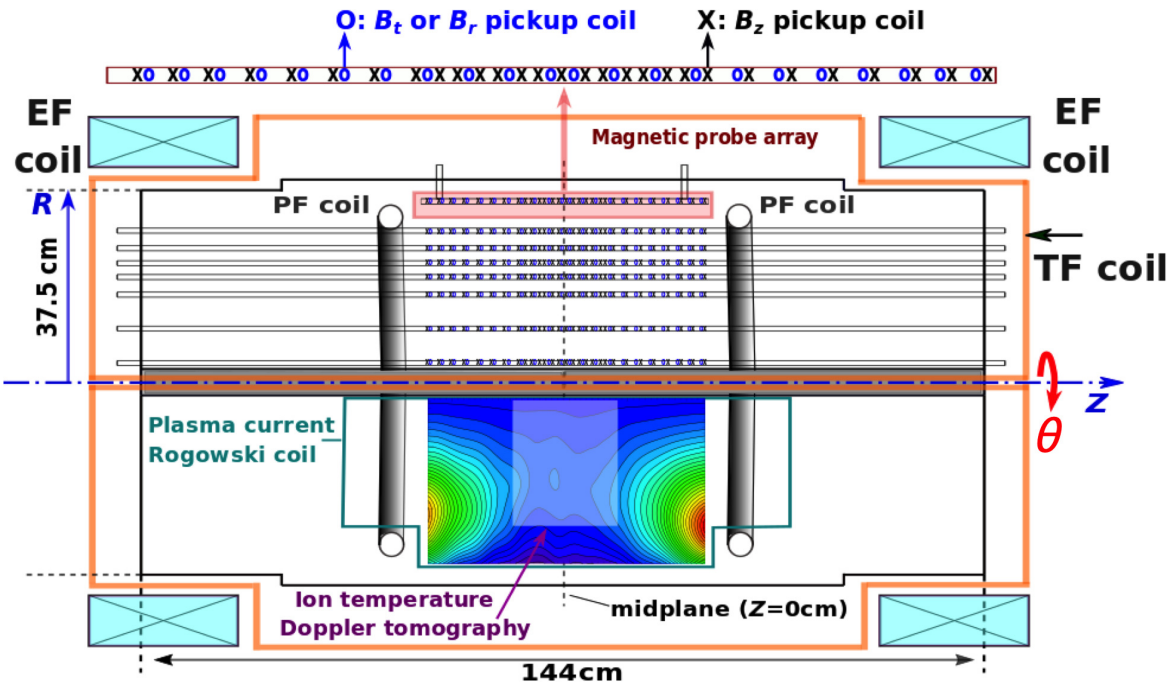

Fig. 3.5 Schematic drawing of the 2D magnetic probe system of the TS-6 device[43].

Magnetic probe system is an important diagnostic to reveal the magnetic filed flux, which is indispensable for investigating magnetic reconnection on TS-6[42]. 2D high-resolution magnetic probe array has been arranged in the $R-Z$ cross-section of TS-6 device to measure the B_z and B_r (or B_t) as shown in the Fig. 3.5. The magnetic probes are made of pickup

coils. The Tab. 3.4 shows the detailed parameters of the pickup coils. These pickup coils are tightly fixed on several holders, which are made a 3D printer with a high-resolution of 16 μm. Relying on the precision structure of both the pickup coils and holders, the spatial resolution of magnetic probe system is significantly improved.

Table 3.4 Detailed parameters of the pickup coils.

Pickup Coil	Structure	Number of Turns	Inner Diameter	Outer Diameter	Length
B_z	Hollow cylinder	300	1 mm	1.9 mm	5 mm
B_r[1]	Hollow ellipse	200	1 mm	2 mm	5 mm

[1] The width of the B_r pickup coil is 1.5 mm

3.3.2 Ion Doppler Tomographic Spectroscopy

The ion Doppler tomographic spectroscopy has already been developed on TS-6 device to measure the 2D profile of ion temperature and flow velocity, which would provide necessary information to study the ion heating and transport process during magnetic reconnection.

The Fig. 3.6.(a) schematically shows the arrangement of the present ion Doppler tomographic spectroscopy system with 288 channels. The 288-channel optical fibers (16CH radially, 18CH axially) are orderly arranged behind optical lens system (focal length: $f = 30$ mm, width: 7.5 mm, diameter: 25 25) to transmit visible light emitted from the plasma on the TS-6 device. Each optical fiber has a core diameter of 485 μm, total diameter of 500 μm (including the coating), and numerical aperture (NA) of 0.5. The other glass fibers (core diameter is 200 μm, total diameter including the coating is 240 μm, $NA = 0.2$) behind the former ones are used to relay the transmitted visible light signal. The spectrometer ($f = 1000$ mm, $NA = 0.06, F = 8.3, g = 1800$ L/mm) is employed to disperse the observed visible light, with a multi-slit (64×5, slit width=50 μm) system as shown in the Fig. 3.6.(b), which is able to rearrange and fix the relaying optical fibers. After the correction of the astigmatism through magnifying optics (meridional (λ) : $\times 2$, sagittal: $\times 0.68$), the dispersed visible light is recorded by a ICCD camera with a resolution of 1024×1024. The Fig. 3.6.(a)

also shows measured 288-channel line-integrated spectra of the H_α, which serves as an example of this diagnostic. The Fig. 3.6.(c) shows the lines of sight of the ion Doppler diagnostic system. The tangential view covers a cross-section from $R_{min} = 0.076$ m to $R_{max} = 0.27$ m.

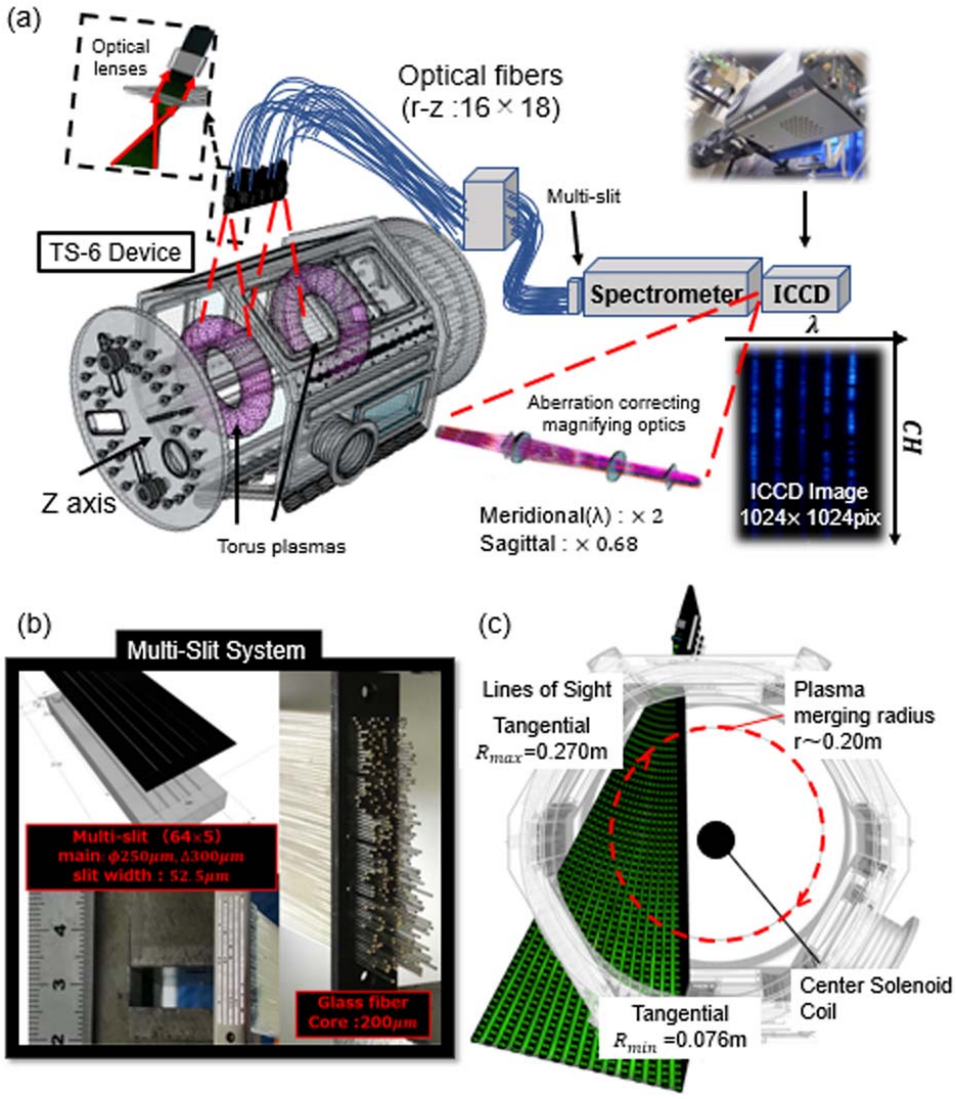

Fig. 3.6 (a) Schematic drawing of ion Doppler tomography spectroscopic system on TS-6 device. (b) Detailed structure of the multi-slit system. (c) Line-of-Sight (LOS) of ion Doppler spectroscopy in the cross-section of TS-6. LOS has tangential view from $R_{min} = 0.076$ m to $R_{max} = 0.27$ m.[44]

Chapter 4

Soft X-ray Tomographic Diagnostic in TS-6 Merging Experiments

Soft X-ray (SXR) diagnostic is an important non-invasive measurement technique, and it has been widely developed on most high-temperature plasma devices for investigating sawtooth instability[45], major and minor disruptions[46], MHD modes[47], impurity transport[48, 49] and so on. Many groups, such as LHD[50], TEXTOR[51], NSTX[52], RELAX[53] and QUEST[54], chose the tangential-view SXR imaging diagnostic for their fusion research. The basic concepts of SXR diagnostic are introduced first.

The design of SXR diagnostic which we developed in TS-6 merging experiments is introduced in detailed, including vacuum system, pinhole camera with MCP as detector, high-voltage pulse circuit, optical system, and high-speed imaging system. The above especially designed systems ensure the precision and reliability of the SXR diagnostic.

Tomography is an effective method for reconstruction, and it can mathematically reveal the local emissivity from line-integrated data for many kinds of plasma diagnostics, including SXR imaging measurement[11]. We developed a kind of tomographic method to obtain the local emissivity of SXR in TS-6 merging experiments to reveal the spacial distribution of high-energy electrons.

4.1 Soft X-ray Diagnostic in TS-6 Merging Experiments

4.1.1 Introduction to Soft X-ray Diagnostic

Soft X-rays are usually detected by silicon diodes which have an extremely fast time response, typically a fraction of a microsecond, and measure the integrated X-ray power above a threshold energy determined by a thin metallic foil, usually beryllium, placed in front of the detectors. The detectors receive most of their power from the hot dense plasma core and have proved invaluable in the study of MHD phenomena and impurity transport effects. The main advantage of this diagnostic is its excellent spatial and temporal resolution. Many detailed studies of tokamak plasmas have been made particularly of the sawtooth in-stability, major and minor disruptions, MHD modes, high-β MHD effects, impurity transports, the snake and pellet injection. Heavy impurities will radiate significantly in the soft X-ray range, through line radiation, recombination radiation, and the Z_{eff} dependence in the bremsstrahlung. Soft X-ray diagnostic is therefore suitable for localizing the radiation of heavy impurities and in case of impurity injection can also be used for particle transport analysis, given the dependence of the emission profile on particle transport parameters.

Surface barrier detector (SBD) is widely employed to observe soft X-ray. Silicon diode solid-state detectors have been the first choice for Soft X-ray detector arrays for several years primarily because of their low cost and simplicity of operation. Unless the detectors are to be placed in the primary machine vacuum, an X-ray filter has to combine its role with that of a vacuum interface. For example, beryllium is particularly suitable, combining strength with good X-ray transmission, free from any absorption edges above a few hundred eV. The electronics associated with soft X-ray diode arrays often represents a major, if not dominant, component of the total system cost. The simultaneous requirements of low noise, high gain, high linearity, and high time resolution place strong demands on system design. The Fig. 4.1 shows the schematic diagram of SXR diagnostic in the toroidal pinch experiment RX (TPE-RX)[55]. It is a typical SXR imaging system with array detectors.

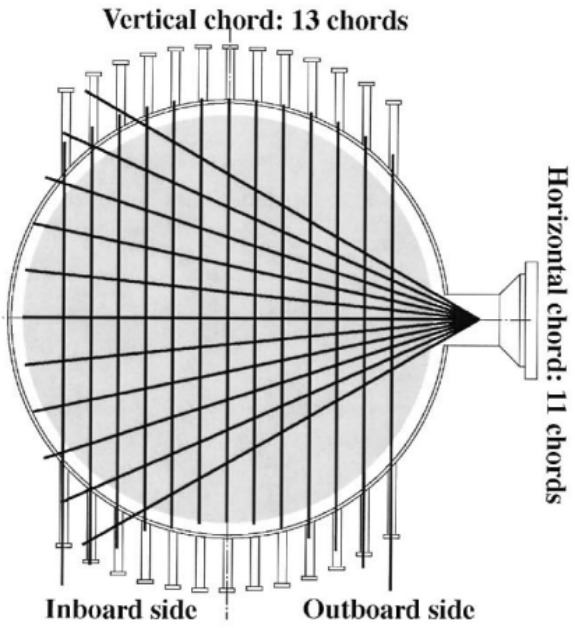

Fig. 4.1 Experimental setup for SXR imaging system in the toroidal pinch experiment RX (TPE-RX). Thirteen and eleven SBDs are respectively installed on the vertical port and horizontal port[55].

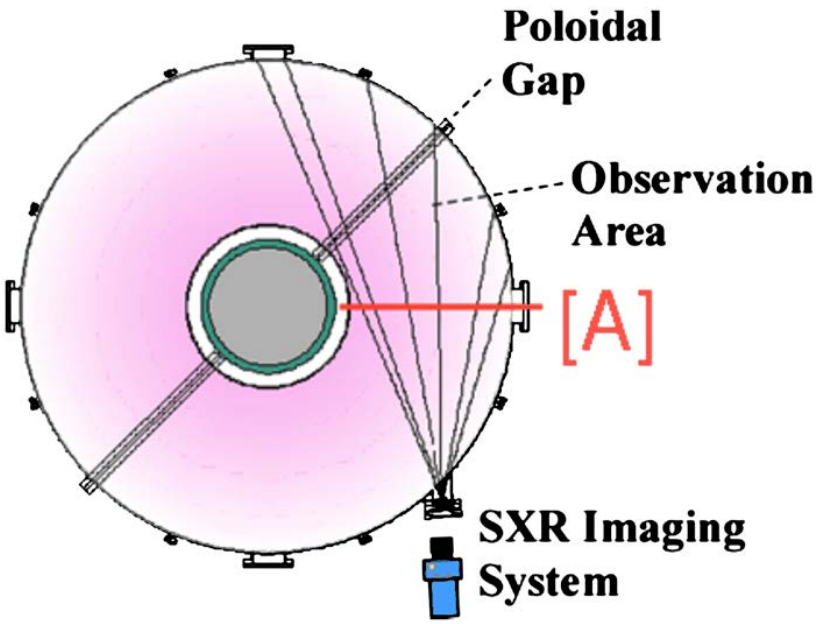

Fig. 4.2 Schematic diagram of tangential SXR imaging system in the RELAX device[56].

Tangential-view SXR diagnostic is another typical SXR imaging system. This kind of SXR diagnostic usually occupies less space of flange or port and has more lines of sight. The Fig. 4.2 shows the schematic diagram of tangential SXR imaging system in the RELAX device[56]. The micro-channel plate serves as the detector and one whole poloidal cross-section can be observed.

4.1.2 Design of Soft X-ray Diagnostic in TS-6 Merging Experiments

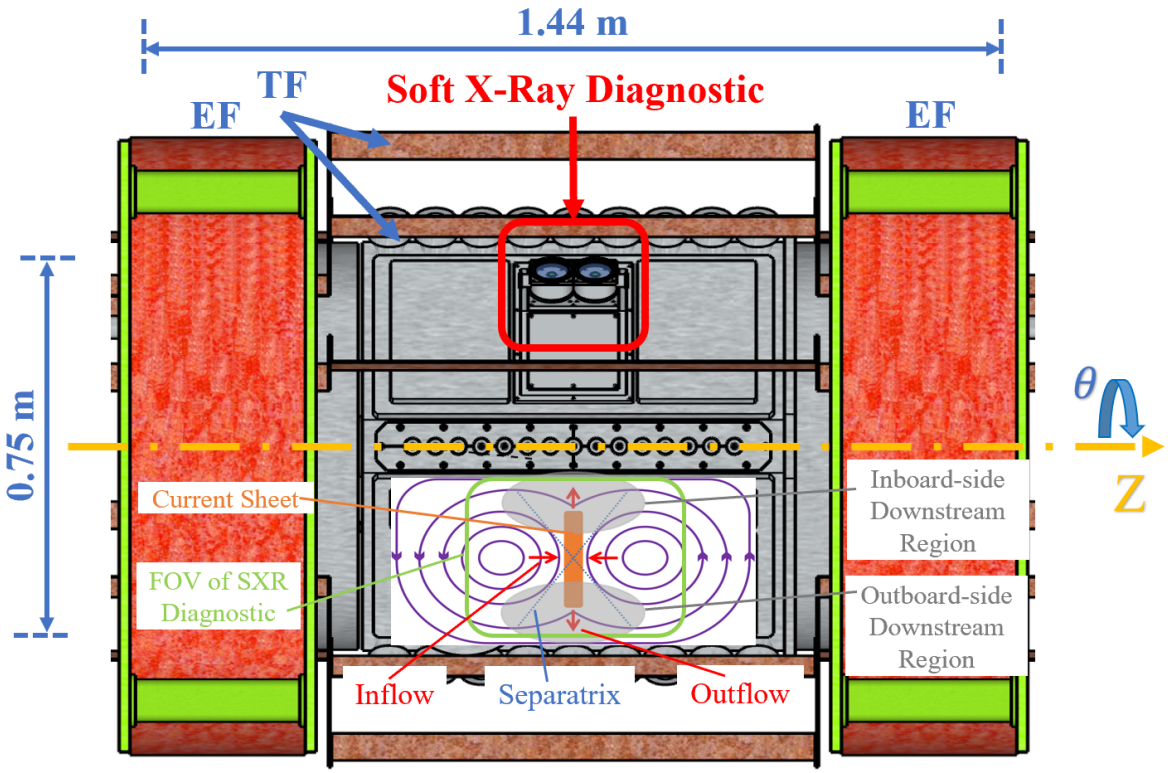

Fig. 4.3 Assembly drawing of TS-6 merging device with two MCP chambers and magnetic field lines of two merging ST plasmas. The red solid line box shows the position of MCP chambers; The purple solid lines represent magnetic field lines of two merging ST plasmas; The green solid line box shows the measurement region of this SXR diagnostic; The gray shades show downstream regions.

In TS-6 spherical tokamak (ST) merging experiments, SXR are to be emitted from high-energy electrons, which are accelerated during the evolution of magnetic reconnection. An innovative tangential-view SXR diagnostic to measure SXR with different energy ranges

has been developed as a key diagnostic in order to more accurately understand high-electron issues such as acceleration mechanism. Multiple micro-channel plates (MCPs) equipped with different filters are installed on TS-6 device, to focus on a whole cross-section of plasma. Using this diagnostic, distribution of accelerated electrons with different energy ranges can be distinguished. The assembly drawing of TS-6 merging device with the SXR diagnostic and magnetic field lines of two merging ST plasmas is shown in the Fig. 4.3. The green solid line box shows the measurement region of this SXR diagnostic, which covers the objective region where magnetic reconnection would occur.

First, the design of this multi-filter SXR diagnostic is introduced in detailed, including pinhole camera with MCPs as detectors, vacuum system, high-voltage pulse circuit, high-speed imaging system, and characteristics of filters. For the imaging system, the obtained raw images are line integrals of local emissivity of SXR along each line of sight. Tomography method based on the Phillips-Tikhonov regularization[12] is employed in order to obtain local emissivity of SXR, which reflects the spatial distribution of high-energy electrons.

Pinhole Camera

Soft X-ray emitted from the merging ST plasmas can enter into the MCP chamber through the pinhole in front of the chamber, as shown in the Fig. 4.4. The orange dash lines represent the lines of sight, and red dash line shows the position of focused cross-section. This SXR diagnostic is able to observe a whole cross-section due to special arrangement of location and viewing angle.

In order to explain the internal structure and operation principle of this pinhole camera, the magnified schematic diagram of MCP chamber is shown in the Fig. 4.5. The diameter of each pinhole is 1 mm, and a filter is used to cover and seal the pinhole. The filter can keep out photons with low energy, to avoid unexpected noise caused by light of other wavelengths, such as visible light, infrared light. The characteristics of filter will be discussed hereinafter. The SXR can motivate the MCP to generate photo-electrons, which would be accelerated by high-voltage electrical field. Finally, the photo-electrons strike the phosphor plate and then visible light is emitted. The SXR signal is amplified by the MCP and converted to visible light, which is observed by a small S-mount lens (focal length $f = 2.5$ mm) at the end of the

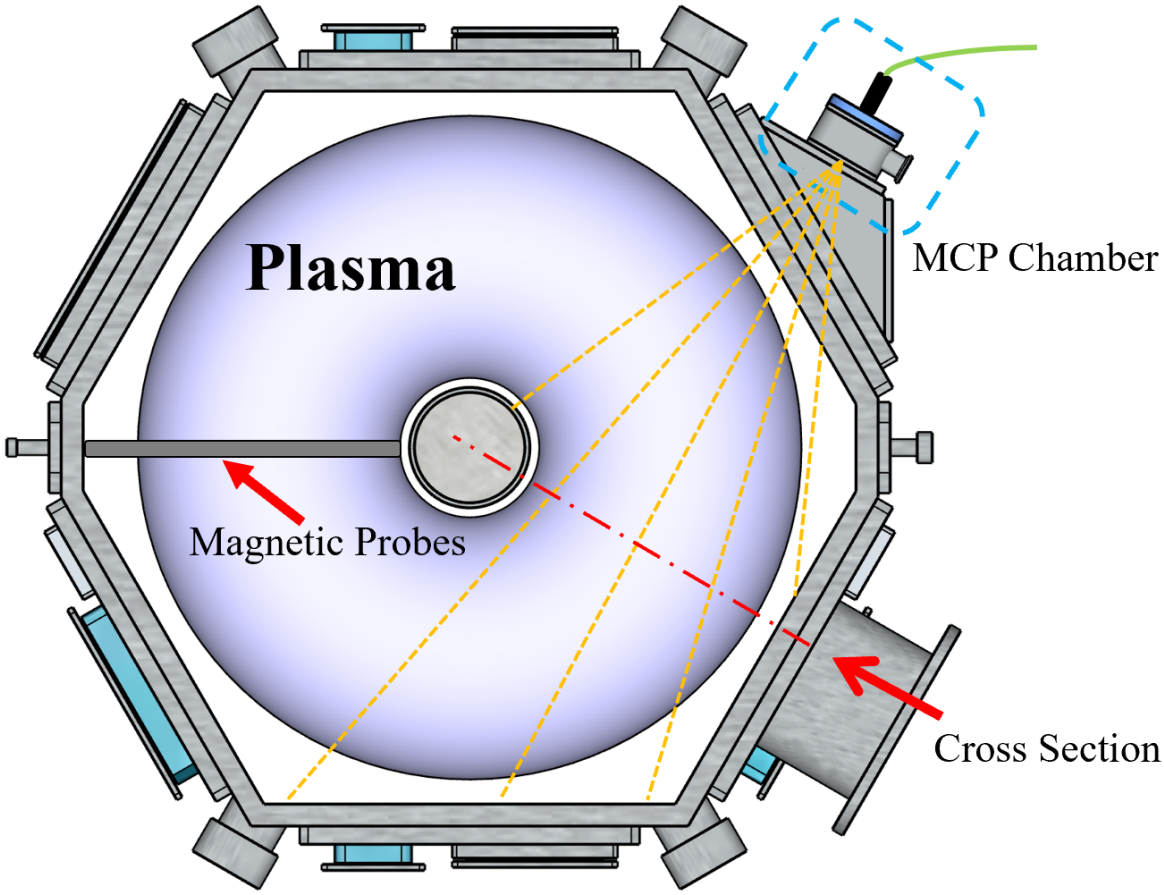

Fig. 4.4 Schematic drawing of TS-6 merging experiments from Z-direction and field of viewing of the SXR diagnostic on TS-6. The orange dash lines represent the lines of sight, and red dash line shows the position of focused cross-section.

phosphor plate. Images appearing on the phosphor plate are to be miniaturized by this lens and transferred to a high speed imaging system through long optical fiber bundles (numerical aperture $NA = 0.45$). Each fiber bundle consists of 6000 fibers.

Fig. 4.6 shows a photograph of one MCP vacuum chamber, MCP, S-mount lens, and fiber bundle. An especially designed connector is employed to connect a fiber bundle and a S-mount lens, and it can also serve as a support to fix the lens behind the glass window of the MCP chamber.

High-Voltage Pulse Circuit

As the electron temperature of plasma in our test discharges is relatively low, only about 10 eV, the SXR signal emitted from plasma during magnetic reconnection is not strong

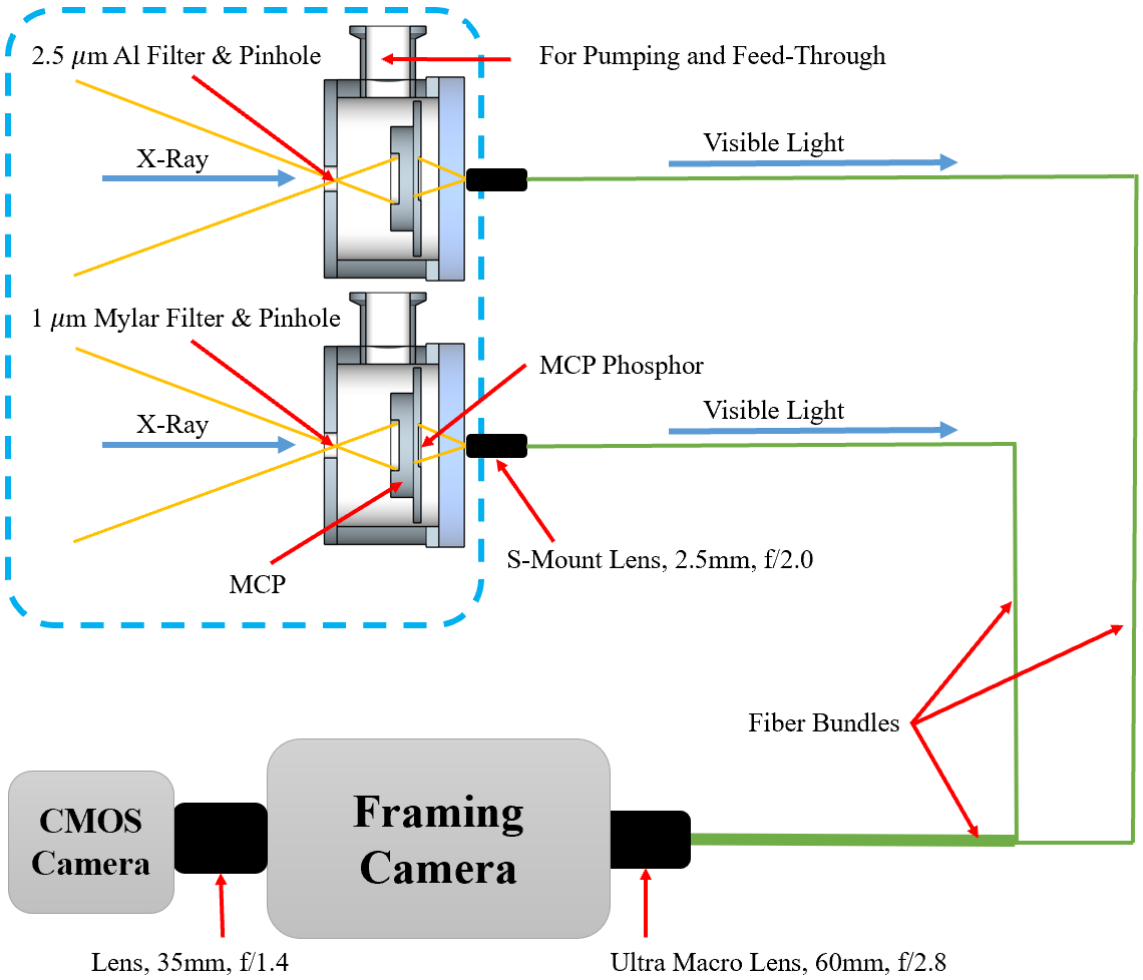

Fig. 4.5 Schematic diagram of pinhole camera and imaging system. The blue dash line box shows the magnified MCP chambers in the Fig. 4.4.

enough to be detected directly. In this diagnostic, we had employed two MCPs (model number: HAMAMATSU F2222-21P-Y010) to amplify the SXR signal by applying high bias voltage to MCP electrodes. The type of MCP in this diagnostic is 2 stage, and the MCP has a phosphor plate with a diameter of 17 mm. The phosphor type is P46, of which the 10% delay time is $0.2 \sim 0.4$ μs. On the other hand, the MCP equipped with phosphor plate is also able to convert SXR signal to visible light, whose images transferred by optical fiber bundles are observed and recorded by a high speed imaging system.

In this diagnostic, MCPs are driven by a high-voltage pulse circuit, as shown in the Fig. 4.7. High-voltage DC power supplies provide $+3 \sim +4$ kV for MCP-phosphor electrode

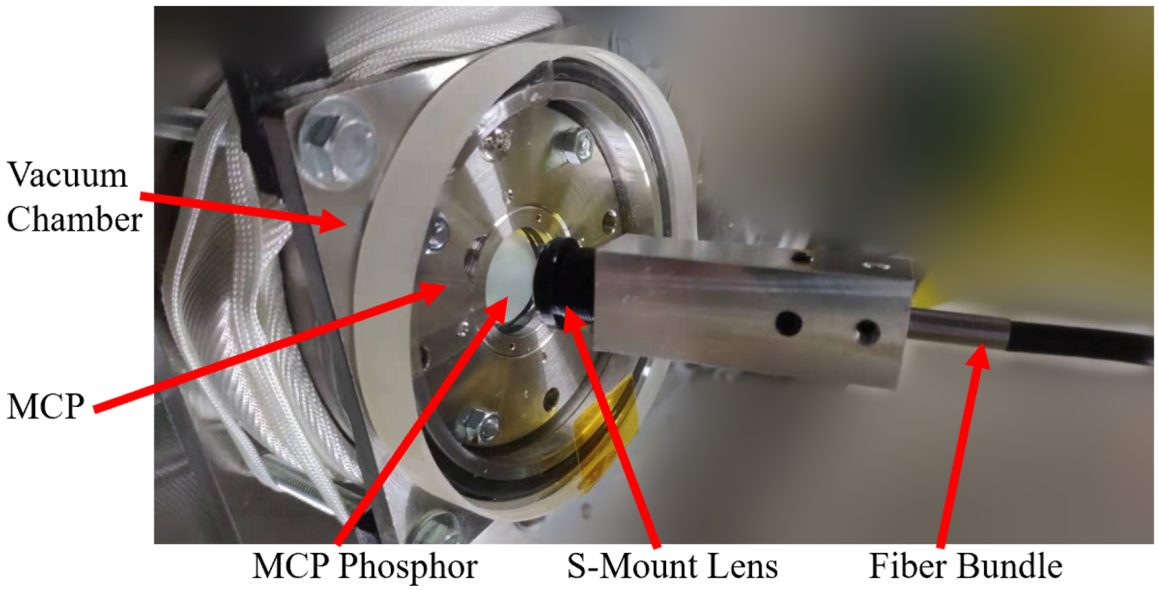

Fig. 4.6 Photograph of one vacuum chamber, MCP, S-mount lens, and fiber bundle.

and $-1.5 \sim -2$ kV for MCP-in electrode, which makes the gain of MCPs large enough. As unexpected currents inducted by the rapid change of TS-6 magnetic field at the beginning and end of experiments will cause noise and damage to the MCPs, the circuit is only switched on when safe, which is achieved and controlled by a pulse generator (model number: Princeton Instruments PG-10), gate drivers (series number: PS9531), and MOSFETs (series number: IXTT02N450HV). Test discharges with different magnetic fields had been carried out to check if the MCPs would be negatively influenced by magnetic fields, and neither obvious problem nor extra noise was found, which further verifies that this circuit can meet the requirements for experiments on TS-6.

Vacuum System

As the first stage of SXR diagnostic on TS-6, we had installed two MCPs on the same toroidal position to focus on one same cross-section of plasma, as shown in the red solid line box of Fig. 4.4. The MCPs should work in high vacuum condition, with vacuum pressure less than 1.3×10^{-4} Pa. In order to satisfy the operation requirement of MCPs, we designed separate vacuum chambers to isolate the MCPs with main chamber of TS-6, and an extra turbo molecular pump (TMP) is employed to maintain high vacuum condition, as shown in the Fig. 4.8. On the other hand, the thick ($\sim$5 mm) SUS-304 vacuum chambers can also keep

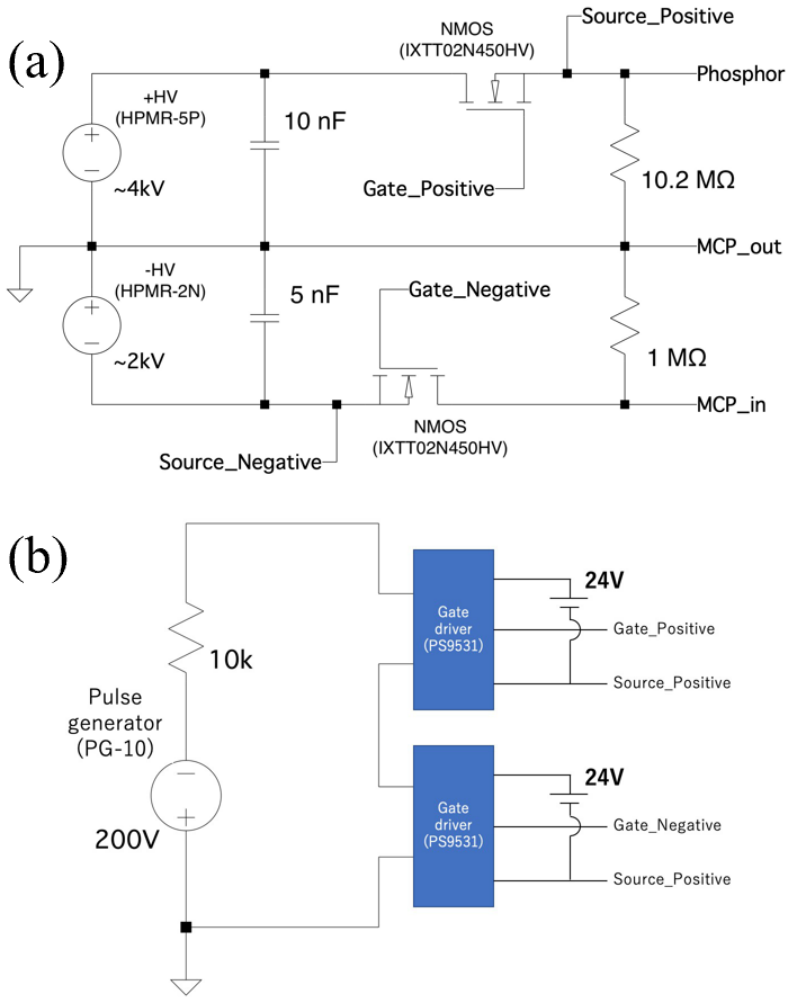

Fig. 4.7 Schematic diagram of high-voltage pulse circuit for driving MCPs. (a) The high-voltage power supply circuit. (b) The pulse generation circuit to control the MOSFET in the (a) (Provided by Mr. Takeda).

the MCPs fully shielded from the magnetic field whose frequency is about 10∼100 kHz. The field of view (FOV) of this SXR diagnostic is shown in the Fig. 4.4, and the orange dash lines represent the lines of sight. The FOV is able to cover one whole cross-section of plasma, and avoids areas where there are magnetic probes. The blue dash line box in the Fig. 4.4 also shows the position of MCP chambers. The two MCPs are installed on the two MCP chambers respectively, and the KF/NW-type flanges are used for pumping and high-voltage feed-through. Detailed structure of the MCP chamber and imaging process are shown in the Fig. 4.5.

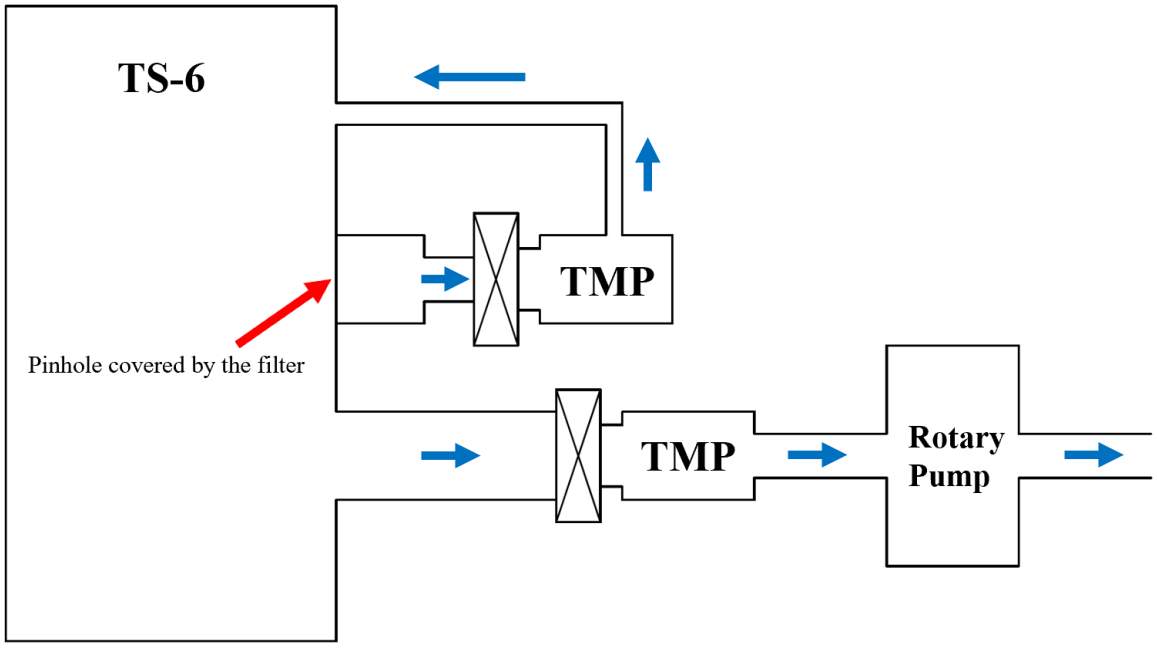

Fig. 4.8 Schematic diagram of the vacuum system.

Before experiments, we pump these MCP chambers and plasma main chamber simultaneously by a rotary and turbo molecular pump (TMP) to avoid destroying the filter, and the vacuum pressure can reach about 2×10^{-5} Torr. Then, we use an extra TMP to pump the MCP chambers individually until its vacuum pressure can reach about 1×10^{-6} Torr. During plasma discharges, the gas pressure in TS-6 plasma chamber is not more than 10^{-3} Torr. So, the pressure difference between the two sides of the thin filter is maintained quite small (no more than 10^{-3} Torr) throughout the whole process to ensure not to destroy the filters.

High Speed Imaging System

The high speed imaging system mainly consists of a framing camera (model number: HAMAMATSU C4187) and a CMOS camera (model number: HAMAMATSU C11440-36U). The frame interval of the framing camera can be 300 ns to 10 ms, which makes it possible to measure the evolution of SXR during magnetic reconnection in TS-6 ST merging experiments. As shown in the Fig. 4.5, images transferred from fiber bundles are gathered together on the end-interface of fiber bundles. These miniaturized images are to be observed by the ultra-macro lens (LAOWA, AF-S, 60mm, f/2.8, 2×Ultra-Macro), mounted in front of the framing camera. Fig. 4.9 is the photograph of the high speed imaging system. The

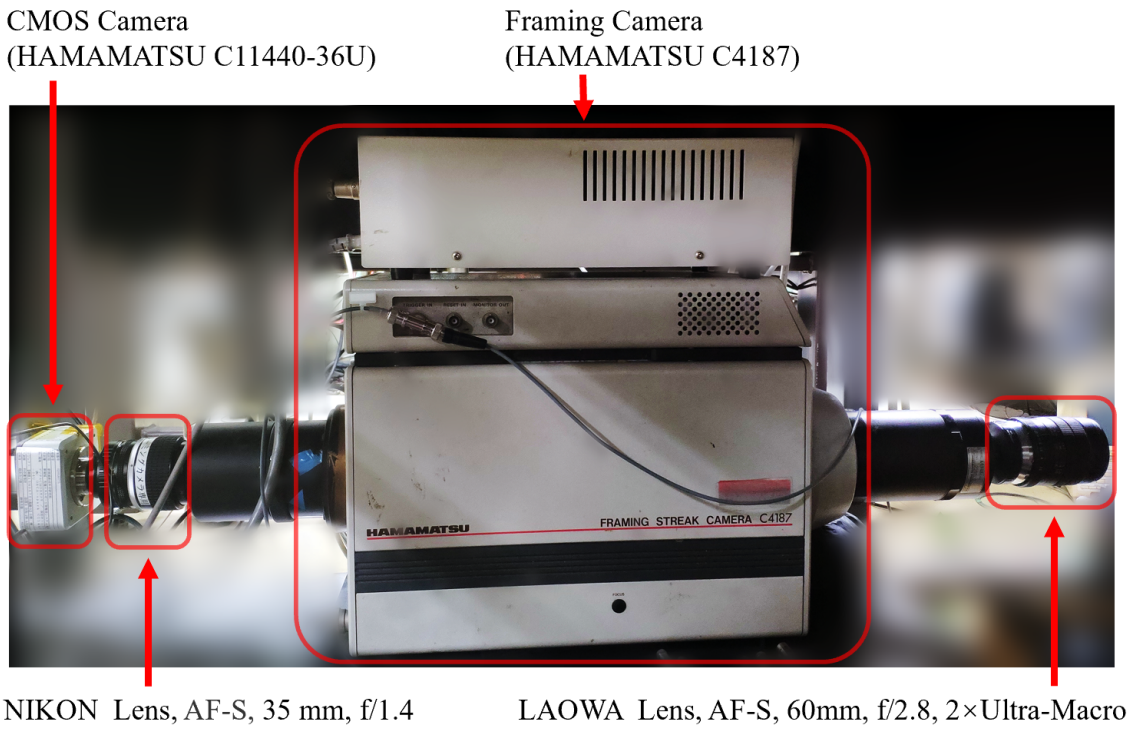

Fig. 4.9 Photograph of the high speed imaging system, including a framing camera, a CMOS camera, and lenses.

magnification ratio of the ultra-macro lens can be up to 2, so this lens is able to sufficiently magnify observed images. The framing camera acquires incident images and outputs up to 8-frame images with a certain frame interval on its fluorescent screen. As the framing camera is much more like an optical system without CMOS/CCD sensor, its output images are to be recorded by the CMOS camera through a camera lens (NIKON, AF-S, 35 mm, f/1.4), and stored in a controlling computer. In our merging experiments, frame intervals of 5 μs and 10 μs are most often used, and pixel number of each image is 230×230. The Fig. 4.3(e) shows an example of raw image of SXR recorded by the CMOS camera.

Characteristics of Filters

At first, the energy dependence of MCP detectors should be discussed, as we use MCPs to measure SXR signal with different energy range. Fig. 4.10 shows the relative MCP response as measured in two separate detector systems. The MCP response for SXR basically decreases with the photon energy increases. It means that the MCP is relatively more sensitive to SXR with lower photon energy.

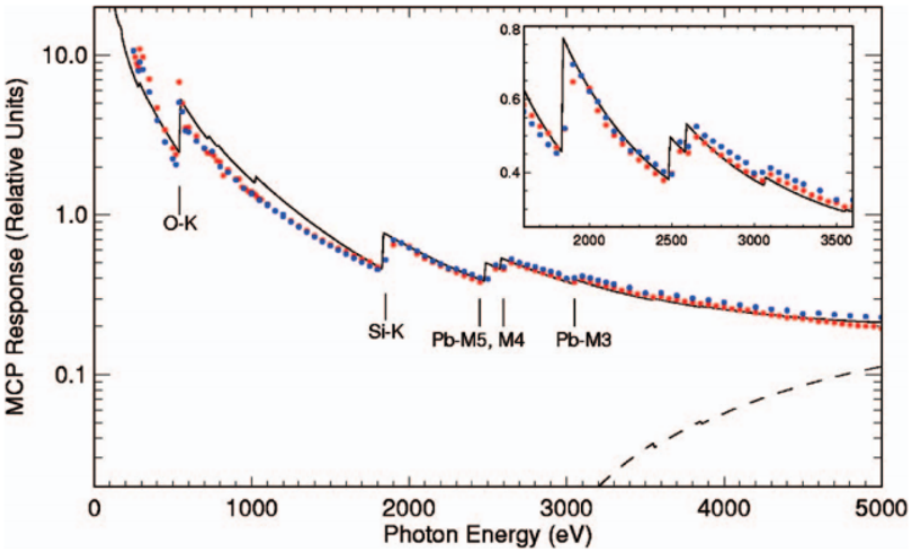

Fig. 4.10 Energy dependence of MCP. Dots in red and blue color show the relative MCP response as measured in two separate detector systems.[57]

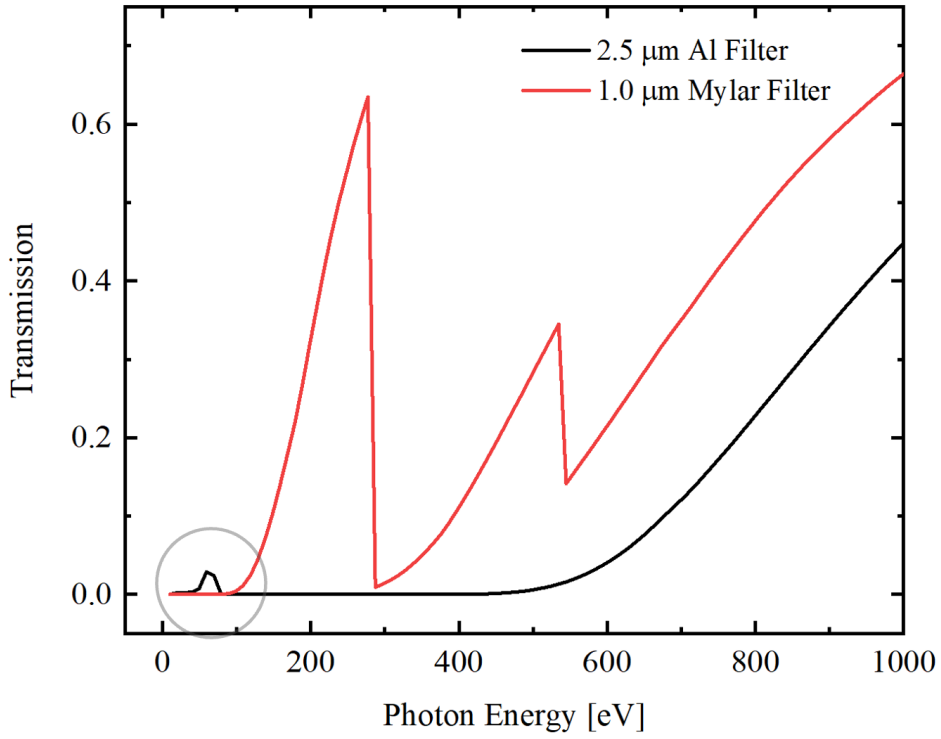

Fig. 4.11 Transmissions of 2.5 μm Al filter and 1 μm Mylar filter as a function of photon energy.

As mentioned above, 1 μm Mylar filter and 2.5 μm Aluminum (Al) filter are employed in this diagnostic, in order to filter out SXR with different energy ranges. The transmission characteristics[58] are shown in the Fig. 4.11. The 1 μm Mylar filter is able to resist photons with energy lower than 100 eV, to make sure that the measured signal is SXR, rather than other kind of light. As for the 2.5 μm Al filter, it can be used to measure SXR with energy higher than 400 eV. On the other hand, the MCP response for SXR generally decreases with the photon energy increases[57]. Therefore, if the photon energy of SXR is much higher than 400 eV, then the intensity of signal from the Al-filter MCP chamber should be weaker than the Mylar-filter one, and the extreme ultraviolet (EUV) signal emitted from plasma can be negligible. In TS-6 merging experiments, we found that the intensity of signal from Al-filter MCP chamber is relatively stronger than the Mylar-filter one. This result means that the energy of SXR emitted from plasma during magnetic reconnection is just a little higher than 100 eV, and the energy of signal from Al-filter MCP chamber is mainly in the range between 20 eV and 100 eV, belonging to EUV, as shown in the dark circle in the Fig. 4.11. Owing to the use of different filters, the energy range of SXR on TS-6 is successfully determined to be higher than 100 eV but lower than 400 eV.

4.1.3 Calibration of Imaging System

As for the high-speed camera system in the present SXR diagnostic, 8-frames mode is most usually employed in the plasma merging experiments on TS-6. So, there are eight sub-images in one whole image which is recorded by the CMOS camera. For the double MCP measurement system, two phosphor plates are focused and there should be two sub-sub-images for each sub-image. Therefore, there would be 16 sub-images recorded in one whole image at one timing, as shown in the Fig. 4.12. The original object of these images are just a light source, and they shows the position of fiber bundles in the whole image. We use these images which are presented in complete circle shape to calibrate the position of each fiber bundle.

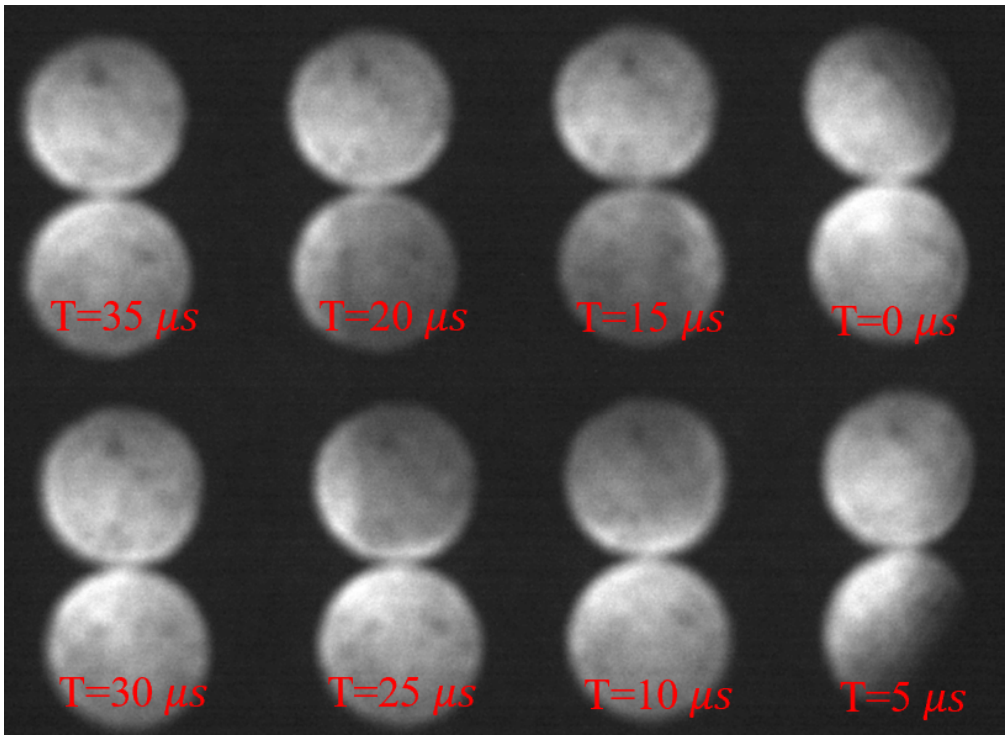

Fig. 4.12 Calibration of positions of 16 images shown on the MCP phosphor plates at different timings.

There is always distortion for each fiber bundle, as it is too long. So, the images which are transmitted to the end surface of fiber bundle would be upside down or askew, compared with the images in the front surface. It is necessary to calibrate the direction of the fiber bundles. Otherwise, we can not determine the correct direction of images, compared with the real observation object. On the other hand, the direction of images would also change because of the imaging principle of other optical system, including the pinhole camera.

In order to solve the above problem, we use a screen to calibrate the direction of images. As shown in the Fig. 4.13.(a), the picture on the right side is the recorded image of the original observation object, an icon. The above method helps us find a general direction relationship between the images and observation object. Then, we use black and white stripes to further determine and calibrate the exact direction of images, as shown in the Fig. 4.13.

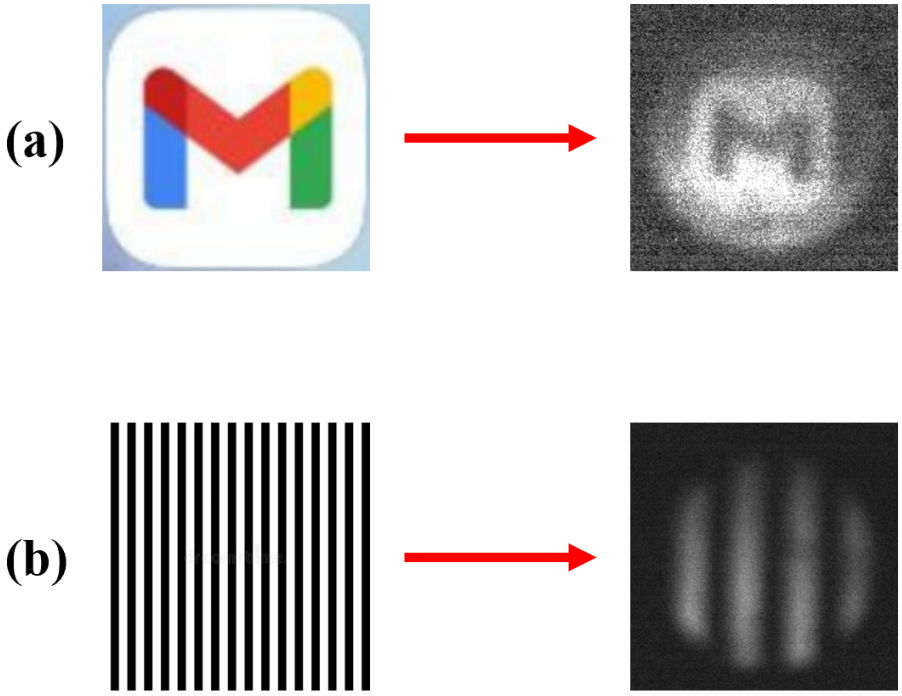

Fig. 4.13 Calibration of image direction. The pictures on the left side are original objects, while the ones on the right side are recorded images.

4.2 Determination of SXR Energy

According to the results measured by other diagnostics such as Langmuir probe and ion Doppler spectroscopy, the initial ST plasmas of present test discharges has the bulk plasma parameters: $T_e \approx 10$ eV,$T_i \approx 30$ eV, $n_e \approx 1 \times 10^{20}$ m^{-3}. As the bulk electron temperature is much lower than the energy range of SXR, SXR is therefore considered to be emitted from bremsstrahlung of electrons with high kinetic energy accelerated by reconnection electric field during magnetic reconnection.

As mentioned above, a 1 μm Mylar filter and a 2.5 μm aluminum (Al) filter are employed in this diagnostic in order to filter out SXR with different energy ranges. The transmission characteristics are shown in Fig. 4.11. The 1 μm Mylar filter can resist photons with energy lower than 100 eV to make sure that the measured signal is only SXR, rather than other kind of light. As for the 2.5 μm Al filter, it can be used to measure SXR with energy higher than 400 eV. Therefore, if the photon energy of SXR is much higher than 400 eV, then the

intensity of the signal from the Al-filter MCP chamber should be weaker than the Mylar-filter one, and the extreme ultraviolet (EUV) signal emitted from the plasma can be negligible.

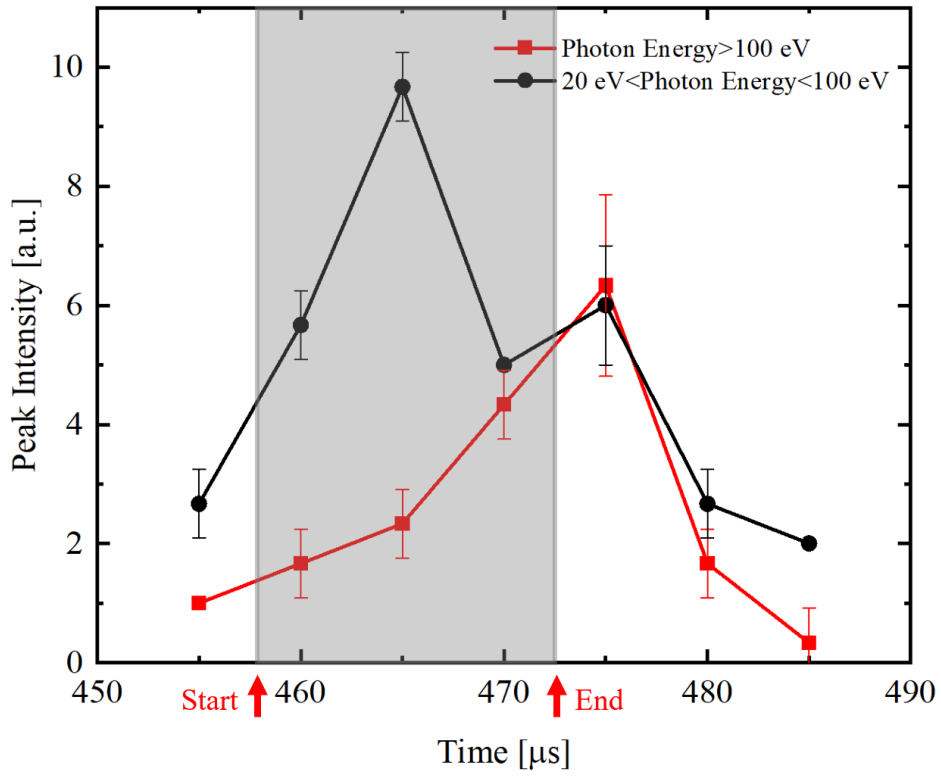

Fig. 4.14 Time evolutions of peak intensities of SXR (Photon Energy > 100 eV) measured through 1.0 μm Mylar filter in downstream regions and EUV light (20 eV < Photon Energy < 100 eV) measured through 2.5 μm Al filter.

As the SXR emission is overall not high and concentrates on particular regions, peak intensities at different moments are employed to relatively reflect the evolution of emission intensity, which are obtained by calculating average value of some brightest points in measured images. Fig. 4.14 shows the peak intensity of photons in downstream regions with different energy ranges, which is measured by this SXR diagnostic in the two ST plasma merging experiments. Photons with energy from 20 eV to 100 eV (EUV light) are detected and reach the maximum amount during magnetic reconnection, as shown in the dark region of Fig. 4.14, while photons with energy higher than 100 eV (SXR) reach the maximum amount a little later than the end of reconnection. This measured result indicates that some electrons would be accelerated by magnetic reconnection, and EUV light is emitted from

these energetic electrons. Because of further acceleration, a part of these electrons obtain higher kinetic energy, resulting in the decrease of EUV light intensity and increase of SXR intensity.

The Fig. 4.14 also indicates that the intensity of the signal from the Al-filter MCP chamber is relatively stronger than the Mylar-filter one. This result means that the energy of SXR emitted from the plasma during magnetic reconnection is just a little higher than 100 eV, and the energy of the signal from the Al-filter MCP chamber is mainly in the range between 20 and 100 eV, belonging to EUV, as shown in the dark circle in the Fig. 4.11. Owing to the use of different filters, the energy range of SXR on TS-6 is successfully determined to be higher than 100 eV but lower than 400 eV.

4.3 Tomography

Computed tomography (CT), as an effective reconstruction method, was first applied in the field of medical imaging diagnostics. With the rapid development of this technique, it has been spread to many more other fields, such as nondestructive materials testing, geophysics, atmospheric research, and plasma diagnostics[59]. The main purpose of tomography is to mathematically process many non-local measured data, such as line-integrated images, to reproduce local physical quantities, such as emissivity.

For a high-temperature plasma device, tomography is usually applied to reconstruct images for imaging diagnostics, such as bolometer, soft/hard X-ray, visible light, vacuum/extreme-ultraviolet light. As mentioned in the Abstract, we use tomography method based on Phillips-Tikhonov regularization to reconstruct the line-integrated images, in order to obtain local emissivity of soft X-ray (SXR), which reflects the distribution of high-energy electrons generated during magnetic reconnection on TS-6 merging spherical tokamak (ST) experiments.

In this section, the tomography method is in detail introduced, including the principle and algorithm. The Radon transform and its inverse-transform are the mathematical bases of tomography, which describe the relationship between line-integral and local emissivity. Solving such an inversion problem is usually regarded to be ill-posed. There are some mathematical method to deal with ill-posed problems, such as Cormack method, maximum entropy method, algebraic reconstruction technique, and Phillips-Tikhonov regularization.

We employ the Phillips-Tikhonov regularization to optimum the solution, and minimize the instability and non-uniqueness caused by this inverse problem. Besides, the effectiveness and accuracy of this reconstruction method is also quantitatively evaluated by phantom/assumed image test.

4.3.1 Introduction to Tomography

In 1885, Wilhelm Conrad Rontgen, a German scientist, discovered that the X-ray was emitted from cathode-ray tube (CRT) on his experiments for the first time. Since then, X-ray attracted a lot of research interests, and was rapidly developed. This kind of radiation has a strong ability to penetrate human body, and can be recorded by photographic films. This characteristic of X-ray gave birth to the X-ray photography technology, which is able to be applied for detection and diagnostics, especially for medical diagnostics. However, the image obtained by X-ray photography is two-dimensional and cannot fully reflect the information of three-dimensional objects. Especially in the depth direction, the information is highly overlapped and is hard to be clearly recognized. Besides, the contrast of images is also reduced. Therefore, with the development of mathematics and physics, reconstruction technology that inverts the cross-sectional information based on projection images of the object from different angles has emerged, that is, tomographic reconstruction.

During 1820s, Norwegian mathematician Niels Henrik Abel proposed a theory, which was named as Abel's integral equation later, to solve a mechanical problem. The purpose of Abel's integral equation is to find how long it will take a bead to slide down a wire or to find the shape of the curve into which the wire is bent. This theory has been widely used in many fields such as mechanics, spectroscopy, seismology, plasma physics.

In 1917, Austrian mathematician Johann Karl August Radon developed and proposed a two-dimensional image reconstruction theory based on Abel's idea. Radon's theory is the mathematical basis of tomographic reconstruction technology: Radon transform. The Radon transform mathematically proves that the two-dimensional distribution function of a physical parameter can be determined by all the line integrals of this function in its domain. For image reconstruction of various radiation including X-ray, this physical parameter refers to the emissivity of radiation, and the line integral is the measured value/image obtained by the radiometric/imaging system. According to Radon's theory, the emissivity The two-dimensional spatial distribution can be determined by the experimental data of the measurement/imaging system.

The tomographic reconstruction algorithms can be mainly classified into two categories: iterative reconstruction algorithms and analytical reconstruction algorithms, as shown on the Fig. 4.15

(1) The iterative reconstruction algorithm takes solving equations as the main idea. Linear algebraic equations are constructed based on measured experimental data at first, and then the purpose of image reconstruction can be achieved by solving the equations. Iterative reconstruction algorithms can be divided into algebraic iterative reconstruction algorithms and statistical iterative reconstruction algorithms. The basis of statistical iterative reconstruction algorithms is optimization theory. The image reconstruction problem can be regarded as a parameter estimation problem. By selecting or constructing a reasonable objective function, solving/finding the parameter that makes the objective function reach the maximum value under some certain constraints. The main algorithms include the maximum entropy method, the minimum norm method, and Phillips-Tikhonov regularization.

(2) Analytical reconstruction algorithms can be further divided into two-dimensional image reconstruction and three-dimensional image reconstruction, according to different scanning forms. The two-dimensional image reconstruction algorithm is based on the Fourier central slice theorem, and mainly includes the direct Fourier reconstruction algorithm and the filtered back projection algorithm. The filtered back projection algorithm is widely used in medical image reconstruction. Three-dimensional image reconstruction algorithms can be divided into approximate image reconstruction algorithms and precise image reconstruction algorithms. The iterative reconstruction algorithm has the advantages of strong anti-noise and low requirements on the completeness of the data. However, at the same time, the disadvantages such as large amount of calculation and slow reconstruction speed also have a negative impact in practical applications. In contrast, analytical reconstruction algorithms have fast reconstruction speed, but have poor anti-noise performance and high data integrity requirements, and are widely used in the field of medical diagnostics.

In the research field of fusion plasma, due to the limitation of experimental conditions, the number of detectors is not enough and the measurement angle is also limited, which results in that the experimental data obtained is usually not complete, and the noise can not be ignored.

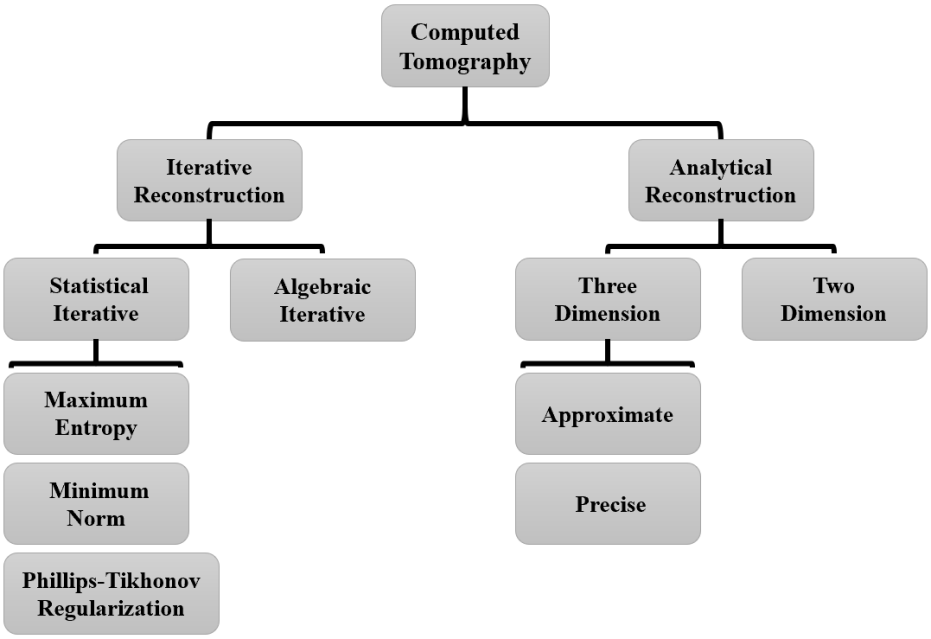

Fig. 4.15 Classification of major tomographic reconstruction algorithms

So, iterative reconstruction algorithm has been widely used in fusion research. Especially with the upgrading of computer technology, the application of iterative reconstruction algorithms including maximum entropy method and Phillips-Tikhonov regularization in fusion research has also received more and more attention.

4.3.2 Tomography for Plasma Diagnostics

For a fusion plasma, the experimental data measured by some diagnostic systems are line-integral, such as bolometer, soft/hard X-ray, visible light, vacuum ultraviolet light (VUV), neutron. Obtaining the plasma emissivity through the inversion of the line-integral measured values has always become an important task in the data processing of the plasma experiment. When the emissivity is fixed on the same magnetic surface, one-dimensional inversion is sufficient to deal with such problems. However, in the case of polar asymmetry, such as MHD (Magneto-hydro-dynamic) phenomenon, impurity transport, fast trapping particles and other situations, in order to obtain the emissivity on the polar cross-section, the two-dimensional inversion is necessary.

The tomographic reconstruction is based on the Radon transformation, which can be used in the study of plasma diagnostic to reconstruct the spatial distribution of radiation emissivity on a two-dimensional polar cross-section. The intensity of plasma radiation is determined by factors such as plasma density, temperature, and finite number of charges. Therefore, according to the reconstructed plasma emissivity, information such as impurity transport, MHD instability, and plasma location can be obtained. Plasma radiation in the wavelength range of vacuum ultraviolet light, visible light and infrared light usually occurs at the plasma boundary position, and the structural information on the plasma boundary can be obtained based on the spectrum in these ranges.

In many fusion devices, such as JET, TCV, AUG, LHD, EAST, KSTAR, tomography of soft X-ray has already become a basic reconstruction technology, which is widely used to study various instability problems in plasma, such as saw-tooth, magnetic island structure, etc. In addition, in the plasma core, since the plasma balance reconstruction in this region is highly uncertain, independent plasma profile information is very valuable. Besides, X-ray is mainly generated from the plasma core, which shows the importance of X-ray diagnosis. The key to these problems is how to reconstruct the spatial distribution of the X-ray emissivity on the poloidal cross-section through the line-integrated value measured by the diagnostic system.

4.3.3 Algorithm of Tomography

Ill-posed Problem

The well-posed problem refers to a type of mathematical issue whose solution exists, is stable, unique and continuously dependents on the input data, and vice versa. For the reconstruction problem mentioned in the previous section, the inverse solution of the spatial distribution of particles by the measured line-integral images is an inverse solution to some structural features in the system from the partially known information of the output results. It is obviously an inverse problem in mathematics, and the vast majority of inverse problems are ill-posed.

The tangential-view tomographic reconstruction problem is limited by objective conditions:

- (1) There are unavoidable errors in the measured experimental data as well as noise;
- (2) The experimental data are often under-determined or over-determined when used as input data in the solution of mathematical problems, which can lead to solutions that may not be unique, stable or even non-existent;
- (3) Inverse problems in which the solution is often not continuously dependent on the input data (experimental data).

Therefore, the reconstruction problem here is an ill-posed problem, and the reconstruction results obtained from it are unstable and not unique. This problem cannot be solved directly by inverse equations. The instability of the reconstruction problem is further aggravated by the fact that in practice the measurement points (i.e. the detector locations) are discrete.

When using classical methods for ill-posed problems, the known information does not necessarily guarantee the existence or uniqueness of the solution, and in addition, small changes in the known information can have a serious impact on the solution. So, the results obtained using classical methods become meaningless and unreliable. The reconstruction problem in this thesis, as discussed above, has been shown to be unsuitable. So, in order to solve this problem, it needs to be regularized to obtain an optimal approximate solution, involving mainly the singular value decomposition method, and the Phillips-Tikhonov regularization method.

Singular value decomposition

The singular value decomposition is an important matrix decomposition in linear algebra, which is mainly used in fusion plasma physics for: computing the inverse of matrices in uncomfortable qualitative problems; decomposing experimental data into different parts according to temporal or spatial properties, which in turn can be studied separately for the desired part, or used to filter noise.

For an arbitrary matrix X of order $M \times N$, this can be decomposed into

$$X_{M\times N} = U_{M\times M}\Sigma_{M\times N}V^T_{N\times N}. \tag{4.1}$$

where the matrices U and V are both You matrices, and the matrices U^T and V^T are conjugate matrices of the matrices U and V respectively, and satisfy

$$U_{M\times M}U^T_{M\times M} = I_{m\times m}\ , \qquad V_{N\times N}V^T_{N\times N} = I_{N\times N}. \tag{4.2}$$

The matrix Σ is a diagonal matrix of order $M \times N$ whose non-zero diagonal elements are the singular values of the matrix X and are arranged in descending order, i.e. $\sigma_{11} \geq \sigma_{22} \geq \cdots \geq 0$.

Since the matrix X is often of unsatisfied rank, there is no inverse matrix of it, and its generalized inverse matrix (X^+) can be found according to the above definition:

$$X^+_{N\times M} = V_{N\times N}\Sigma^+_{N\times M}U^T_{M\times M}. \tag{4.3}$$

where the matrix Σ^+ is a diagonal matrix of order $N \times M$ and satisfies $\sigma_{ii} \cdot \sigma^+_{ii} = 1$.

The geometric matrix is often of insufficient rank, and when the discomfort problem is not very serious, the generalized inverse matrix can be solved according to the procedure described above to invert the equation to obtain the distribution of the emissivity E. However, for practical experimental results, which are severe discomfort problems for the reasons described above, the accuracy of the solution results needs to be further improved, and so the truncated singular value decomposition method, equivalent to the Phillips-Tikhonov regularisation method for discrete discomfort problems, is required.

For the imaging system, the obtained raw images are line integrals of local emissivity of SXR along each line of sight. Tomography method based on the Phillips-Tikhonov regularization is employed in order to obtain local emissivity of SXR, which reflects the spatial distribution of high-energy electrons.

The line-integral relationship between the images and the local emissivity can be expressed as:

$$\boldsymbol{P} = G\boldsymbol{E} + \boldsymbol{\varepsilon}, \tag{4.4}$$

where vector $\boldsymbol{P}$ represents measured values of the imaging system, $\boldsymbol{E}$ represents local emissivity of SXR emitted from plasma, $\boldsymbol{\varepsilon}$ is a residual vector, and matrix G represents the geometric relationship between lines of sight and observed plasma.

For a tokamak plasma, SXR emissivity can be assumed to be symmetric in toroidal direction. Based on this assumption, lines of sight can be projected onto just one cross-section, as shown in the Fig. 4.16. Therefore, the relationship between lines of sight and observed plasma in this tangential-view system can be simplified to be a 2-D plane problem. The colorful curved lines represents projected lines of sight, and the blue solid circles represent the cross-section of two merging ST plasmas. The projection plane can be divided into computational grids, and then the geometric matrix G is calculated in advance by accounting the length of each line of sight inside each node of grids, which represents the corresponding weight of each emission cell to each detector/pixel.

In this diagnostic, we reduce the resolution of images from 230×230 to 100×100 and set the computational grid of 100×100 for the tomographic reconstruction, considering the balance between spatial resolution and computational efficiency. Under this condition, the spatial resolution can be up to 4 mm.

Due to instability and non-uniqueness of solving inverse problem, obtaining local emissivity directly based on Eq. (4.4) or the ordinary least squares linear regression is highly ill-posed. Phillips-Tikhonov regularization is used in this paper to optimize the solution, namely to minimize the residual term $\boldsymbol{\varepsilon} = \boldsymbol{P} - G\boldsymbol{E}$. The above problem can be transformed to solve $\boldsymbol{E}$ when the following quantity χ^2 takes the minimum value,

$$\chi^2 = \alpha \|L\boldsymbol{E}\|^2 + \|\boldsymbol{P} - G\boldsymbol{E}\|^2, \tag{4.5}$$

where $L = \nabla^2$ is the Laplacian matrix, and α is the regularization factor, which can determine the optimum degree of solution. In general, the regularization factor α is selected by some

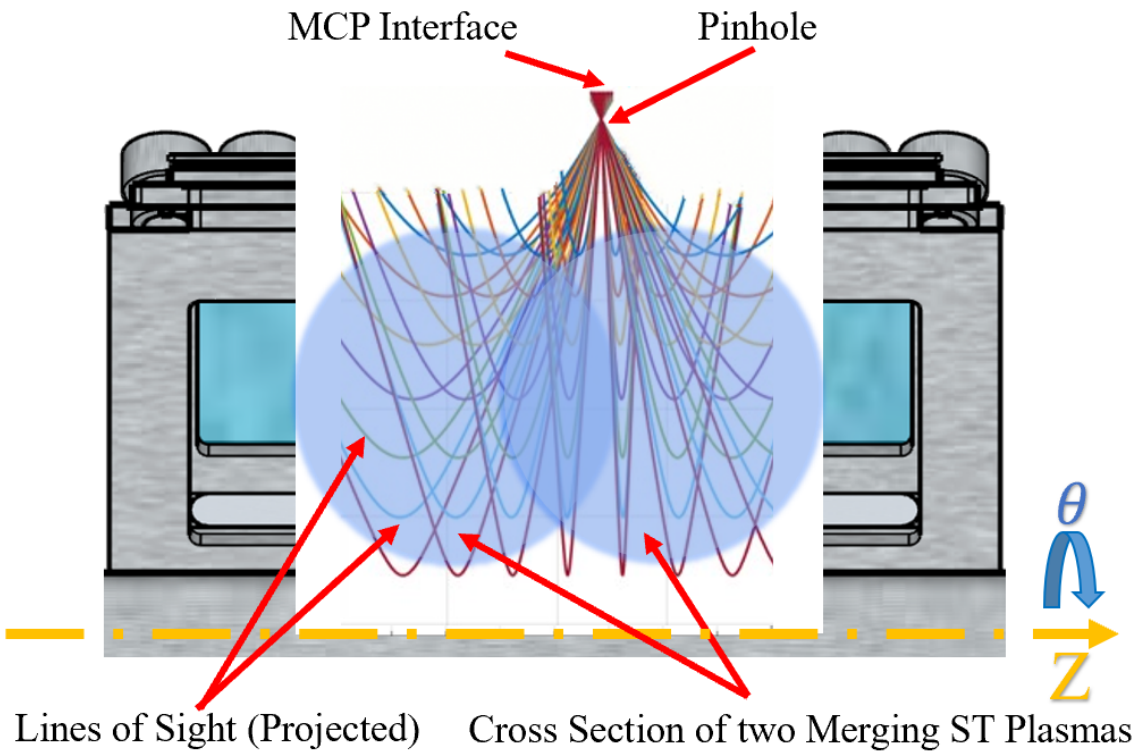

Fig. 4.16 Schematic diagram of line of sight on TS-6 with cross-section of two merging ST plasmas.The colorful curved lines represent projected lines of sight.

methods such as generalized cross validation (GCV) and L-curve, of which appropriate choice would be more effective for specific cases[60]. For this diagnostic, both methods can be applicable and no obvious superiority is found. We employ the GCV method, as expressed in the following:

$$GCV(\alpha) = \frac{\|\boldsymbol{P} - G\boldsymbol{E}(\alpha)\|^2}{[Trace[I - GG(\alpha)]]^2}, \tag{4.6}$$

where $G(\alpha) = (G^T G + \alpha L^T L)^{-1} G^T$, and $\boldsymbol{E}(\alpha)$ can be obtained from the following regularized normal equation:

$$(G^T G + \alpha L^T L)\boldsymbol{E}(\alpha) = G^T \boldsymbol{P}. \tag{4.7}$$

4.3.4 Validation of Effectiveness and Accuracy

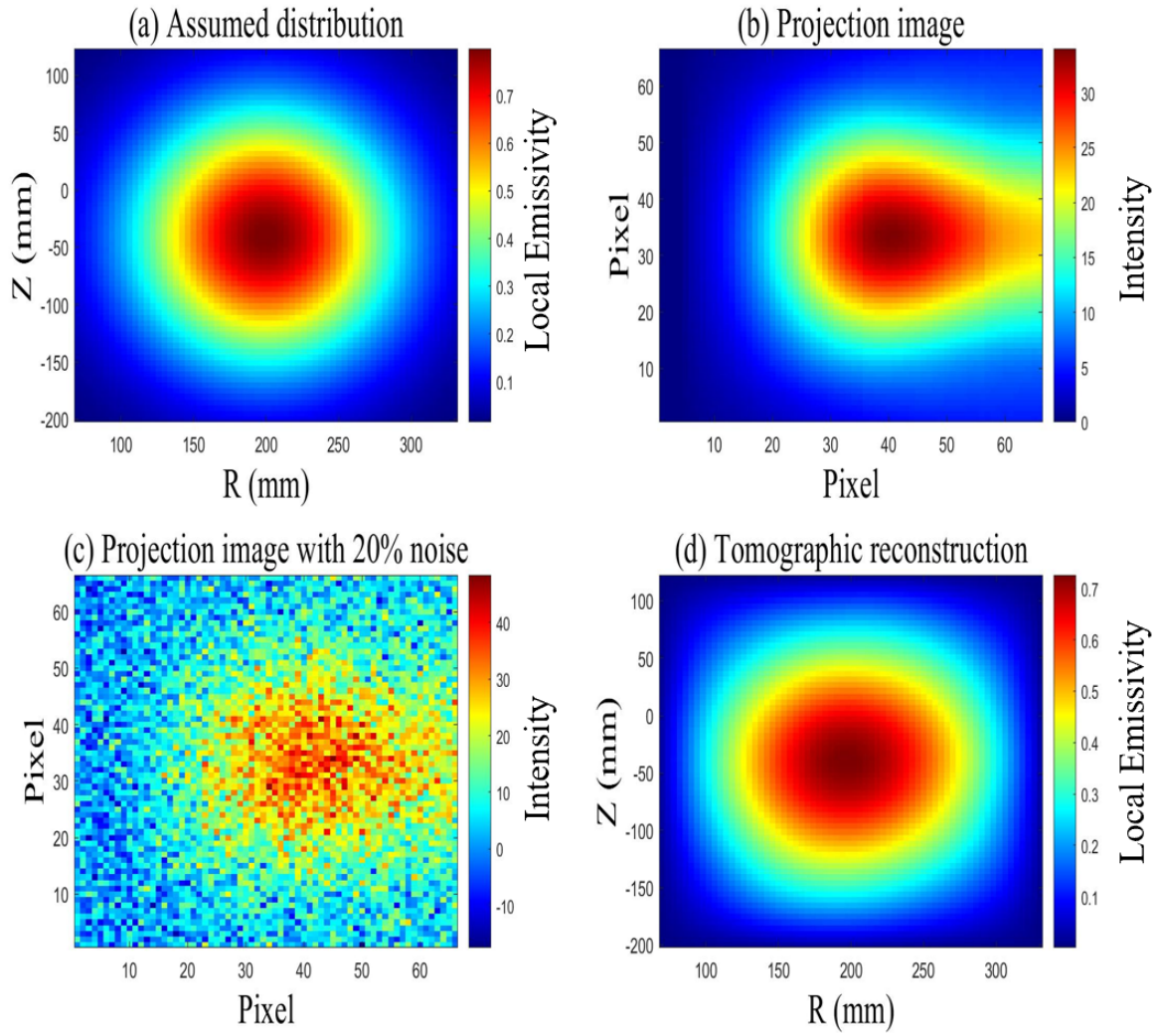

Fig. 4.17 Phantom image test for validation by using an assumed peak distribution. (a) Assumed distribution. (b) Projection image of the assumed distribution. (c) Image of the projection with 20% Gaussian noise. (d) Tomographic reconstruction result.

To verify the effectiveness and accuracy of the Phillips-Tikhonov regularization method in solving the tangential reconstruction problem, an assumed distribution serving as the original object is employed to test if it can be reproduced by this tomographic method, as

shown in the Fig. 4.17.(a). This distribution can be expressed as:

$$E = \frac{1}{\sqrt{2\pi}\sigma} \cdot e^{-\frac{(\rho-\mu)^2}{2\sigma^2}}, \tag{4.8}$$

where the $\sigma = 0.5$ and the $\mu = 0$.

The Fig. 4.17.(b) is the projection image of the assumed distribution. The projection image is line-integrated and calculated by the original distribution and geometric matrix. The projection represents the measured image for a imaging system. As there is always inevitable noise for the measured images, a certain amount of Gaussian noise is added to the projection image. The Fig. 4.17.(c) shows the image of the projection with 20% Gaussian noise, which becomes blurry and unclear. The Fig. 4.17.(d) is the reconstructed result by Phillips-Tikhonov regularization method. By comparing Fig. 4.17.(d) and Fig. 4.17.(a), we can see that the Phillips-Tikhonov regularization method is able to reconstruct the original assumed distribution very well, even when there is strong noise. The reliability of the method in solving the ill-posed problem is also verified by the effective reconstruction. Therefore, it has been demonstrated that the tomographic reconstruction method can be applied to the image inversion problem of the tangential imaging diagnostic system on the TS-6 device.

Because the SXR diagnostic is developed on TS-6 device for the first time, the structure of images which would be measured is unpredictable. So, another two common kinds of assumed profiles are employed to further validate the effectiveness and accuracy of this tomographic method. This validation processes are similar to the above ones. The Fig. 4.18 shows the phantom image test by using an assumed hollow distribution for validation, where the $\sigma = 0.05$ and the $\mu = 0.7$. The Fig. 4.19 shows the phantom image test by using an assumed high-mode distribution for validation. This distribution can be expressed as:

$$E = \frac{1}{\sqrt{2\pi}\sigma} \cdot e^{-\frac{(\rho-\mu)^2}{2\sigma^2}} \cdot con(m\theta), \tag{4.9}$$

where the $\sigma = 0.1$, the $\mu = 0.85$ and the $m = 20$. The high-mode structure is usually observed in instability problem.

Phantom image tests by using these three kinds of assumed distributions (peak, hollow, and high-mode) show that the reconstructed profiles can well reproduce the original information. So, this kind of tomographic method is able to be employed to reconstruct general line-integrated images in TS-6 merging experiments.

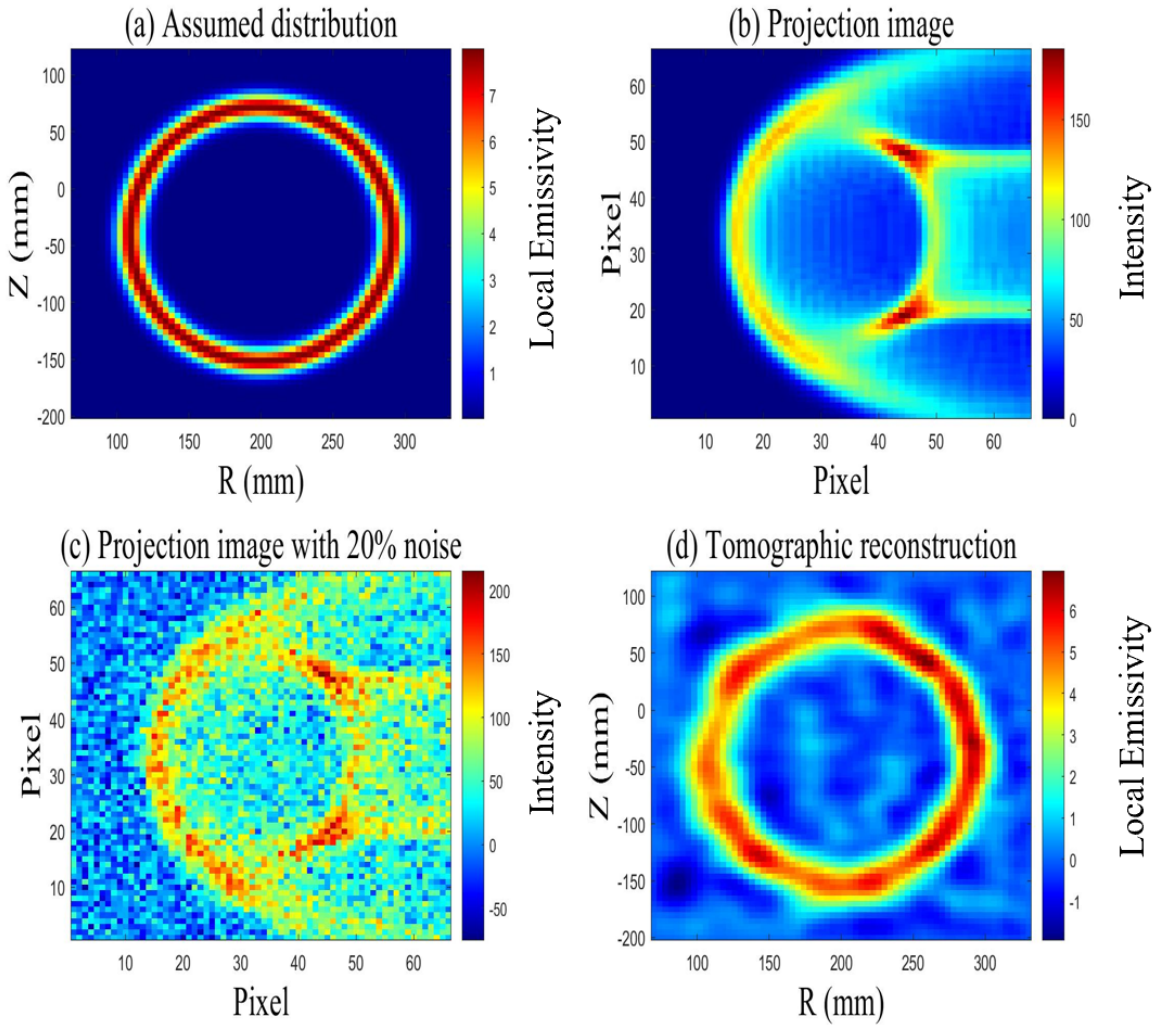

Fig. 4.18 Phantom image test for validation by using an assumed hollow distribution. (a) Assumed distribution. (b) Projection image of the assumed distribution. (c) Image of the projection with 20% Gaussian noise. (d) Tomographic reconstruction result.

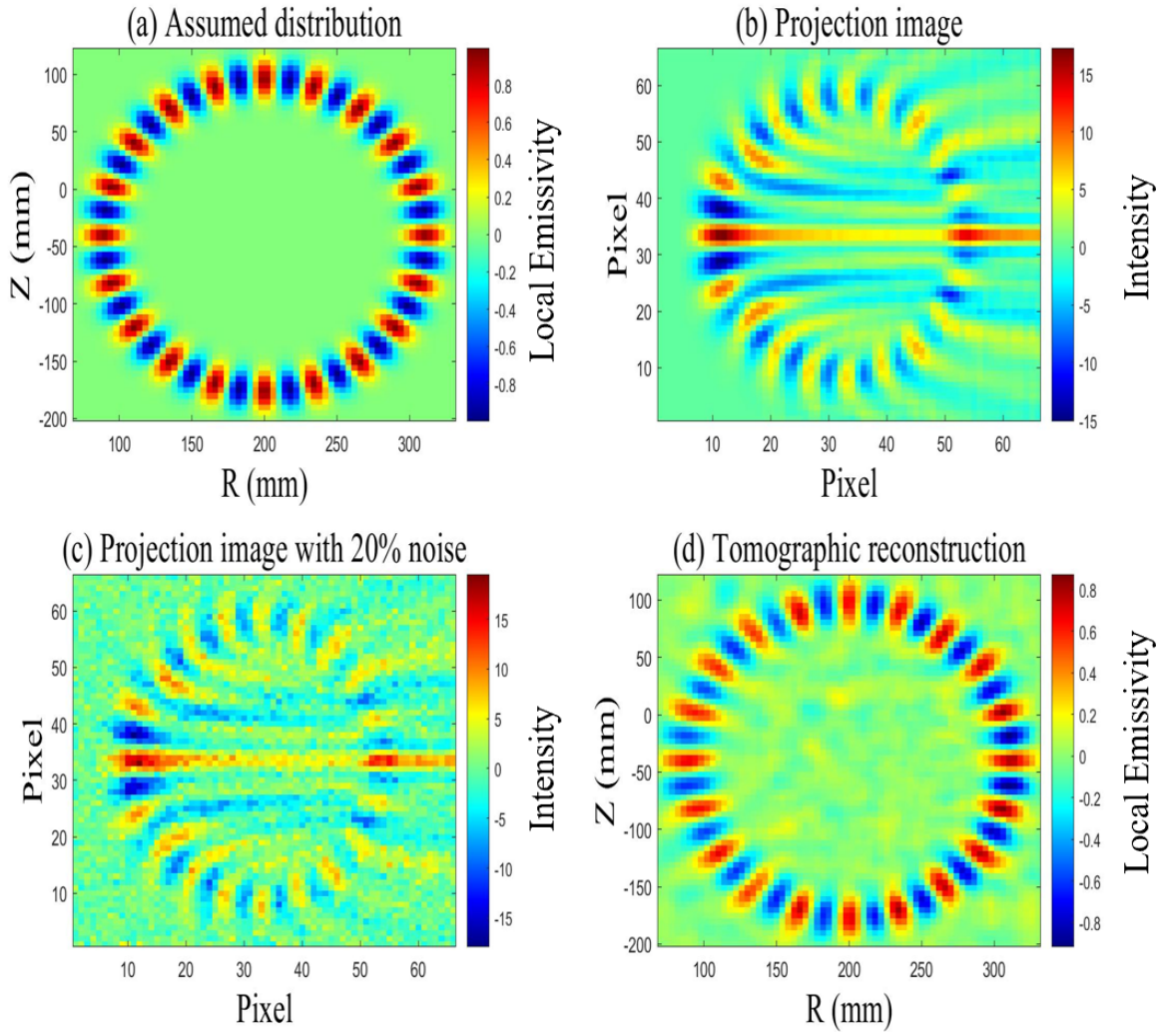

Fig. 4.19 Phantom image test for validation by using an assumed high-mode distribution. (a) Assumed distribution. (b) Projection image of the assumed distribution. (c) Image of the projection with 20% Gaussian noise. (d) Tomographic reconstruction result.

Chapter 5

Electron Acceleration in Magnetic Reconnection

5.1 Review of Electron Acceleration Mechanism

The mechanism of electron acceleration is kept to be concerned, as it is important and indispensable to reveal the physics of magnetic reconnection. Cluster observations and particle-in-cell (PIC) simulations have been trying to figure out this problem, and there are some possible explanations to make it clear.

In the anti-parallel magnetic reconnection, the meandering motion of electrons near the X-point is considered to be the main mechanism of electron acceleration[61]. The Fig. 5.1 shows the process of electron acceleration during the evolution of anti-parallel magnetic reconnection. Electrons in inflow are to be accelerated by the reconnection electric field near the X-point.

If a guide field is employed in addition, electrons would be accelerated in advance by parallel electric field along the separatrix. When these electrons enter into the region near the X-point, they would do gyratory movement around the guide field, which confines them in the vicinity of X-point and further accelerate them[62].

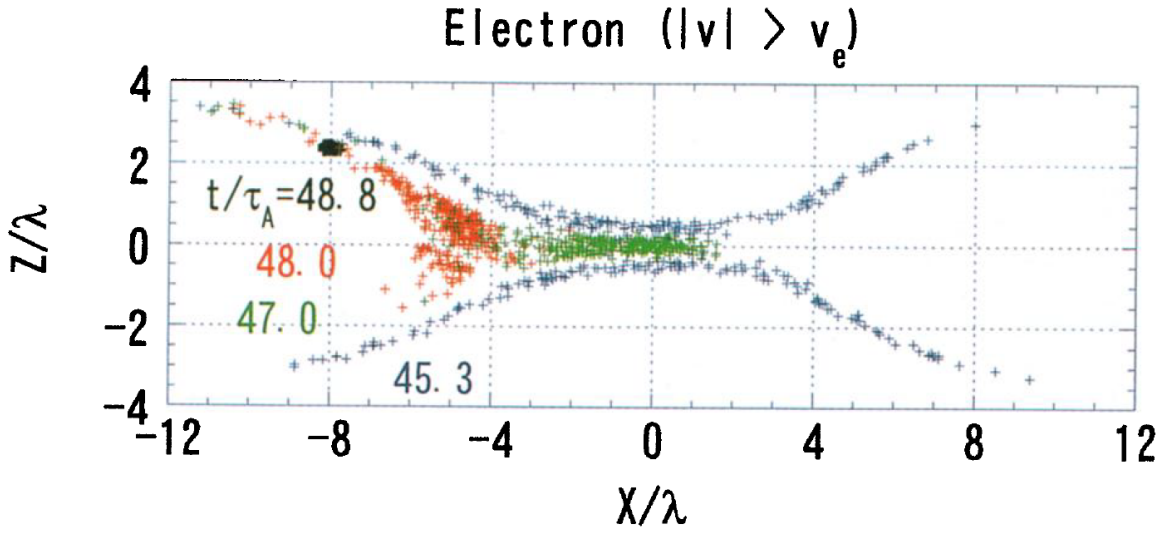

Fig. 5.1 Positions of electrons traced backward in time from the black area at $t/\tau_A = 48.8$.[61]

For the downstream region, electrons can be accelerated in the magnetic field pileup region, as the electric field can accelerate electrons in their drift direction (gradient drift and curving drift of magnetic field).[61]

The movement of electrons would be coupled with magnetic field again after they leave from the electron diffusion region. When the electrons arrive the region where the magnetic field is relatively high, the kinetic energy of electrons in the direction perpendicular to magnetic field would increase. The betatron acceleration mechanism plays an important role in accelerating electrons in the magnetic field pileup region. If there is a parallel electric field in the magnetic field pileup region, electrons would be confined here, and the betatron acceleration would last longer[63].

According to the description above, the electron acceleration during magnetic reconnection is not a simple acceleration process near the X-point, but a process of multiple steps. Prof. Hoshino divided the acceleration process into 3 steps[61, 64, 65]:

- (1) preliminary acceleration before the electrons enter into the region near the X-point, which is also known as surfing acceleration;
- (2) acceleration near the X-point, which can be enhanced by guide fields;

- (3) acceleration in the downstream region where the magnetic field piled up and betatron acceleration plays an important role.

Betatron and Fermi acceleration were found to contribute to electron acceleration in the downstream regions during unsteady magnetic reconnection by cluster observation[66]. Among them, the localized betatron acceleration plays an important role in the downstream acceleration and is responsible for more than half of the energy gain for the peak observed fluxes. The acceleration mechanism is quasi-adiabatic, and the highest electron fluxes distribute in the direction perpendicular to the magnetic field in the rising speed portion of the jets.

5.2 Electron Acceleration in the Downstream Region

There have already been some efforts that attempt to understand the mechanism of electron acceleration in the downstream region, especially near the dipolarization front (DF), by PIC simulation. At first, some PIC simulation results are to be introduced, which can help to easier understand the physical image and mechanism of electron acceleration in the downstream region. On the other hand, it can also serve as a reference for the experimental results.

Fig. 5.2 shows the positions of high-energy electrons accelerated in the pileup regions, which is calculated by tracing the energetic electrons. The colors of the figure on the right side denote the mean kinetic energies of these electrons at different times[63]. This method can directly explain the formation of electron energy fluxes. Electrons are accelerated in the pileup regions and obtain much more energy with the process of acceleration. At the meanwhile, these accelerated electrons would move to further downstream regions.

The Fig. 5.3 shows the trajectories of some typical electrons at different timings. The figures on the left side show the trajectories of electron which is not sufficiently accelerated near the in the DF region. This kind of electron has a large velocity parallel to the magnetic lines, so it will pass through the DF region in a short time without sufficient acceleration.The figures on the right side show the trajectories of electron which has very small parallel velocity. Therefore, it will be trapped in DF region and obtain huge acceleration here by the induced electric field. The electric field is induced because of the increase of B_z. The movement direction is perpendicular to the magnetic field, which agrees with with the cluster observation as mentioned above[66]. The betatron acceleration plays an important role during this electron acceleration process.

The trajectories of some typical electrons can explain the mechanism of electron acceleration more detailed, and the formation of electron energy fluxes also becomes easier to be understood.

As mentioned before, the SXR tomographic diagnostic is developed to reveal the local emissivity of SXR, which reflects the distribution of accelerated electrons in TS-6 plasma

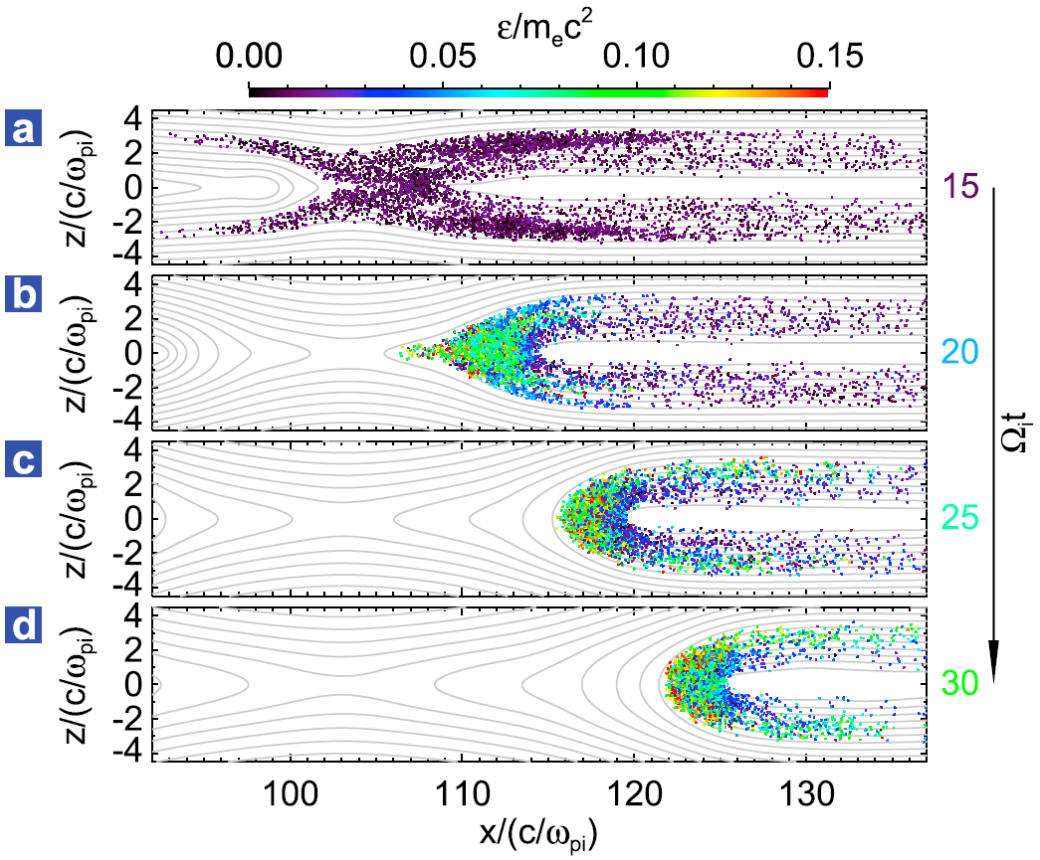

Fig. 5.2 The position of the electrons accelerated near the pileup region at (a) $\Omega_i t = 15$, (b) $\Omega_i t = 20$, (c) $\Omega_i t = 25$, and (d) $\Omega_i t = 30$. The colors of the dots present the kinetic energy for each electron, and the colors of the figures on the right side denote the mean kinetic energies of these electrons at different times. The silver contours represent the in-plane magnetic field lines. [63]

merging experiments. Reconstructed results of SXR intensity are shown in the Fig. 5.4. The white curved lines represent magnetic filed lines. SXR can be evidently observed at $t = 470$ μs, while the SXR signal is very weak at $t = 460$ μs.

For this experiment, we chose Argon as the discharge gas, as it is much easier to be ionized, compared with Hydrogen. In our test experiments, we tried to use the Hydrogen as the discharge gas, but the measured SXR signal is very weak, due to the low electron bulk temperature in the present TS-6 plasma.The exposure time of high-speed framing camera is usually chosen to be 5 μs or 2 μs. The charging voltages for toroidal and poloidal field coils

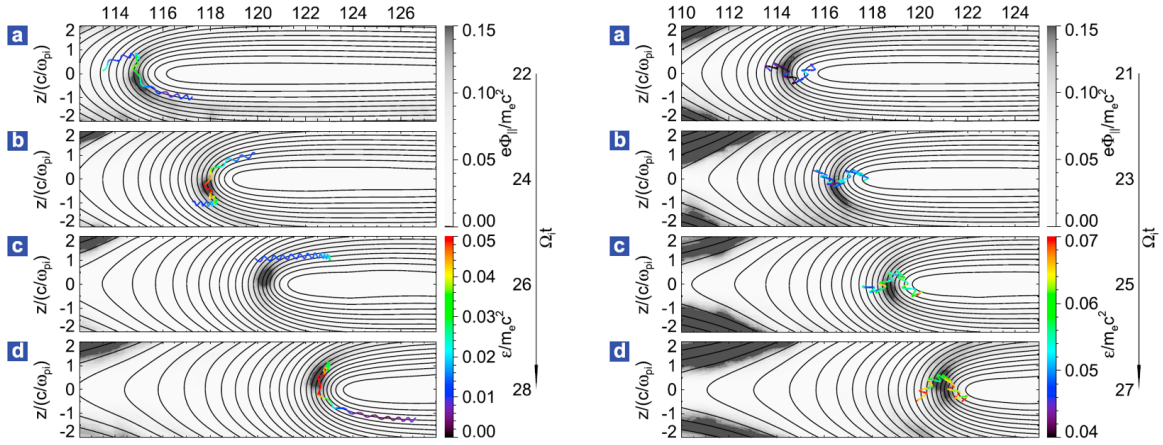

Fig. 5.3 The trajectories of the most accelerated electron during (a) $20.1 \leq \Omega_i t \leq 22$, (b) $22 \leq \Omega_i t \leq 24$, (c) $24 \leq \Omega_i t \leq 26$, (d) $26 \leq \Omega_i t \leq 27.8$. The colors of the trajectory indicate the kinetic energies, while the background images are the parallel electric potential. [63]

are generally chosen to be as high as possible, in order to make sure that the SXR signal is strong enough.

On the other hand, the reconstructed SXR emissivity also indicates that electrons can be accelerated in the downstream regions, both in the inboard-side and outboard-side. The SXR emissivity is much stronger in the inboard-side, which means that electrons are more likely to be accelerated to higher energy in this side where the toroidal magnetic field is much higher. This experimental result first indicated the downstream acceleration in TS-6 merging experiments. In the follow-up experiments, related issues are investigated in depth.

As shown in the Fig. 5.5, the left-column figures show local emissivity with energy range more than 100 eV, while the right-column ones show local emissivity with energy range from 20 eV to 100 eV. The local emissivity reflects the distribution of high-energy electrons, and the majority of them are found distributing in the direction perpendicular to the magnetic field, which agrees with PIC simulation[63, 67]. Accelerated electrons with different energy range can be found in the downstream regions during the magnetic reconnection. Only accelerated electrons with lower energy (20 eV $\sim$ 100 eV) can be obviously measured in relatively earlier stage at $t = 475$ μs. With the evolution of magnetic reconnection, electrons with higher energy ($>$ 100 eV) are found distributing in further part of downstream region as

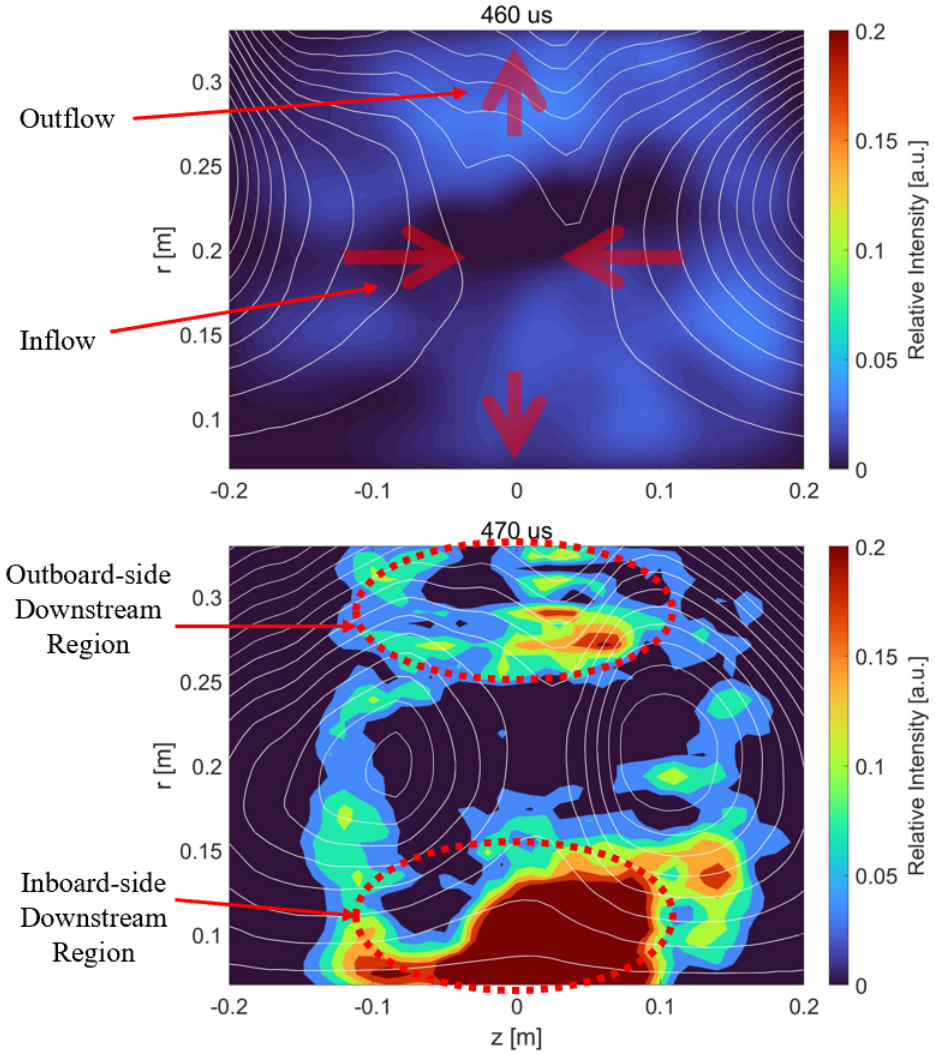

Fig. 5.4 Reconstructed results of SXR images measured by 1.0 μm Mylar-filter pinhole camera at $t = 460\mu$s and $t = 470\mu$s respectively. The white curved lines represent magnetic field lines of two merging ST plasmas.

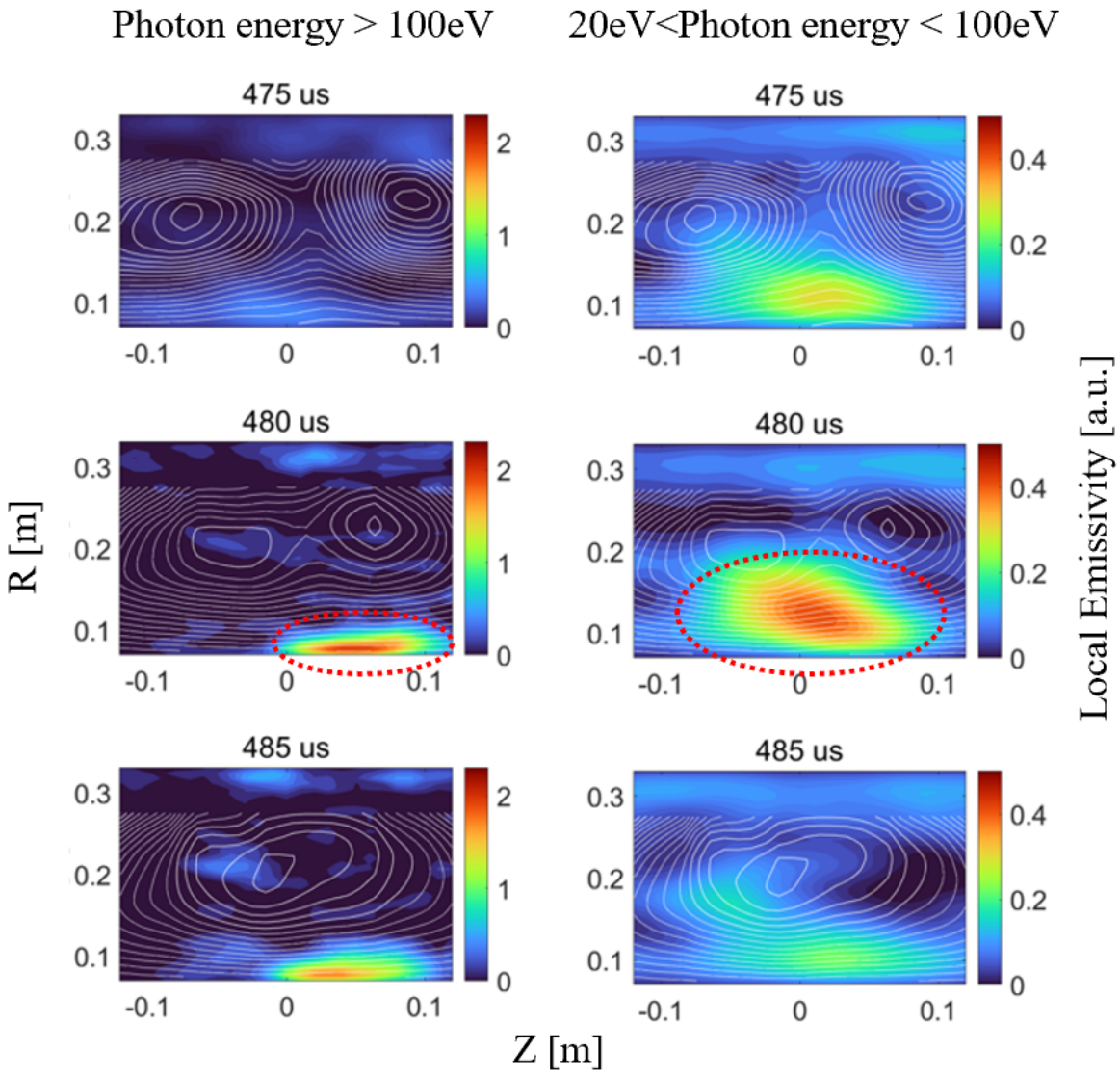

Fig. 5.5 Local emissivity of accelerated electrons with different energy ranges during the evolution of magnetic reconnection in TS-6 plasma merging experiments. The figures in left column show local emissivity with energy range more than 100 eV, while the right-column ones show local emissivity with energy range from 20 eV to 100 eV. The white curved lines represent magnetic field lines of two merging ST plasmas.

shown in the red dotted circle on the left side at $t = 480$ μs, compared with electrons with lower energy on the right side. After the magnetic reconnection, the energy of electrons decays at $t = 485$ μs.

After acceleration in the X-point region, electrons leave from electron diffusion region along with the outflow and most of them would be trapped by the electric potential. These electrons can be accelerated by the induced electric field in the magnetic pileup areas, and obtain much more energy along with the movement to further parts of the downstream region, which can explain the above experimental results as shown in the Fig. 5.5. The localized beratron acceleration plays an important role for the electron acceleration in the downstream region.

5.3 Effects of B_z on Electron Acceleration

Poloidal field (PF) coils are employed to induce two ST plasmas in TS-6 merging experiments. Higher swinging down of PF voltage can produce plasma with higher plasma current, which increases the B_z in the following process. Plasma merging experiments were carried out on TS-6 device with different charging voltages for PF coils to investigate the effects of B_z on electron acceleration. The voltage of toroidal field (TF) was kept in the same value (4 KV) in order to control variable. The discharge gas is argon (Ar).

The Fig. 5.6 shows the detailed reconstructed results with different PF charging voltages from 30 KV to 39 KV at different times. The corresponding B_z can be found in the Fig. 5.7. The peak value of reconstructed local emissivity is employed to quantitatively compare the relative intensity of SXR emission.

The reconstructed local emissivity reflects the distribution of accelerated electrons. The peak value of local emissivity in X-point and downstream region of the Fig. 5.6 with different charging PF voltage/B_z at $t = 480\mu$s is shown in the Fig. 5.7. It can help to quantitatively compare the effects of B_z on electron acceleration. Thus, electron acceleration in the downstream region is obviously enhanced along with the increase of PF voltage, while near the X-point the electron acceleration is not obviously enhanced. The reason is that the increase of PF makes the B_z stronger, which enhances the electron acceleration in the downstream region. But, the electron acceleration in the X-point region is mainly dominated by guide field, and it will be discussed in the next subsection.

As introduced before, electron can be accelerated in the downstream region where the magnetic field piles up, as the electric field can accelerate electrons in their drift direction (gradient drift and curving drift of magnetic field)[61]. The increase of PF enhances the above effect by increasing the induced electric field, which lead to the increase of downstream acceleration. This phenomenon also indicates that the betatron acceleration is an important mechanism for explaining the generation of high-energy electrons in the downstream regions during the magnetic reconnection.

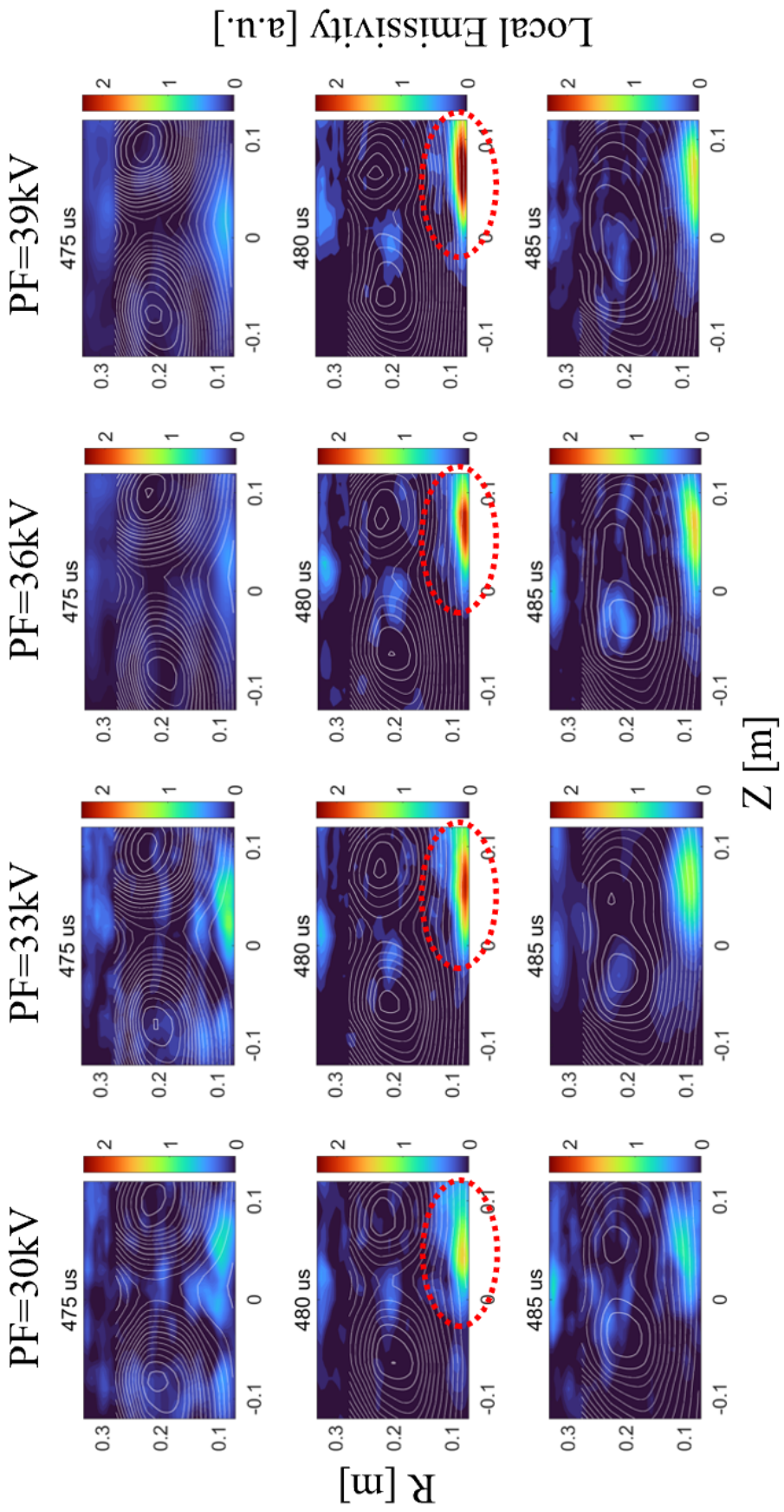

Fig. 5.6 Reconstructed results of SXR images measured by 1.0 μm Mylar-filter pinhole camera with different PF voltage. The white curved lines represent magnetic field lines of two merging ST plasmas.

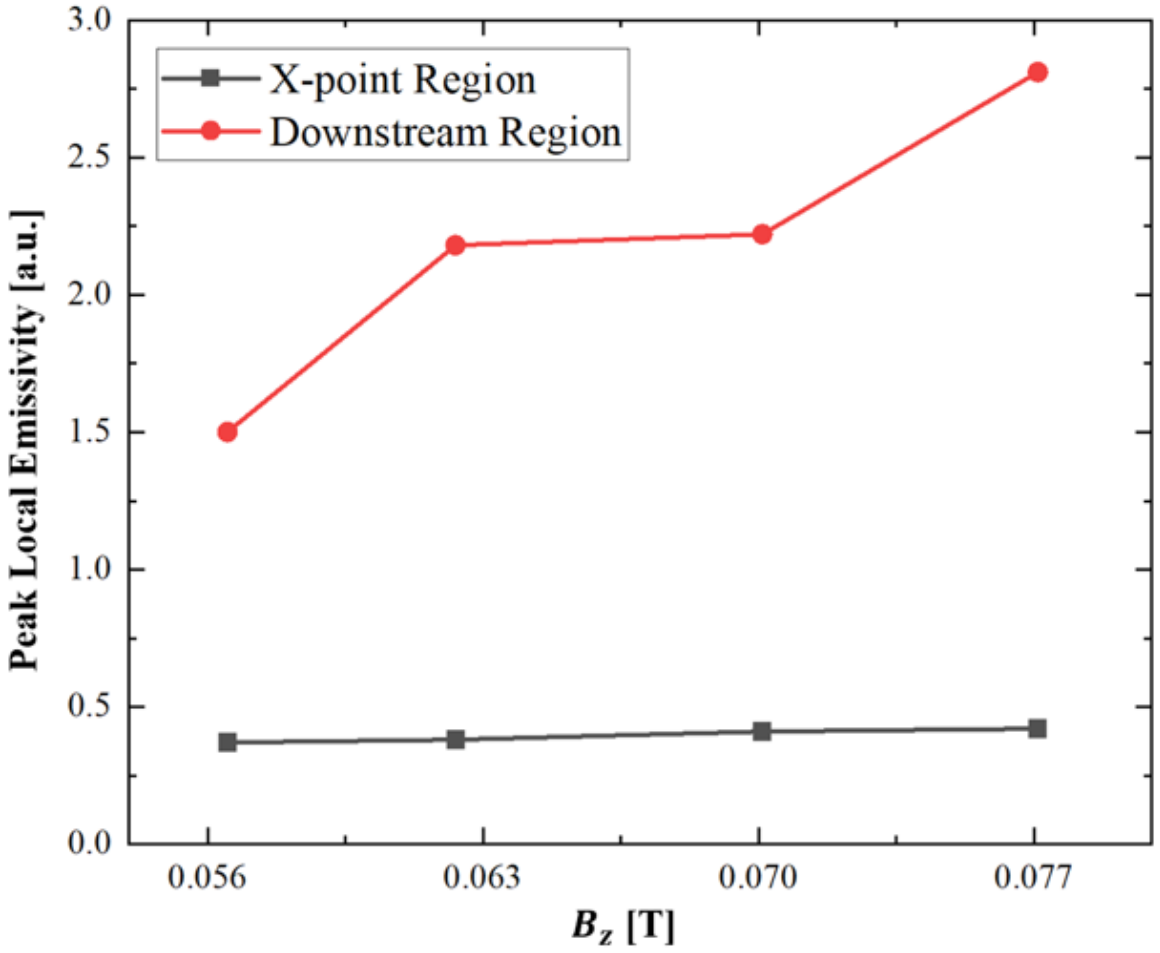

Fig. 5.7 Peak value of local emissivity in X-point and downstream region of the Fig. 5.6 with different B_z at $t = 480\mu$s.

5.4 Effects of Guide Field on Electron Acceleration

Fig. 5.8 shows the positions of test electrons, which is obtained by tracing typical electron trajectories by PIC simulation. For the Fig. 5.8.(a), at the beginning, the test electrons are located in the region of $0 < x < 0.8c/\omega_{pe}$, $2.9c/\omega_{pi} < x < 3.1c/\omega_{pi}$, outside the separatrix. The different color of the dots represents the positions of test electrons at different times. Black, blue, green, and red dots describe the positions of the test electrons at further late timing, respectively. For the Fig. 5.8.(b), at the beginning, the test electrons are located in the region of $0 < x < 0.8c/\omega_{pe}$, $2.7c/\omega_{pi} < x < 2.9c/\omega_{pi}$, inside the separatrix. The different

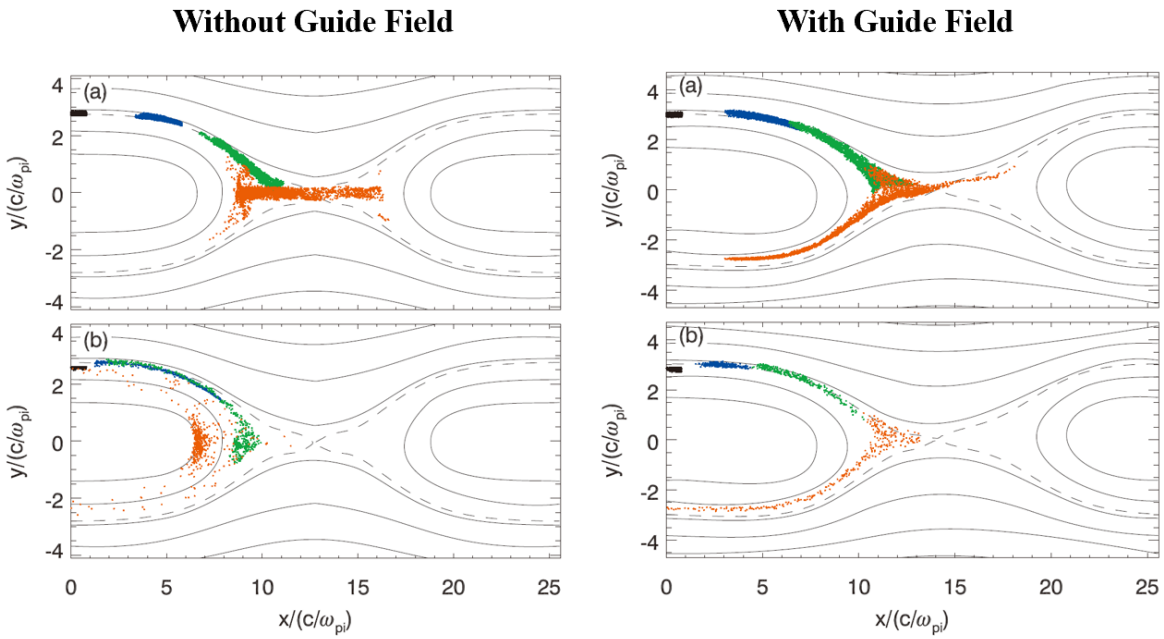

Fig. 5.8 The positions of test electrons at different times. The figures on the left side show the anti-parallel reconnection without guide field, while the ones on the right side show the guide field reconnection. [67]

color of the dots represents the positions of test electrons at different times. By the way, particles with kinetic energy $\varepsilon < 0.3 m_e c^2$ are not plotted, in order to avoid confusion with low-energy particles in the initial time.

The above comparison between reconnection without and with guide field points out that (1) electrons from the outside of separatrix tend to be accelerated in the vicinity of X line, while electrons from the inside tend to be accelerated in the pileup region; (2) the efficiency of electron acceleration is higher in the vicinity of the X line than in the pileup region: (3) electron acceleration can be enhanced by guide field through parallel electric field near the X line.

Fig. 5.9 shows the reconstructed local emissivity of SXR. As the local emissivity reflects the distribution of accelerated electrons, the X-point acceleration is obviously measured. The electrons in the downstream region have much more energy as they can be further accelerated after leaving the X-point by parallel electric field. The peak values of local emissivity in the downstream region are 0.75 at $t = 475$ μs, and 1.5 at $t = 480$ μs. The peak values of local

emissivity in the region near X-point are 0.32 at $t = 475$ μs, and 0.37 at $t = 480$ μs. The above values, which have no other physical meanings, are only used to reflect the relative intensity of local SXR emissivity.

By comparing the above peak values of local SXR emissivity, we can find that both downstream acceleration and X-point acceleration are enhanced with the evolution of magnetic reconnection. The peak values of local SXR emissivity in the downstream region is $2-3$ times stronger than that in the region near the X-point, because electrons are to be further accelerated after leaving from the X-point and obtain much more kinetic energy.

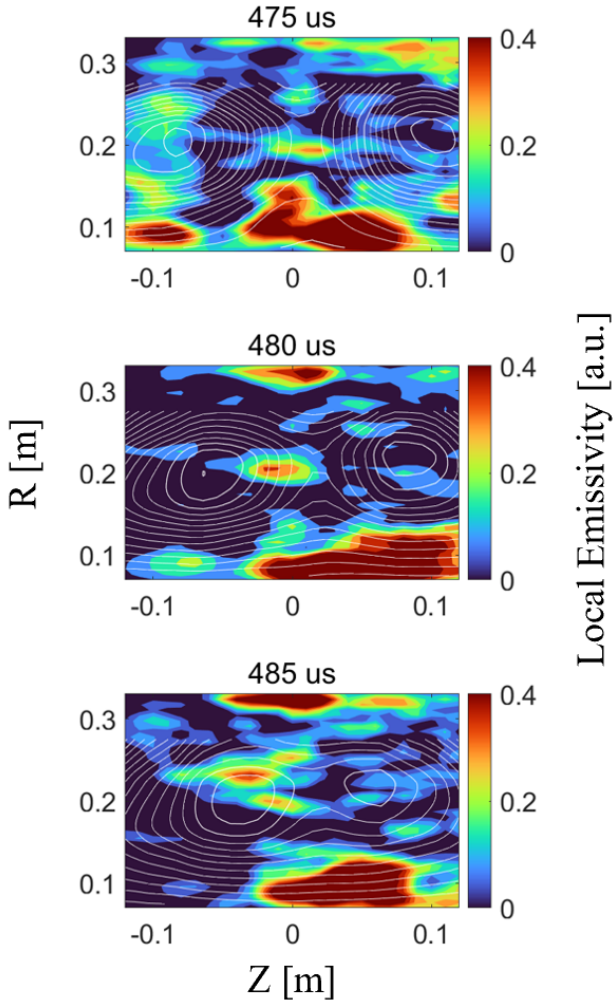

Fig. 5.9 Reconstructed results of SXR images measured by 1.0 μm Mylar-filter pinhole camera. The white curved lines represent magnetic field lines of two merging ST plasmas.

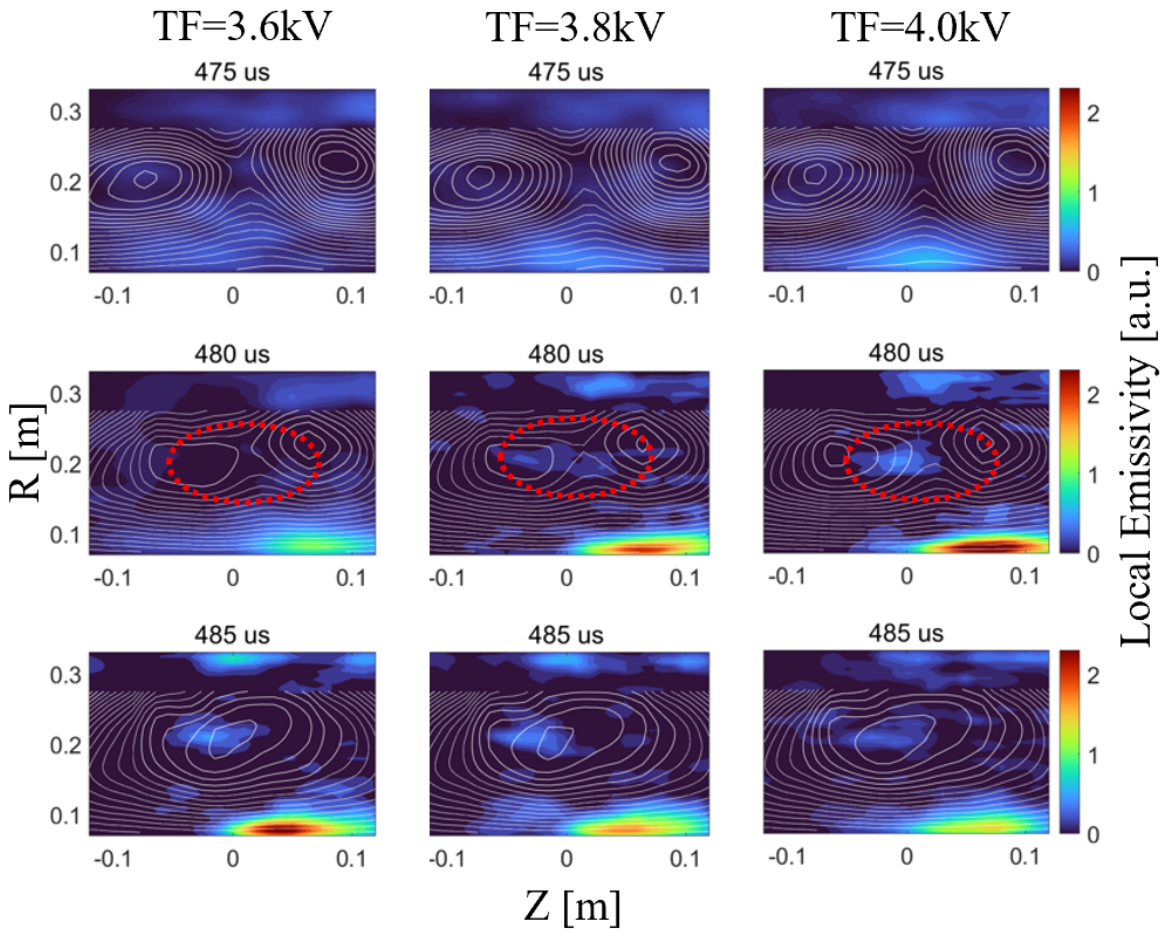

Fig. 5.10 Reconstructed results of SXR images measured by 1.0 μm Mylar-filter pinhole camera with different TF voltage. The white curved lines represent magnetic field lines of two merging ST plasmas.

Similar to the above procedure, plasma merging experiments were carried out on TS-6 device with different charging voltages for TF coils to investigate the effects of guide field on electron acceleration. The voltage of PF was kept in the same value in order to control other variables as the same. The discharge gas is argon (Ar), and the exposure time of framing camera is 2 μs.

The Fig. 5.10 shows the detailed reconstructed results with different charging TF voltage at different times. The toroidal magnetic fields corresponding to charging TF voltages are 0.310 T (3.6 KV), 0.327 T (3.8 KV) and 0.344 T (4.0 KV) respectively.

The peak value of local emissivity in the region near the X-point is employed to quantitatively compare the intensity of SXR emission of the Fig. 5.10 at $t = 480\mu$s. As shown in

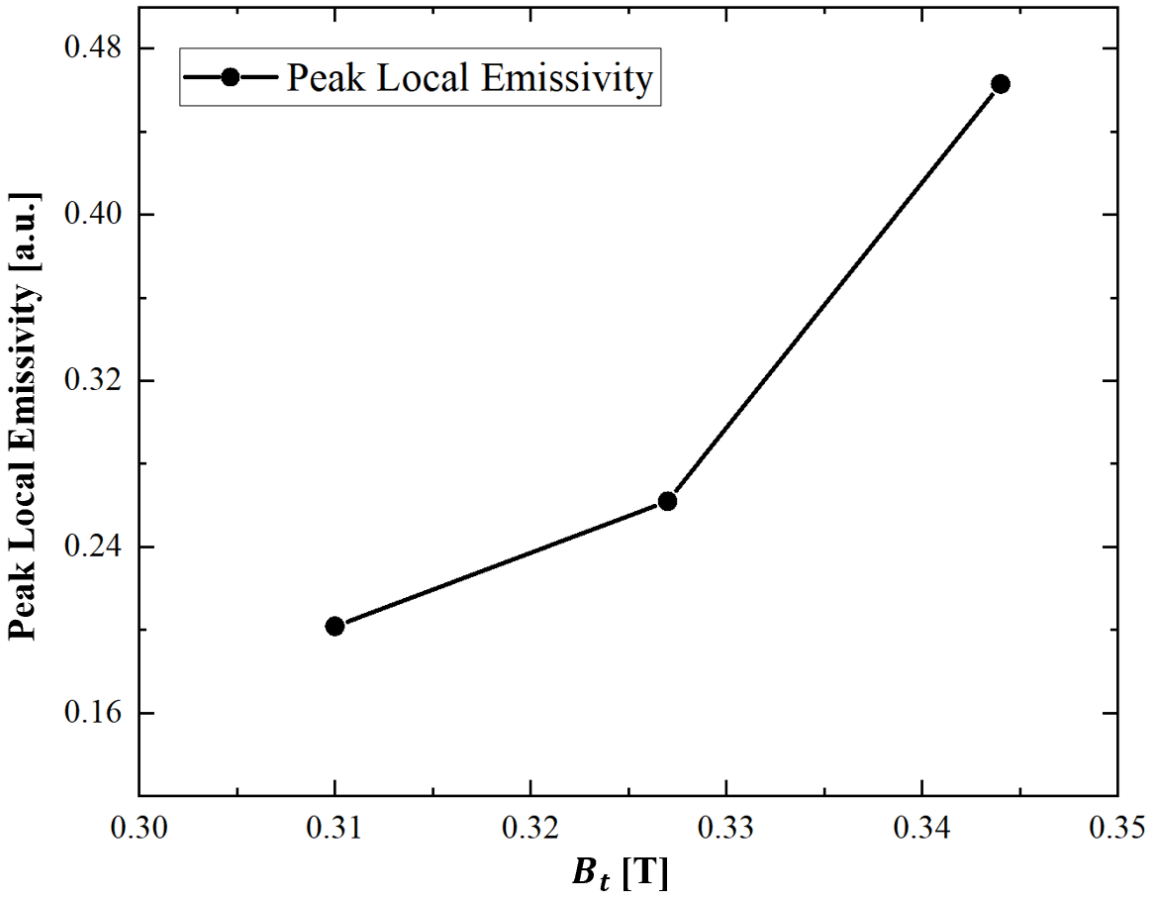

Fig. 5.11 Peak value of local emissivity in the region near the X-point of the Fig. 5.10 at $t = 480\mu$s.

the Fig. 5.11, the local emissivity becomes stronger with a higher toroidal magnetic field B_t, indicating the electron acceleration near the X-point is obviously enhanced along with the increase of B_t. As the peak value of local emissivity in the downstream region with different TF/B_t changes a little and appears at different times, we do not compare it but related issues would be discussed later.

After the electrons enter into the region near the X-point, they would rotate around the guide field. The guide field confines electrons in the vicinity of X-point and further accelerate them[62]. Thus, when higher guide field is employed, the X-point acceleration would be enhanced. So, the local emissivity of SXR would be much stronger, which agree with the experimental results

On the other hand, it can also be found that higher guide field makes the X-ray burst occur earlier and high-energy electrons cool down quickly by comparing the local emissivity of SXR. As shown in the Fig. 5.10, the local emissivity reaches the maximum value at $t = 485$ μs when the TF= 3.6 KV, while it reaches the maximum value at $t = 480$ μs when the TF= 3.8 KV or TF= 4.0 KV. Besides, at $t = 485$ μs, the local emissivity decrease with the increase of TF voltage.

The above experimental results further agree with the mechanism of electron acceleration near the X-point. The PIC simulation figures out that the guide field is able to enhance the electron acceleration through parallel electric field near the X-point, a much more effective acceleration channel than acceleration in the pileup region. So, when a higher guide field is employed, electrons should be accelerated much faster and obtain much more kinetic energy. Therefore, the experimental results are reasonable and agree with the simulation results.

Even-though we had found that the guide field can enhance the electron acceleration near the X-point, but the acceleration in the downstream region is not obviously enhanced with the increase of guide field. It means that the guide field mainly effects the electron acceleration in the region near the X-point. Some research found that a strong guild field would suppress the generation of non-thermal electrons by weakening the Fermi drive mechanism[68]. So, it is necessary to perform high-field and high-energy merging experiences after the upgrade of TS-6 in the future. There could be a threshold for the guide field to enhance the electron acceleration.

5.5 Comparison with Ion Heating

As mentioned in the abstract, the ion heating has been sufficiently investigated in the TS-4[3], MAST[6] and TS-6[5, 7] devices. The global ion heating/transport characteristics of magnetic reconnection during spherical tokamak merging experiments was studied in the TS-6 device[7].

The Fig. 5.12 shows the time evolution of full-2D ion temperature profile during magnetic reconnection with $B_{rec} \sim 0.02$ T and $B_t \sim 0.1$ T. Before the magnetic reconnection ($t = 65\ \mu s$), the ion temperature initially peaks on the magnetic axes of two upstream plasma rings at $r \sim 0.2$ m. With the evolution of plasma merging, the ion temperature profile is converted to a hollow one who has high temperature region around $r \sim 0.12$ m and $r \sim 0.27$ m by downstream heating mechanism of magnetic reconnection. The impulsively formed localized hot spots in the downstream region is then transported mostly on the field line direction to equilibrate the profile on the flux surface as shown in the 1D time evolution of T_i at $r \sim 0.12\ \mathrm{m} \pm 0.02$ m.

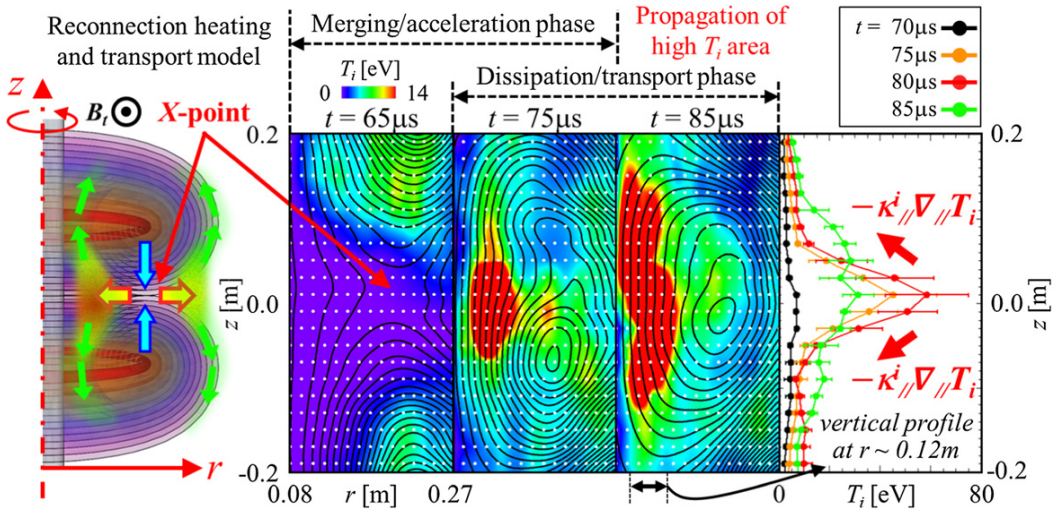

Fig. 5.12 Time evolution of full-2D ion temperature profile during magnetic reconnection. (Left) The reconnection heating/transport model; (Middle) The measured 2D ion temperature profile T_i in three major time frames at $t = 65\ \mu s$, $75\ \mu s$ and $85\ \mu s$ (before, during and after merging) with poloidal flux contour lines; (Right) The 1D vertical profile of radially averaged T_i at $r \sim 0.12\ \mathrm{m} \pm 0.02$ m of each z position.[7]

In the downstream region, the ion thermal energy was found to transport mostly in the field line direction. The previous section has shown our experimental results about electron acceleration. The electrons would be much more accelerated in the direction perpendicular to the field lines, and high-energy electrons are found mainly distributing in the similar position (as shown in the Fig. 5.5) to the hot spots of ion temperature at $t = 75\ \mu s$. The acceleration of electrons can affect the ion heating/transport by the interaction between electrons and ions.

Based on the PIC simulation results, there are also electrons accelerated along the field lines, but they get less kinetic energy. With the upgrade of the TS-6 and the SXR diagnostic, much finer structure should be observed and this kind of electrons are expected to be detected. The electrons accelerated along the field lines would be helpful to explain the ion heating/transport in the field line direction.

Chapter 6

Summary and Conclusions

In order to investigate the electron acceleration mechanism during the evolution of magnetic reconnection, we developed a multi-filter high-resolution soft X-ray imaging diagnostic in TS-6 plasma merging experiments.

The advantages of this diagnostic are listed as follows.

- Stereo soft X-ray images can be simultaneously measured by only one same high-speed camera system.
- The evolution of soft X-ray emission can be recorded.
- Energy analyses can be performed by using two different filters on the stereo pin-hole cameras.
- The MCP chambers are especially designed. It is easy to upgrade the present diagnostic to 16-camera system for 3D tomography and detailed energy analyses.

Detailed design of this SXR diagnostic is introduced in this thesis, including vacuum system, pinhole camera with MCP as detector, high-voltage pulse circuit, optical system, and high-speed imaging system. The above especially designed systems ensure the precision and reliability of the SXR diagnostic.

The tomographic method based on the Phillips-Tikhonov regularization is developed to reconstruct line-integrated images into local emissivity of SXR, which reflects the spatial distribution of high-energy electrons.

Relying on the SXR diagnostic developed on TS-6 plasma merging experiments, the following achievements have been successfully accomplished.

- The SXR has been detected for the first time in the TS-6 plasma merging experiments;
- The photon energy of SXR has been determined to be higher than 100 eV but lower than 400 eV by the use of multiple filters.
- Both downstream acceleration and X-point acceleration have been measured by reconstructing the SXR images into local emissivity.
- The local emissivity in the downstream region is several times stronger than that in the X-point region, indicating that electrons are to be further accelerated after leaving from the X-point and obtain much more kinetic energy.
- Accelerated electrons with higher energy are observed to distribute in further downstream regions of magnetic reconnection, which means that they obtain much more kinetic energy along with the outflow.
- Electrons can be accelerated in the downstream region where the magnetic field piles up, as the electric field can accelerate electrons in their drift direction (gradient drift and curving drift of magnetic field)[61]. We found that electron acceleration in the downstream region could be enhanced with the increase of PF/B_z.
- After the electrons enter into the region near the X-point, they would rotate around the guide field. The guide field confines electrons in the vicinity of X-point and further accelerate them[62]. We also found that the process of electron acceleration could be faster with the increase of guide field. The possible mechanism is that the guide field enhanced the X-point acceleration through parallel electric field, and it is a much more effective channel to accelerate electrons, compared with downstream acceleration. So,

the electron acceleration near the X-point would become stronger and faster. Our experimental results show that the burst of SXR is much earlier and the intensity is much stronger with a higher guide field, which agrees with the mechanism.

Increasing the intensity of SXR signal and improving the accuracy of this SXR diagnostic are necessary for further research on electron acceleration. With higher SXR emission energy, more clear and precise structure can be observed and more physical issues can be studied.

At present, our diagnostic just focuses on SXR with energy a little higher than 100 eV, as the bulk electron temperature is so low. So, it is also a reason to increase the magnetic field to get higher-energy SXR. On the other hand, higher SXR energy can allow us to observe it in more different energy ranges by different filters. There would be more detectors with different filters in our SXR diagnostic in the future.

Of course, the presence of magnetic probes is non-negligible, which obviously influences the motion of high-energy electrons, resulting in the difficulty of increasing electron kinetic energy. In the future, magnetic field measurement without inserting probes into plasma such as EFIT would help solve this problem.

References

[1] Masaaki Yamada, Russell Kulsrud, and Hantao Ji. Magnetic reconnection. *Reviews of Modern Physics*, 82(1):603, 2010.

[2] Yasushi Ono, Kozo Katayama, Akira Yumoto, and Makoto Katsurai. Studies on the formation process and the stability properties of the double-spheromak configuration in a cusp shaped magnetic field. *Kaku Yugo Kenkyu*, 56(3):214–226, 1986.

[3] Y Ono, H Tanabe, Y Hayashi, T Ii, Y Narushima, T Yamada, M Inomoto, and CZ Cheng. Ion and electron heating characteristics of magnetic reconnection in a two flux loop merging experiment. *Physical review letters*, 107(18):185001, 2011.

[4] Y Ono, S Inoue, H Tanabe, Chio-Zong Cheng, H Hara, and R Horiuchi. Reconnection heating experiments and simulations for torus plasma merging start-up. *Nuclear Fusion*, 59(7):076025, 2019.

[5] H Tanabe, Q Cao, H Tanaka, T Ahmadi, M Akimitsu, A Sawada, M Inomoto, and Y Ono. Investigation of fine structure formation of guide field reconnection during merging plasma startup of spherical tokamak in ts-3u. *Nuclear Fusion*, 59(8):086041, 2019.

[6] Hiroshi Tanabe, Takuma Yamada, Takenori Watanabe, Keii Gi, Kazutake Kadowaki, Michiaki Inomoto, Ryota Imazawa, Mikhail Gryaznevich, Clive Michael, B Crowley, et al. Electron and ion heating characteristics during magnetic reconnection in the mast spherical tokamak. *Physical review letters*, 115(21):215004, 2015.

[7] H Tanabe, H Tanaka, Q Cao, Y Cai, M Akimitsu, T Ahmadi, CZ Cheng, M Inomoto, and Y Ono. Global ion heating/transport during merging spherical tokamak formation. *Nuclear Fusion*, 61(10):106027, 2021.

[8] M Inomoto, T Ushiki, X Guo, T Sugawara, K Kondo, T Mihara, Y Minami, Y Inai, H Kaneko, R Yanai, et al. Effects of reconnection downstream conditions on electron parallel acceleration during the merging start-up of a spherical tokamak. *Nuclear Fusion*, 59(8):086040, 2019.

[9] Tomohiko Ushiki. Verification and application of electron energization process during spherical tokamak merging start-up.

[10] Junguang Xiang, Shinjiro Takeda, Yunhan Cai, Hiroshi Tanabe, Qinghong Cao, Haruaki Tanaka, and Yasushi Ono. Double-filter high-resolution soft x-ray tomographic diagnostic for investigating electron acceleration in ts-6 reconnection merging experiments. *Review of Scientific Instruments*, 92(8):083504, 2021.

[11] LC Ingesson, B Alper, BJ Peterson, and J-C Vallet. Chapter 7: Tomography diagnostics: Bolometry and soft-x-ray detection. *Fusion Science and Technology*, 53(2):528–576, 2008.

[12] Naofumi Iwama, Hiromasa Yoshida, Hitoshi Takimoto, Yun Shen, Shuichi Takamura, and Takashige Tsukishima. Phillips–tikhonov regularization of plasma image reconstruction with the generalized cross validation. *Applied physics letters*, 54(6):502–504, 1989.

[13] Eugene N Parker. Sweet's mechanism for merging magnetic fields in conducting fluids. *Journal of Geophysical Research*, 62(4):509–520, 1957.

[14] Ellen G Zweibel and Masaaki Yamada. Magnetic reconnection in astrophysical and laboratory plasmas. *Annual review of astronomy and astrophysics*, 47:291–332, 2009.

[15] JF Drake, M Swisdak, H Che, and MA Shay. Electron acceleration from contracting magnetic islands during reconnection. *Nature*, 443(7111):553–556, 2006.

[16] Dieter Biskamp. Magnetic reconnection in plasmas. *Astrophysics and Space Science*, 242(1):165–207, 1996.

[17] S Usami, H Ohtani, R Horiuchi, and M Den. Development of multi-hierarchy simulation model for studies of magnetic reconnection. *Communications in Computational Physics*, 4:537–544, 2008.

[18] M Hoshino, T Mukai, T Yamamoto, and S Kokubun. Ion dynamics in magnetic reconnection: Comparison between numerical simulation and geotail observations. *Journal of Geophysical Research: Space Physics*, 103(A3):4509–4530, 1998.

[19] T Yamada, H Tanabe, TG Watanabe, Y Hayashi, R Imazawa, M Inomoto, Y Ono, M Gryaznevich, R Scannell, C Michael, et al. Localized electron heating during magnetic reconnection in mast. *Nuclear Fusion*, 56(10):106019, 2016.

[20] Scott Chia Hsu, G Fiksel, TA Carter, H Ji, RM Kulsrud, and M Yamada. Local measurement of nonclassical ion heating during magnetic reconnection. *Physical review letters*, 84(17):3859, 2000.

[21] Jongsoo Yoo, Byungkeun Na, Jonathan Jara-Almonte, Masaaki Yamada, Hantao Ji, Vadim Roytershteyn, Matthew R Argall, William Fox, and Li-Jen Chen. Electron heating and energy inventory during asymmetric reconnection in a laboratory plasma. *Journal of Geophysical Research: Space Physics*, 122(9):9264–9281, 2017.

[22] M Yamada, FM Levinton, N Pomphrey, R Budny, J Manickam, and Y Nagayama. Investigation of magnetic reconnection during a sawtooth crash in a high-temperature tokamak plasma. *Physics of plasmas*, 1(10):3269–3276, 1994.

[23] H Soltwisch. Measurement of current-density changes during sawtooth activity in a tokamak by far-infrared polarimetry. *Review of Scientific Instruments*, 59(8):1599–1604, 1988.

[24] Wikipedia contributors. Nuclear power — Wikipedia, the free encyclopedia. https://en.wikipedia.org/w/index.php?title=Nuclear_power&oldid=1029361529, 2021. [Online; accessed 24-June-2021].

[25] Wikipedia contributors. Deuterium–tritium fusion — Wikipedia, the free encyclopedia. https://en.wikipedia.org/w/index.php?title=Deuterium%E2%80%93tritium_fusion&oldid=1037458352, 2021. [Online; accessed 6-September-2021].

[26] Wikipedia contributors. Magnetic mirror — Wikipedia, the free encyclopedia. https://en.wikipedia.org/w/index.php?title=Magnetic_mirror&oldid=1036659096, 2021. [Online; accessed 6-September-2021].

[27] H Shirai, P Barabaschi, Y Kamada, et al. Recent progress of the jt-60sa project. *Nuclear Fusion*, 57(10):102002, 2017.

[28] Thomas Klinger, A Alonso, S Bozhenkov, R Burhenn, A Dinklage, G Fuchert, J Geiger, O Grulke, A Langenberg, M Hirsch, et al. Performance and properties of the first plasmas of wendelstein 7-x. *Plasma Physics and Controlled Fusion*, 59(1):014018, 2016.

[29] FusionWiki. Sketch of tokamak geometry, including separatrix. http://fusionwiki.ciemat.es/wiki/Triangularity, 2021.

[30] Mitsuru Kikuchi, Karl Lackner, Minh Quang Tran. Fusion physics. International Atomic Energy Agency (IAEA), 2012.

[31] John Wesson. Tokamaks, fourth edition. Oxford Science Publicaitons, 2011.

[32] Ronald Gordon Giovanelli. Studies of the physics of the sun's atmosphere. *Ph. D. Thesis*, 1950.

[33] James Wynne Dungey. *Cosmic electrodynamics*. CUP Archive, 1958.

[34] PA Sweet. Nuovo cimento suppl. *Ser. X*, 8:188, 1958.

[35] HE Petschek. The physics of solar flares. In *AAS-NASA Symp.*, volume 425. NASA, 1964.

[36] M Hesse and PA Cassak. Magnetic reconnection in the space sciences: Past, present, and future. *Journal of Geophysical Research: Space Physics*, 125(2):e2018JA025935, 2020.

[37] Masaaki Yamada, Hantao Ji, Scott Hsu, Troy Carter, Russell Kulsrud, Norton Bretz, Forrest Jobes, Yasushi Ono, and Francis Perkins. Study of driven magnetic reconnection in a laboratory plasma. *Physics of Plasmas*, 4(5):1936–1944, 1997.

[38] J Egedal, A Fasoli, M Porkolab, and D Tarkowski. Plasma generation and confinement in a toroidal magnetic cusp. *Review of Scientific Instruments*, 71(9):3351–3361, 2000.

[39] Y Ono, T Matsuyama, K Umeda, and E Kawamori. Spontaneous and artificial generation of sheared-flow in oblate frcs in ts-3 and 4 frc experiments. *Nuclear fusion*, 43(8):649, 2003.

[40] Andrew Kirk, J Adamek, RJ Akers, S Allan, L Appel, F Arese Lucini, M Barnes, T Barrett, N Ben Ayed, W Boeglin, et al. Overview of recent physics results from mast. *Nuclear Fusion*, 57(10):102007, 2017.

[41] M Inomoto, TG Watanabe, K Gi, K Yamasaki, S Kamio, R Imazawa, T Yamada, X Guo, T Ushiki, H Ishikawa, et al. Centre-solenoid-free merging start-up of spherical tokamak plasmas in utst. *Nuclear Fusion*, 55(3):033013, 2015.

[42] Qinghong Cao, Yunhan Cai, Moe Akimitsu, Junguang Xiang, Tara Ahmadi, Haruaki Tanaka, Hiroshi Tanabe, and Yasushi Ono. Spontaneous formation of plasmoid during early magnetic reconnection phase of two merging tokamaks. *IEEJ Transactions on Electrical and Electronic Engineering*, 15(9):1403–1404, 2020.

[43] Qinghong Cao. Experimental study of dynamic magnetic reconnection in tokamak plasma merging experiment.

[44] Haruaki TANAKA, Hiroshi TANABE, Qinghong CAO, and Yasushi ONO. Global ion heating during st merging driven by high guide field reconnection. *Plasma and Fusion Research*, 16:2402068–2402068, 2021.

[45] AW Edwards, DJ Campbell, WW Engelhardt, H-U Fahrbach, RD Gill, RS Granetz, S Tsuji, BJD Tubbing, A Weller, J Wesson, et al. Rapid collapse of a plasma sawtooth oscillation in the jet tokamak. *Physical review letters*, 57(2):210, 1986.

[46] Stodiek von Goeler, W Stodiek, and N Sauthoff. Studies of internal disruptions and m= 1 oscillations in tokamak discharges with soft—x-ray tecniques. *Physical Review Letters*, 33(20):1201, 1974.

[47] M Bessenrodt-Weberpals, HJ De Blank, M Maraschek, PJ McCarthy, M Sokoll, K Asmussen, et al. Mhd activity as seen in soft x-ray radiation. *Plasma physics and controlled fusion*, 38(9):1543, 1996.

[48] Kevin W Wenzel and Richard D Petrasso. X-ray imaging arrays for impurity transport studies on the texas experimental tokamak. *Review of Scientific Instruments*, 61(2):693–700, 1990.

[49] LC Ingesson, B Alper, H Chen, AW Edwards, GC Fehmers, JC Fuchs, R Giannella, RD Gill, L Lauro-Taroni, and M Romanelli. Soft x ray tomography during elms and impurity injection in jet. *Nuclear fusion*, 38(11):1675, 1998.

[50] S. Ohdachi, K. Toi, G. Fuchs, and S. von Goeler. Tangential soft x-ray camera for large helical device. *Review of Scientific Instruments*, 72(1):724–726, 2001.

[51] S. von Goeler, R. Kaita, M. Bitter, G. Fuchs, M. Poier, G. Bertschinger, H. R. Koslowski, K. Toi, S. Ohdachi, and A. Donné. High speed tangential soft x-ray camera for the study of magnetohydrodynamics instabilities. *Review of Scientific Instruments*, 70(1):599–602, 1999.

[52] BC Stratton, R Feder, S von Goeler, GF Renda, VJ Mastrocola, and JL Lowrance. Initial operation of the national spherical torus experiment fast tangential soft x-ray camera. *Review of scientific instruments*, 75(10):3959–3961, 2004.

[53] T. Onchi, R. Ikezoe, K. Oki, A. Sanpei, H. Himura, and S. Masamune. Tangential soft-x ray imaging for three-dimensional structural studies in a reversed field pinch. *Review of Scientific Instruments*, 81(7), 2010.

[54] Canbin Huang, Kazuaki Hanada, Kengoh Kuroda, Shinichro Kojima, Hiroaki Fujiyoshi, Hiroki Miura, Tomoki Yamada, Hiroshi Idei, Makoto Hasegawa, and Takumi Onchi. Fast tangentially viewed soft x-ray imaging system based on image intensifier with microchannel plate detector on quest. *Plasma and Fusion Research*, 14:1402128–1402128, 2019.

[55] H Koguchi, T Shimada, T Asai, Y Yagi, Y Hirano, and H Sakakita. Soft x-ray tomography system for the toroidal pinch experiment-rx reversed-field pinch. *Review of scientific instruments*, 75(10):4004–4006, 2004.

[56] T Onchi, R Ikezoe, K Oki, A Sanpei, H Himura, and S Masamune. Tangential soft-x ray imaging for three-dimensional structural studies in a reversed field pinch. *Review of Scientific Instruments*, 81(7):073502, 2010.

[57] G. A. Rochau, J. E. Bailey, G. A. Chandler, T. J. Nash, D. S. Nielsen, G. S. Dunham, O. F. Garcia, N. R. Joseph, J. W. Keister, M. J. Madlener, D. V. Morgan, K. J. Moy, and M. Wu. Energy dependent sensitivity of microchannel plate detectors. *Review of Scientific Instruments*, 77(10):10E323, 2006.

[58] Lawrence Berkeley National Laboratory. Filter transmission. *The Center for X-Ray Optics, Lawrence Berkeley National Laboratory*.

[59] L. C. Ingesson, B. Alper, B. J. Peterson, and J.-C. Vallet. Chapter 7: Tomography Diagnostics: Bolometry and Soft-X-Ray Detection. *Fusion Science and Technology*, 53(2):528–576, February 2008.

[60] Mirko Salewski, B Geiger, AS Jacobsen, Per Christian Hansen, WW Heidbrink, Søren Bang Korsholm, Frank Leipold, Jens Madsen, Dmitry Moseev, Stefan Kragh Nielsen, et al. High-definition velocity-space tomography of fast-ion dynamics. *Nuclear Fusion*, 56(10):106024, 2016.

[61] M Hoshino, T Mukai, T Terasawa, and I Shinohara. Suprathermal electron acceleration in magnetic reconnection. *Journal of Geophysical Research: Space Physics*, 106(A11):25979–25997, 2001.

[62] PL Pritchett. Relativistic electron production during guide field magnetic reconnection. *Journal of Geophysical Research: Space Physics*, 111(A10), 2006.

[63] Can Huang, Mingyu Wu, Quanming Lu, Rongsheng Wang, and Shui Wang. Electron acceleration in the dipolarization front driven by magnetic reconnection. *Journal of Geophysical Research: Space Physics*, 120(3):1759–1765, 2015.

[64] Masahiro Hoshino. Electron surfing acceleration in magnetic reconnection. *Journal of Geophysical Research: Space Physics*, 110(A10), 2005.

[65] M Hoshino and Y Lyubarsky. Relativistic reconnection and particle acceleration. *Space science reviews*, 173(1):521–533, 2012.

[66] HS Fu, Yu V Khotyaintsev, Andris Vaivads, Alessandro Retinò, and Mats André. Energetic electron acceleration by unsteady magnetic reconnection. *Nature Physics*, 9(7):426–430, 2013.

[67] Can Huang, Quanming Lu, and Shui Wang. The mechanisms of electron acceleration in antiparallel and guide field magnetic reconnection. *Physics of Plasmas*, 17(7):072306, 2010.

[68] Harry Arnold, JF Drake, Marc Swisdak, Fan Guo, JT Dahlin, Bin Chen, Gregory Fleishman, Lindsay Glesener, Eduard Kontar, Tai Phan, et al. Electron acceleration during macroscale magnetic reconnection. *Physical Review Letters*, 126(13):135101, 2021.

List of figures

List of tables

Appendix A

List of Publications

Academic Papers

[1] Junguang Xiang, Shinjiro Takeda, Yunhan Cai, Hiroshi Tanabe, Qinghong Cao, Haruaki Tanaka, and Yasushi Ono. "Double-filter high-resolution soft x-ray tomographic diagnostic for investigating electron acceleration in TS-6 reconnection merging experiments", *Review of Scientific Instruments 92, 083504 (2021).*

[2] Junguang Xiang, Shinjiro Takeda, Yunhan Cai, Yukehi Okunishi, Haruaki Tanaka, Hiroshi Tanabe, and Yasushi Ono. "Effects of Guide Field on Electron Acceleration during Magnetic Reconnection in TS-6 Merging Experiments", *To be submitted.*

[3] 竹田 慎次朗, 向 俊光, 蔡 雲漢, 田辺 博士, 小野 靖. "高エネルギー電子分布の時間発展計測のための軟X線ステレオ画像計測システムの開発", 電気学会論文誌Ａ *2021 年 141 巻 10 号 p. 604-605.*

[4] Qinghong Cao, Yunhan Cai, Moe Akimitsu, Junguang Xiang, Tara Ahmadi, Haruaki Tanaka, Hiroshi Tanabe, and Yasushi Ono Spontaneous Formation of Plasmoid during Early Magnetic Reconnection Phase of Two Merging Tokamaks. *IEEJ Transactions on Electrical and Electronic Engineering, 15, 1403-1404 (2020).*

Conferences

[1] J. Xiang, S. Takeda, Y. Cai, H. Tanabe, H. Tanaka, Y. Ono “Investigation of Electron Acceleration of Magnetic Reconnection by SXR Tomographic Diagnostic on TS-6 Merging Experiment”, *5th Asia-Pacific Conference on Plasma Physics (AAPPS-DPP 2021), 26 Sept.-1 Oct. 2021*. (Oral Presentation)

[2] J. Xiang, S. Takeda, Y. Cai, Q. Cao, H. Tanabe, Y. Ono “Development of X-ray tomography diagnostic for TS-6 Tokamak Merging Experiments”, *4th Asia-Pacific Conference on Plasma Physics (AAPPS-DPP 2020), 26-31 Oct. 2020*. (Oral Presentation)

[3] S. Takeda, J. Xiang, Y. Cai, H. Tanabe, Y. Ono “Development of Soft X-ray Stereo Imaging System for High-Energy Electron Distribution Measurement”, *5th Asia-Pacific Conference on Plasma Physics (AAPPS-DPP 2021), 26 Sept.-1 Oct. 2021*. (Oral Presentation)

[4] 竹田 慎次朗， 向 俊光，蔡 雲漢，田辺 博士，小野 靖 "磁気リコネクションの高エネルギー電子生成現象の2視点軟X線画像計測" 第*38*回 プラズマ・核融合学会年会*, 2021.11.22(*月*)-11.25(*木*)*. (口頭発表)

[5] Y. Ono, R. Someya, S. Ito, J. Xiang, et al. “Overview of Merging Spherical Tokamak Experiments and Simulations for Burning High-Beta and/or Absolute Minimum-B Plasma Formation”, *28th IAEA Fusion Energy Conference (FEC 2020), 10-15 May 2021*.

[6] Y. Ono, H. Tanabe, S. Kamiya, H. Tanaka, Y. Cai, Q. Cao, J. Xiang, M. Gryaznevich, S. Usami and R. Horiuchi, “Scaling Physics of Reconnection Heating and Acceleration in Tokamak Merging Experiments”, *61th Annual Meeting of the APS Division of Plasma Physics, Florida, USA, Oct. 2019*.